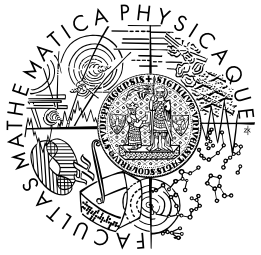

FACULTY
OF MATHEMATICS
AND PHYSICS
Charles University

DOCTORAL THESIS

Jakub Hromádka

2D & 3D computer modelling of low-temperature plasma sheaths with a particular focus on their mutual interaction

Department of Surface and Plasma Science

Supervisor of the doctoral thesis:	prof. RNDr. Rudolf Hrach, DrSc., doc. RNDr. Věra Hrachová, CSc.
Study programme:	Physics
Study branch:	Mathematical and computer modelling

Prague 2023

I declare that I carried out this doctoral thesis independently, and only with the cited sources, literature and other professional sources. It has not been used to obtain another or the same degree.

I understand that my work relates to the rights and obligations under the Act No. 121/2000 Sb., the Copyright Act, as amended, in particular the fact that the Charles University has the right to conclude a license agreement on the use of this work as a school work pursuant to Section 60 subsection 1 of the Copyright Act.

In ..... date ....

Author's signature

I would especially like to thank my supervisor prof. RNDr. Rudolf Hrach, DrSc. who unfortunately did not live to see the work completed. It was he who introduced me to the world of computer modelling and its applications in plasma physics. Thanks to his kind and patient guidance, thanks to his engaging explanations and thanks to his stimulating and valuable advice, I was able to understand the issue very well and master the technique of computer modelling to the extent that I would like to devote myself to it in the future. I thank him many times for everything.

I would also like to say many thanks to doc. RNDr. Věra Hrachová, CSc. who selflessly took over the supervision of the thesis after her husband. I thank her for all her valuable advice, stimulating comments and the time she spent reading the text of the thesis.

I would also like to thank my family and friends for their support throughout my studies and especially my girlfriend for her great support in the final phase of writing the thesis.

I also thank all my colleagues from the Fusion Plasma Division, Institute of Plasma Physics of the Czech Academy of Sciences with whom I could discuss various topics in the field of plasma physics and computer modelling on various occasions.

Title: 2D & 3D computer modelling of low-temperature plasma sheaths with a particular focus on their mutual interaction

Author: Jakub Hromádka

Department: Department of Surface and Plasma Science

Supervisor: prof. RNDr. Rudolf Hrach, DrSc., doc. RNDr. Věra Hrachová, CSc., Department of Surface and Plasma Science

Abstract: The presented thesis deals with the study of the sheath layer which is formed during the interaction of a low-temperature plasma with a solid object using computer modelling techniques. The theoretical part of the thesis summarizes knowledge about the physics of the sheath layer of electropositive and electronegative plasma and presents the theory of measuring plasma parameters using a Langmuir probe, including a discussion of the effect of collisions of charged particles with neutrals on the probe measurements. Further, theoretical descriptions of the plasma are presented which are the basis of the computer models created in the framework of the thesis: a particle model based on the Particle-in-Cell method and a fluid model of the drift-diffusion approximation of the plasma. The developed particle model works in 3D space, uses the null-collision Monte Carlo method to account for the effects of collisions of charged particles with neutrals and implements the Intel® Math Kernel Library functions to solve the Poisson's equation. The fluid model is implemented using FeniCS software. At first, the developed models are used for the calculation of the sheath layer and the current-voltage characteristics of free-standing Langmuir probes of several types: a 1D model of an infinitely large planar probe, a 2D model of a cylindrical probe and a 3D model of a planar probe of finite dimensions. Calculations are successfully compared with theory and mutual differences when using different modelling techniques are discussed. Attention is also paid to the interaction of the sheath layers of two Langmuir probes at a close distance to each other. It is observed that the interaction can occur over a long distance thanks to the long-range electric field in the pre-sheath. With the selected pressure regime, a decreasing profile of the number density of charged particles is observed towards the surface of the probe according to the solution of the diffusion equation – if the probe comes close to another one that measures the current-voltage characteristic, its presence leads to a decrease in the measured current and an underestimation of the evaluated plasma density. If a probe with a constant bias voltage is placed near the probe measuring the current-voltage characteristic, the measured electron temperature is also distorted; if the interacting probe is held at a floating potential, then the influence of its presence on the measured value of the electron temperature is not observed.

Keywords: low-temperature plasma, plasma sheath, Particle-in-Cell method, Langmuir probe, sheath interaction

Contents

Introduction

The beginnings of the field of plasma physics date back to the 1920s when electric discharges under reduced pressure were intensively investigated. During these experiments, an ionized gas was observed and it was first labeled as 'plasma' in 1928 by Irving Langmuir. Since then, the field of plasma physics has undergone very dynamic development both in theory and experiment, and plasma has found application in many fields of human activity. To this day, plasma is the subject of intensive scientific research worldwide.

One of the most important topics in the research field of the low-temperature plasma physics is the study of plasma-solid interaction. At this interface, the so-called sheath layer with a drop of electric potential is created and its existence significantly influences properties of charged particles (e. g. energy distribution, fluxes) which pass from the bulk plasma to the surface of the solid object. Therefore, investigation of plasma sheath properties at different physical conditions is of great importance for all applications where the plasma-solid interaction takes place, e. g. plasma processing techniques of material surface treatment in industry applications (e. g. surface etching of materials, plasma immersion ion implantation, ionized plasma vapour deposition IPVD, thin film deposition PECVD, etc.), diagnostic methods based on the Langmuir probe measurement, procedures of plasma medicine, design of plasma facing components in fusion devices, etc. Due to the wide variety of the low-temperature plasma applications, parameters of the respective plasma discharges also vary in wide ranges (e. g. mean energies of the charged particles, their number densities, multiple particle species in chemically active plasmas, different kinds of scattering processes, energy dependent cross sections, non-equilibrium energy distribution functions, etc.). Therefore, there exist rather various theories of plasma sheath, which cover only certain specific ranges of the plasma parameters, than one universal theory. Since low-temperature plasma is an environment where phenomena over multiple length and time scales are coupled and its description can thus become quite complex, computer models can well support the research in this field.

Application of computer modelling techniques in plasma physics research has been investigated since the very early days when computers became available for scientific research. Numerous computational studies of plasma discharges were performed in the second half of the 20th century to propose and verify suitable numerical schemes. These efforts were summarized in the works Hockney and Eastwood [1988] and Birdsall and Langdon [1991] which are widely used references for particle modelling methods until today. Particle models are able to provide detailed microscopic information about the modelled plasma discharge; on the other hand, they suffer from large demands on the computational resources. In case of low Knudsen number ($Kn = \lambda/L \ll 1$), when the mean free path λ of the charged particles is much lower than the length scale of the problem L, fluid modelling techniques can be advantageously applied as their demands on the computational resources are much lower compared to the particle modelling techniques [Alves, 2007]. Sometimes, both modelling techniques are coupled into the so-called hybrid models which combine their advantages – solution speed of the fluid models and sufficiently precise microscopic description of the particle

models. Such a technique was presented e. g. in the works Bogaerts et al. [1999], Kushner [2009], Hruby and Hrach [2010].

Since particle models provide the most accurate results, considerable attention has been paid to their development, optimization and parallelization. Over the years, models based on the so-called Particle-in-Cell method (PIC) became the most widespread – it was implemented in different types of codes that developed it in different directions. The paper Vahedi and Surendra [1995], for example, describes an implementation that includes the effects of collisions of charged particles with neutrals modelled using the nul-collision method and Monte Carlo techniques. The article Verboncoeur et al. [1995] describes a modular implementation of 2D PIC code using object-oriented programming techniques that also takes into account relativistic effects. In the work of Markidis and Lapenta [2011], we find an implicit implementation of the PIC algorithm which solves the equations of motion of particles and Maxwell's equations implicitly in time and thus eliminates the effects of finite grid instability, which in common implementations of the PIC algorithm leads to an unphysical increase in the energy of the modelled ensemble of particles.

Particle models based on the PIC method have evolved over the years to the extent that they can be incorporated into the research in various areas of plasma physics. An example is the work of Matyash et al. [2007] which describes the use of this method for the study of capacitive radiofrequency discharges in oxygen, dusty plasmas and negative ion sources for heating of fusion plasmas. Another example is the works of Keller et al. [2000] and Miyagawa et al. [2007] which use the 2D PIC method to study one of the plasma processing techniques called plasma immersion ion implantation – in them the influence of various input parameters of the discharge is investigated (e.g. the type of working gas, its pressure, the length of the electric pulse, geometric parameters, effect of secondary emission) on the size of the sheath, the spatial distribution of number densities of electrons, ions and neutrals, the ion flux and its spatial distribution. The application of the PIC modelling methodology for the study of the IPVD process is presented in the works of Lu and Kushner [2001] and Ibehej et al. [2017] which on the one hand use it for precise determination of plasma behavior near the substrate, but also include processes on its surface – the deposition itself including resputtering and movement of physisorbed particles on the surface.

Many studies based on the PIC method were carried out using 1D or 2D models in cases where the geometric symmetry of the studied problem could be exploited. Thanks to the advanced computing technology and especially thanks to the progress in methods of massive parallelization of codes, it has recently become possible to study problems in 3D space as well. An example is the work of Fubiani and Boeuf [2013] where the PIC method is used for modelling of a high power fusion-type negative ion source – the model is used to calculate the plasma characteristics of the ion source and special emphasis is put on the production of negative ions on the plasma grid surface. The work Teunissen and Ebert [2016] presents 3D PIC/MCC simulations of discharge inception around a sharp anode in nitrogen/oxygen mixtures – the study was carried out in a needle-to-plane geometry using different nitrogen/oxygen mixtures at atmospheric pressure.

Since the very beginnings of plasma physics, considerable attention has been devoted to the theoretical description of the sheath layer that forms at the in-

terface between plasma and solid matter. Over the years, a number of works have been created that presented analytical models of the sheath layer under various conditions (e.g. pressure, chemical composition of the plasma, geometric arrangement, collisions with neutral particles, etc.). A very good summary of this effort in terms of electropositive plasma is the work of Riemann [1991] which was supplemented by a theory for multicomponent plasma in the work Riemann [1995].

It turned out that, thanks to its chemical composition, an electronegative plasma (i.e. a plasma that contains negative ions in addition to positive ions and electrons) can be important for practical use. Much attention was paid to its theoretical study and various models were proposed for its description, e.g. the work of Braithwaite and Allen [1988] or the work of Franklin and Snell [1992]. Some of these models were also compared with one dimensional PIC simulations [Lichtenberg et al., 1994] and it was thus shown how the main characteristics of electronegative plasma are varied with pressure or power of plasma discharge and how these parameters change in a large range of electronegativity [Oudini et al., 2013].

Despite the fact that many works dealt with the description of the plasma sheath, only very little attention (to the best of our knowledge) was devoted to the study of the mutual interaction of several plasma sheaths. A unique example is the work of Barnat and Hebner [2007] in which the coupling between the cylindrical probe sheath and the powered planar electrode is described for several mutual positions. In most cases (e.g. double probe method), experimenters try to avoid mutual interaction of plasma sheaths; however, this is not possible in some cases (e.g. at low pressures when plasma sheaths are very large or when dust particles with their own sheath are present nearby the sheath of a probe) and it would therefore be useful to know how much the fluxes of charged particles on a solid object change if its sheath is disturbed by another sheath. Such information can be used for the correct interpretation of measurements using a Langmuir probe whose sheath interacts with another one. The application of computer models developed in the framework of the presented work is aimed at this not very explored area.

The presented work is organized in such a way that in the chapter 1 the theory of the formation of low temperature plasma sheath and the theory of Langmuir probe diagnostics are presented; for both topics, the effects of collisions between charged and neutral particles are also discussed. The chapter 2 summarizes the theory of computer models that were used in the work and the chapter 3 describes their concrete implementation in detail. The chapter 4 presents physical results for selected probe diagnostics topics obtained by the developed computer models.

1. Plasma theory

1.1 Theory of plasma sheath

Plasma sheath is a layer which is created between plasma and a solid surface (figure 1.1). It is a region where the assumption of plasma quasi-neutrality is violated. Characteristic measure of plasma sheath is Debye length λ_D [Lieberman and Lichtenberg, 2005]

$$\lambda_D = \left(\frac{\epsilon_0 \mathrm{k_B} T_e}{\mathrm{e}^2 n_e} \right)^{\frac{1}{2}},$$

where T_e, n_e is temperature and number density of electrons, respectively. Plasma sheath parameters (e.g. size, voltage drop) depend on plasma properties (e.g. composition, energy of particle species). On the contrary, presence of plasma sheath strongly affects characteristics of particles impinging on the surface of a solid object (e.g. energy distribution, flux). Study of plasma sheath is therefore of great importance for all applications where plasma-solid interaction comes into a play (e.g. plasma-assisted techniques of material surface treatment, fusion applications).

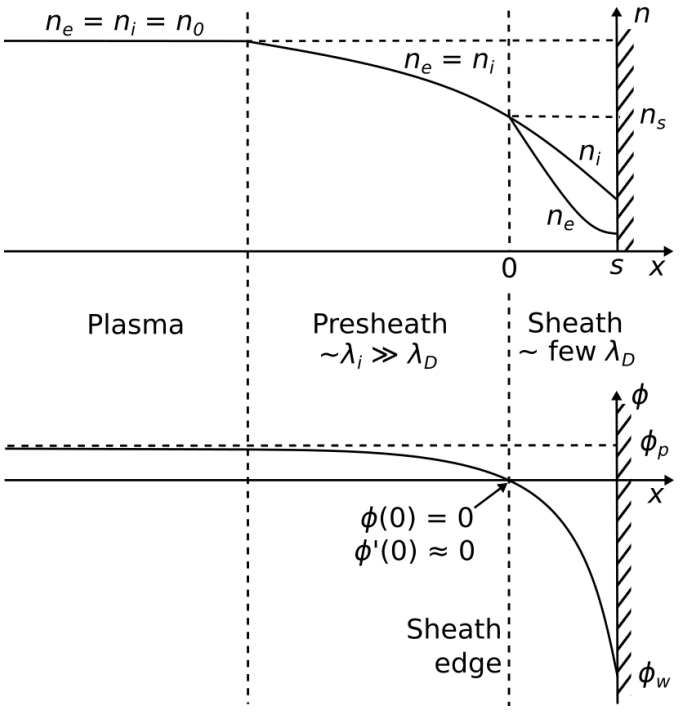

Figure 1.1: Scheme of plasma sheath and presheath created in front of a metal solid wall (n – number density of charged species, ϕ – electric potential). The figure is taken from the book Lieberman and Lichtenberg [2005].

1.1.1 Collisionless sheath

The first insight into the problem of plasma sheath creation can be provided by one dimensional collisionless model which is presented e.g. in the book Lieberman

and Lichtenberg [2005] and which we present in this chapter. The model is based on several assumptions:

- Maxwellian electrons with temperature T_e,
- cold ion approximation ($T_i = 0$),
- $n_e(0) = n_i(0) = n_s$ at the plasma-sheath boundary.

The situation on the interface between plasma and a solid object is schematically shown in the figure 1.1 in terms of electric potential ϕ and number density of electrons n_e and positive ions n_i (u_s – velocity of ions at the sheath boundary, n_0 – number density of charged particles in the bulk plasma).

The following equations can be used for the sheath description. Energy conservation for positive ions (E_s – kinetic energy of ions at the sheath boundary):

$$\frac{1}{2}m_i u_i^2 = \frac{1}{2}m_i u_s^2 - \mathrm{e}\phi = E_s - \mathrm{e}\phi.$$

Continuity of ion flux (ionization is not assumed in the sheath):

$$n_i u_i = n_s u_s.$$

Combination of the given equations leads to an expression for ion number density n_i:

$$n_i = n_s \left(1 - \frac{2\mathrm{e}\phi}{m_i u_s^2}\right)^{-\frac{1}{2}}. \tag{1.1.1}$$

Boltzmann relation can be considered for number density of electrons:

$$n_e = n_s \exp\left(\frac{\mathrm{e}\phi}{k_B T_e}\right). \tag{1.1.2}$$

The expressions for electron and ion number density can be inserted into the Poisson equation for electric potential ϕ:

$$\frac{\mathrm{d}^2\phi}{\mathrm{d}x^2} = \frac{\mathrm{e}}{\epsilon_0}(n_e - n_i) = \frac{\mathrm{e}n_s}{\epsilon_0}\left[\exp\left(\frac{\mathrm{e}\phi}{k_B T_e}\right) - \left(1 - \frac{\mathrm{e}\phi}{E_s}\right)^{-\frac{1}{2}}\right]. \tag{1.1.3}$$

The equations (1.1.1) – (1.1.3) form closed system of non-linear equations for description of the simple collisionless plasma sheath. The equations can be further reformulated and expressions for characteristic properties of plasma sheath can be derived.

Let us multiply the equation (1.1.3) by $\frac{\mathrm{d}\phi}{\mathrm{d}x}$ and let us perform integration with respect to x coordinate on an interval $[0, \phi]$. Let us also assume that $\phi(0) = \frac{\mathrm{d}\phi}{\mathrm{d}x}(0) = 0$ (figure 1.1). Then,

$$\begin{aligned}
\int_0^\phi \frac{\mathrm{d}\phi}{\mathrm{d}x}\frac{\mathrm{d}}{\mathrm{d}x}\left(\frac{\mathrm{d}\phi}{\mathrm{d}x}\right)\mathrm{d}x &= \frac{\mathrm{e}n_s}{\epsilon_0}\int_0^\phi \left[\exp\left(\frac{\mathrm{e}\phi}{k_B T_e}\right) - \left(1 - \frac{\mathrm{e}\phi}{E_s}\right)^{-\frac{1}{2}}\right]\frac{\mathrm{d}\phi}{\mathrm{d}x}\mathrm{d}x, \\
\frac{1}{2}\left(\frac{\mathrm{d}\phi}{\mathrm{d}x}\right)^2 &= \frac{\mathrm{e}n_s}{\epsilon_0}\left[k_B T_e \exp\left(\frac{\mathrm{e}\phi}{k_B T_e}\right) - k_B T_e + 2E_s\left(1 - \frac{\mathrm{e}\phi}{E_s}\right)^{\frac{1}{2}} - 2E_s\right].
\end{aligned} \tag{1.1.4}$$

The solution of equation (1.1.4) exists only when its right-hand side is greater than zero. After making Taylor's series expansion up to the second order, the following condition is obtained:

$$\frac{1}{2}\frac{\phi^2}{k_B T_e} - \frac{1}{4}\frac{\phi^2}{E_s} \geq 0 \Rightarrow E_s \geq \frac{k_B T_e}{2}.$$

Finally, the so-called Bohm criterion is derived:

$$u_s \geq u_B = \left(\frac{k_B T_e}{m_i}\right)^{\frac{1}{2}}. \tag{1.1.5}$$

In order for a sheath in front of a solid object existed, kinetic energy of the ions entering the sheath region must be high enough so they are able to overcome thermal energy of the electrons and build positive space charge area in the sheath.

Positive ions are accelerated to the Bohm velocity u_B in a region which preceeds the sheath and which is called *presheath*. It is a region where plasma is quasineutral and where non-zero electric field is present. On the border between sheath and presheath, subsonic ion flux ($u_i < u_B$) changes into the supersonic one ($u_i > u_B$).

Size of the potential drop ϕ_p in the presheath can be derived from the following equality where the already derived expression for Bohm velocity u_B is inserted into the expression for the kinetic energy of the ions:

$$\begin{aligned} \frac{1}{2} m_i u_B^2 &= \mathrm{e}\phi_p, \\ \phi_p &= \frac{k_B T_e}{2\mathrm{e}}. \end{aligned} \tag{1.1.6}$$

If the Boltzmann relation for number density of electrons is considered also in presheath, an expression for plasma density n_s at the edge of the sheath can be derived

$$n_s = n_0 \exp\left(-\frac{\mathrm{e}\phi_p}{k_B T_e}\right) \approx 0.61 n_0. \tag{1.1.7}$$

Expression for the floating potential ϕ_w of the metal wall (with respect to the sheath-presheath edge) which is in contact with plasma can be derived from the equality of electron Γ_e and ion Γ_i fluxes on the wall

$$\Gamma_i = n_s u_B = \Gamma_e = n_s \exp\left(\frac{\mathrm{e}\phi_w}{k_B T_e}\right)\frac{1}{4} v_{th}, \tag{1.1.8}$$

$$\begin{aligned} n_s \left(\frac{k_B T_e}{m_i}\right)^{\frac{1}{2}} &= n_s \exp\left(\frac{\mathrm{e}\phi_w}{k_B T_e}\right)\frac{1}{4}\left(\frac{8 k_B T_e}{\pi m_e}\right)^{\frac{1}{2}}, \\ \phi_w &= \frac{k_B T_e}{\mathrm{e}} \ln\left(\frac{2\pi m_e}{m_i}\right)^{\frac{1}{2}}, \end{aligned} \tag{1.1.9}$$

where v_{th} is the mean speed of the thermal motion of the electrons.

Energy E_i of the positive ions which land on the metal wall is given by the sum of energy which they gain in the presheath and energy gained in the sheath

$$E_i = \mathrm{e}\left(\phi_p + |\phi_w|\right) = k_B T_e \left[\frac{1}{2} + \ln\left(\frac{m_i}{2\pi m_e}\right)^{\frac{1}{2}}\right].$$

Size s of the sheath can be evaluated in such a way that expression (1.1.4) is numerically integrated to obtain the expression for distribution of potential $\phi(x)$ in the sheath and consequently the equation

$$\phi(s) = \phi_w,$$

is solved for the size s of the sheath.

1.1.2 Sheaths in electronegative plasma

Bohm sheath criterion in the form (1.1.5) was derived under several specific assumptions. The criterion can be extended to the more general conditions, e. g. for electronegative plasma which includes also negatively charged ions. Such general criterion was derived in the article Riemann [1991] in the form

$$\frac{1}{m_i}\int_0^\infty \frac{1}{v^2} f(v)\mathrm{d}v \leq \frac{1}{\mathrm{e}} \frac{\mathrm{d}\left(n_e + n_-\right)}{\mathrm{d}\phi}\Big|_{\phi=0}, \tag{1.1.10}$$

where n_- denotes the number density of negatively charged ions and $f(v)$ is the velocity distribution funtion of positive ions. The generalized criterion can be useful for better understanding of sheath creation in electronegative plasma as it is presented in the works Boyd and Thompson [1959] and Lieberman and Lichtenberg [2005].

If negative ions are present in the plasma, the Poisson equation for the electric potential ϕ can be written in the from

$$\Delta\phi = -\frac{\mathrm{e}}{\epsilon_0}\left(n_i - n_e - n_-\right),$$

where n_i, n_e and n_- are positive ion, electron and negative ion number densities. Plasma quasi-neutrality is assumed at the sheath edge: $n_{si} = n_{se} + n_{s-}$. Further, the ratio of negative ions to electrons is defined: $\alpha_s = n_{s-}/n_{se}$. As a result, the quasi-neutrality condition can be written as

$$n_{s+} = \left(1 + \alpha_s\right) n_{se}.$$

If the distributions of electrons and negative ions are Maxwellian, the temperature ratio $\gamma = T_e/T_-$ can be introduced. Considering the Boltzmann relation for electrons and negative ions, we obtain

$$n_e + n_- = n_{se} \exp\left(\frac{\mathrm{e}\phi}{\mathrm{k_B}T_e}\right) + \alpha_s n_{se} \exp\left(\gamma\frac{\mathrm{e}\phi}{\mathrm{k_B}T_e}\right).$$

Using the already derived quasi-neutrality condition at the sheath edge, we get

$$n_e + n_- = \frac{n_{s+}}{1+\alpha_s}\left[\exp\left(\frac{\mathrm{e}\phi}{\mathrm{k_B}T_e}\right) + \alpha_s \exp\left(\gamma\frac{\mathrm{e}\phi}{\mathrm{k_B}T_e}\right)\right].$$

This expression can be inserted into the generalized Bohm criterion (1.1.10). Once the derivative on the right-hand side is performed, we get

$$\frac{k_B T_e}{m_i}\int_0^\infty \frac{1}{v^2} f(v)\mathrm{d}v \leq n_{s+}\left(\frac{1+\alpha_s\gamma}{1+\alpha_s}\right).$$

Taking into account the assumption of cold ions, the following condition for the velocity of positive ion at the sheath edge is obtained

$$u_s \geq u_B = \left[\frac{k_B T_e \left(1+\alpha_s\right)}{m_i \left(1+\alpha_s \gamma\right)}\right]^{\frac{1}{2}}. \tag{1.1.11}$$

It can be seen that for high γ and not too small α_s, the presence of negative ions can significantly reduce the required velocity of positive ions at the sheath edge. In this situation, the positive ion temperature cannot be neglected and integration over the ion velocity distribution in the generalized expression (1.1.10) should be performed.

Further, the negative potential in the sheath and presheath causes that the negative ions are repelled from this region. As a result, electronegativity at the sheath edge α_s is lower with respect to the electronegativity in the plasma bulk α_b and the role of electrons in the sheath region gets more important. Using the Boltzmann relation for electrons and negative ions, their number density at the sheath edge can be related to that one in the plasma bulk

$$n_{se} = n_{be} \exp\left(-\frac{\mathrm{e}\phi_p}{\mathrm{k_b} T_e}\right),$$
$$n_{s-} = n_{b-} \exp\left(-\gamma\frac{\mathrm{e}\phi_p}{\mathrm{k_b} T_e}\right),$$

where ϕ_p is the potential drop in the presheath (figure 1.1). Using the definition of electronegativity α and the relations for number density above, the following expression is obtained

$$\alpha_s = \alpha_b \exp\left[\frac{\mathrm{e}\phi_p(1-\gamma)}{\mathrm{k_B} T_e}\right]. \tag{1.1.12}$$

In the chapter 1.1.1, expresssion for the potential drop in the presheath (1.1.6) was derived using the consideration of energy conservation of the positive ions in the presheath

$$\frac{1}{2} m_i u_B^2 = \mathrm{e}\phi_p.$$

If the same consideration is done taking into account the generalized Bohm criterion (1.1.11), the following expression for the potential drop in the presheath in case of electronegative plasma is obtained

$$\phi_p = \frac{\mathrm{k_B} T_e}{\mathrm{e}} \frac{1+\alpha_s}{2(1+\gamma\alpha_s)}.$$

It can be seen that it gives the same value of ϕ_p for $\alpha_s = 0$ as the expression (1.1.6). If the expression for ϕ_p is inserted into the equation (1.1.12), the relation between α_b and α_s is obtained

$$\alpha_b = \alpha_s \exp\left[\frac{(1+\alpha_s)(\gamma-1)}{2(1+\gamma\alpha_s)}\right].$$

Typically, α_b is known and α_s can be evaluated from the last derived equation (e. g. numerically). Dependence of electronegativity at the sheath edge α_s and

potential drop in the presheath ϕ_p on the electronegativity of the plasma bulk α_b according to the derived expressions is shown in the figure 1.2 for several values of the $\gamma = T_e/T_-$ parameter [Boyd and Thompson, 1959].

It can be seen that in case of $\gamma > 30$, which is typical condition for electronegative discharges, the influence of electrons on plasma sheath is more significant than that one of negative ions. Even for values of α_b close to 1 and slightly above, quite low electronegativity at the sheath edge α_s is observed and potential drop in the presheath is close to the value expected for electropositive plasma $\phi_p = k_B T_e/2\mathrm{e}$.

It should be mentioned that the expressions derived above provide description of the electronegative sheaths only in the first approximation – e. g. the assumption of the Boltzmann relation for negative ions does not have to be valid; there might be also additional effects if plasma is collisional.

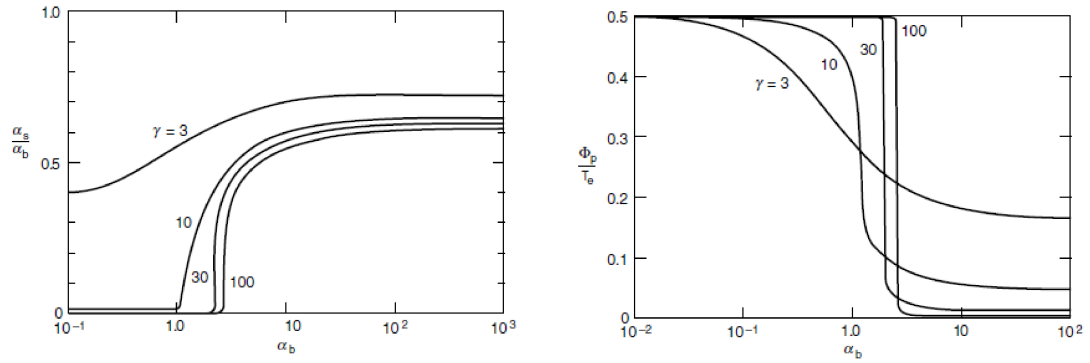

(a) Electronegativity at the sheath edge α_s (b) Potential drop ϕ_p in presheath

Figure 1.2: Parameters of the electronegative plasma sheaths with respect to the electronegativity in the plasma bulk α_b for different values of the $\gamma = T_e/T_-$ parameter. The figures are based on the work Boyd and Thompson [1959].

1.1.3 Plasma sheath in the presence of collisions

Collisionless plasma sheath is a quite special case for which the exact position of the sheath edge can be relatively easily defined – it is at the point where the quasi-neutral presheath solution becomes singular and positive ions reach the Bohm velocity. In the case of weakly collisional plasma, the situation at the sheath-presheath interface is more complicated and it is not possible to define its exact position. The problem was adressed in numerous works, e. g. Riemann [1991], Riemann [1997], Godyak and Sternberg [1990]. It turned out that two characteristic scales which are well separated can be defined for weakly collisional plasma: presheath scale length which is given by ion-neutral mean free path λ_i and sheath scale length given by a few Debye lengths λ_D with $\lambda_i \gg \lambda_D$. In addition, there is an intermediate length scale $\lambda_i^{1/5}\lambda_D^{4/5}$ which characterizes the transition region between the presheath and the sheath. The ion drift speed is lower than the Bohm speed in this region.

In the case of highly collisional plasmas with $\lambda_i \leq \lambda_D$, the ion transport is well described by mobility coefficient ($u_i \approx \mu_i E$), the intermediate transition region is not present anymore and breakdown of the plasma quasi-neutrality happens at a

sheath width

$$s \approx K\left(\lambda_D^2 l\right)^{\frac{1}{3}} \approx \left(\pi K^3\right)^{\frac{1}{2}} \lambda_{Ds},$$

where λ_D is the Debye length of a bulk plasma, λ_{Ds} is Debye length at the sheath edge, l is the characteristic length of the plasma discharge. K is coefficient of order unity and it was derived e. g. in the work Franklin and Snell [2000]: $K \approx 2.2 + 0.125 \log_{10}(\nu_{iz}/\nu_{mi})$, where ν_{iz} is the ionization frequency and ν_{mi} is the ion-neutral momentum transfer frequency. The ion speed at the sheath edge is below the Bohm speed which is described by expression [Franklin, 2002]

$$u_s \approx u_B \left(C \frac{\lambda_i}{\lambda_{Ds}}\right)^{\frac{1}{2}}, \tag{1.1.13}$$

where C is a coefficient of order unity, or by expression [Godyak and Sternberg, 1990]

$$u_s \approx \frac{u_B}{(1 + \pi\lambda_{Ds}/2\lambda_i)^{\frac{1}{2}}}. \tag{1.1.14}$$

Since the situation at the interface between bulk plasma and sheath region is quite complicated as many parameters come into play, the exact position of the sheath edge is a matter of definition. However, it is mainly the ion flux entering the sheath which determines the sheath properties and which has some physical meaning. It can be utilized in the definition of boundary conditions for solution of diffusion problems

$$-D(\nabla n)_s = n_s u_B.$$

For highly collisional plasma, it turns out that the diffusion solutions are quite insensitive to the edge ion drift speed and simple boundary condition

$$n \approx 0$$

at the perfectly absorbing wall can be used instead.

1.2 Theory of Langmuir probe measurement

To understand plasma behavior in different operating conditions, measurements of its local basic parameters is crucial. Since the very beginning of plasma physics in the 1920's, one of the most common diagnostic tools, which is still used also nowadays, is the Langmuir probe. It is a small metallic electrode with a well defined geometry (planar, cylindrical or spherical) which is immersed into the plasma. Voltage bias U_p with respect to the local space plasma potential is then applied on the probe and the drained current I_p for different probe potentials U_p is monitored. Finally, plasma parameters are calculated from this current-voltage (IV) characteristics. In this way, the following plasma parameters can be obtained: plasma density (n_e, n_i), electron temperature (T_e), electron energy distribution function, plasma potential and ion flux. The simplicity of the Langmuir probe construction and of the associated electronics is its very valuable benefit. The other one is that apart of the other diagnostic methods (such as e. g. spectroscopy) it can provide measurement of the local parameters since the disturbance caused by the probe can be well localized under a wide range of

conditions. To achieve this, the probe has to be, however, very carefully designed. On the other hand, the interpretation of the measured IV characteristics is often difficult. The probe can be used in a wide range of working conditions (pressures 10^{-5} - 10^{3} Torr, plasma density 10^{15} - $10^{24}\mathrm{m}^{-3}$) and there is no universal probe theory which would describe IV characteristics over such a wide parametric range. When the probe is immersed into the plasma, sheath region where large electric fields can be present appears and its relative dimension with respect to the characteristic size of the probe affects the trajectory of the charged particles which approach the probe. Further, collisions of charged particles with the neutrals can also significantly affect their motion in the sheath region if the mean free paths are comparable to the Debye length. Since the nature of the charged particles motion is different under these various conditions, there are multiple probe theories which can be applied in the specific working regimes of the Langmuir probe as can be seen in the schematic figure 1.3 (taken from the article Bose et al. [2017]). In the following sections, the collisionless theories are described in detail and effects of collisions on the probe measurements are discussed as well.

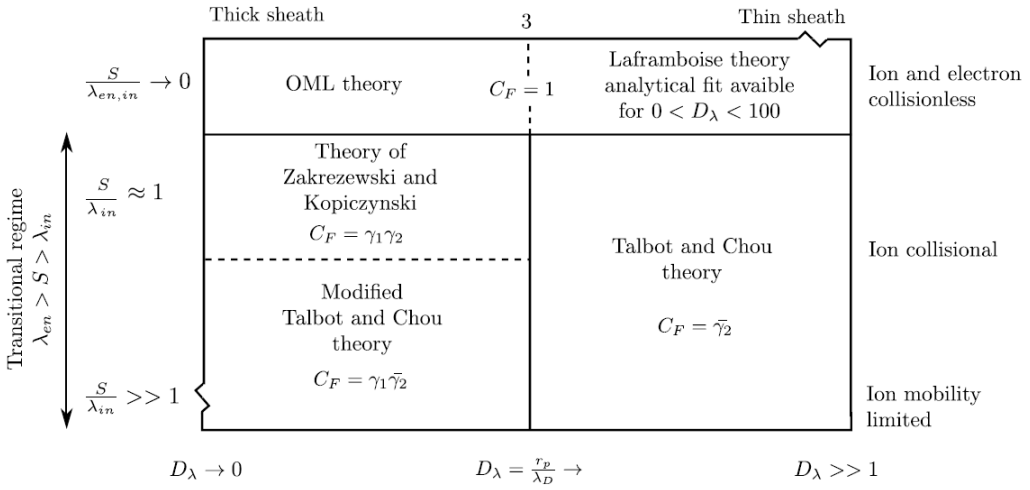

Figure 1.3: Different operating regimes of a Langmuir probe and probe theories [Bose et al., 2017]. S denotes the dimension of the sheath, λ_{en} and λ_{in} represent the electron-neutral and ion-neutral mean free path, r_p is the probe radius, λ_D is the Debye length and C_F represents the correction factor to the normalized Laframboise current.

1.2.1 Collisionless probe theories

The simplest probe theory was formulated in the article by Mott-Smith and Langmuir [Mott-Smith and Langmuir, 1926] and it is valid for unmagnetized collisionless Maxwellian plasmas. The theory is based on several assumptions:

- The bulk plasma is considered as infinite, stationary, homogeneous, Maxwellian and quasineutral.

- The presence of the probe causes perturbation which is confined to a space

charge sheath with a well defined boundary. Outside the sheath, the electric potential is assumed uniform.

- The sheath size is small compared to the characteristic probe dimension and edge effects can be thus neglected.
- The collisional mean free path λ of the charged particles is larger than the Debye length λ_D and than the characteristic probe dimension.
- The charged particles which reach the probe surface are always collected. The particles do not chemically react with the probe material; the probe does not emit.
- The electric potential in the vicinity of the probe preserves the symmetry (planar, cylindrical or spherical) and it is a monotonic function between the sheath edge and the probe surface.
- The electric currents of the different charged particle species on the probe are independent of each other and can be calculated separately.

In the following paragraphs, the expressions which relate the plasma properties with current voltage curves are presented for planar, cylindrical and spherical probes. Derivation of the expression for electric current on the planar probe is quite straightforward; for the cylindrical and the spherical probes, more complicated expressions are obtained since the orbital motions of the charged particles have to be also taken into account. For a detailed derivation of these expressions, we refer to the article Mott-Smith and Langmuir [1926]. For the spherical and the cylindrical probes, the expressions in the thin sheath ($r_s - r_p \ll r_p$) and the thick sheath ($r_s \gg r_p$) limits are presented (r_p is the probe radius, r_s is the sheath radius). The expressions in the thick sheath limit correspond to the so-called OML theory (*orbital motion limited theory*). At this place, we define the expressions for thermal velocity v_{th}, saturation current density j_0 and dimensionless probe potential η which we use in the next paragraphs:

$$v_{th} = \left(\frac{8 \mathrm{k_B} T}{\pi m} \right)^{\frac{1}{2}},$$
$$j_0 = \frac{1}{4} n_0 v_{th} q,$$
$$\eta = \frac{q U_p}{\mathrm{k_B} T},$$

where U_p is the bias of the probe with respect to the plasma potential.

Planar probe

At first, electric current of the charged particles which are repelled from the planar probe ($qU_p > 0$) is investigated. Providing that the normal to the surface of the probe is oriented in the positive direction of the x axis of the Cartesian coordinate system, the following expression for the current density j on the probe can be written

$$I = q A_{pln} \int_{-\infty}^{\infty} \int_{-\infty}^{\infty} \int_{-\infty}^{-v_{min}} f(\boldsymbol{r}, \boldsymbol{v}, t) v_x \mathrm{d}v_x \mathrm{d}v_y \mathrm{d}v_z,$$

where A_{pln} is the area of the planar probe, $f(\boldsymbol{r}, \boldsymbol{v}, t)$ is the velocity distribution function of the charged particles and $v_{min} = (2qU_p/m_e)^{1/2}$ – the particles must have sufficiently high velocity in the negative direction of the x axis so they are able to overcome braking electrostatic field of the probe and they can reach its surface. If the isotropic Maxwellian distribution of the particles is assumed, we can write

$$I = qA_{pln}\left(\frac{m}{2\pi \mathrm{k_B}T}\right)^{\frac{3}{2}} \int_{-\infty}^{\infty}\int_{-\infty}^{\infty}\int_{-\infty}^{-v_{min}} \exp\left(-\frac{mv^2}{2\mathrm{k_B}T}\right) v_x \mathrm{d}v_x \mathrm{d}v_y \mathrm{d}v_z. \tag{1.2.1}$$

Performing integration in the considered limits, we obtain

$$I(\eta) = \frac{1}{4} n_0 v_{th} q A_{pln} \exp(-\eta) = j_0 A_{pln} \exp(-\eta). \tag{1.2.2}$$

If the potential of the probe is attractive for the charged particles ($qU_p < 0$), the integration of the v_x component in the equation (1.2.1) can be performed over the entire interval $(-\infty; \infty)$ and we get

$$I(\eta) = j_0 A_{pln}. \tag{1.2.3}$$

In the view of the derived expressions, the knowledge of the dependance of the electron current I_e on the bias of the probe U_p (I-V characteristics) allows us to write the following expressions for the electron temperature T_e and number density n_e

$$T_e = \frac{\mathrm{e}}{\mathrm{k_B}}\left(\frac{\mathrm{d}}{\mathrm{d}U_p}\ln|I_e|\right)^{-1}, \tag{1.2.4}$$

$$n_e = \frac{(I_e)_{U_p=0}}{\mathrm{e}A_{pln}}\left(\frac{2\pi m_e}{\mathrm{k_B}T_e}\right)^{\frac{1}{2}}. \tag{1.2.5}$$

Cylindrical probe

- Repelled particles ($qU_p > 0 \Rightarrow \eta > 0$):

  $$I(\eta) = j_0 A_{cyl} \exp(-\eta),$$

  where A_{cyl} is the area of the cylindrical probe.

- Attracted particles ($qU_p < 0 \Rightarrow \eta < 0$):

  $$I(\eta) = j_0 A_{cyl}\left\{\frac{r_s}{r_p}\mathrm{erf}\left[\left(\frac{r_p^2}{r_s^2 - r_p^2}|\eta|\right)^{\frac{1}{2}}\right] + \exp(|\eta|)\,\mathrm{erfc}\left[\left(\frac{r_s^2}{r_s^2 - r_p^2}|\eta|\right)^{\frac{1}{2}}\right]\right\},$$

  where $\mathrm{erfc}(x) = 1 - \mathrm{erf}(x)$.

  - Thin sheath limit ($r_s - r_p \ll r_p$):

    $$I(\eta) = j_0 A_{cyl}.$$

  - Thick sheath limit ($r_s \gg r_p$):

    $$I(\eta) = j_0 A_{cyl}\left[\frac{2}{\sqrt{\pi}}\eta^{\frac{1}{2}} + \exp(|\eta|)\,\mathrm{erfc}\left(|\eta|^{\frac{1}{2}}\right)\right],$$

    or even more simplified expression can be considered

    $$I(\eta) = j_0 A_{cyl}\frac{2}{\sqrt{\pi}}(1 + |\eta|)^{\frac{1}{2}}.$$

Spherical probe

- Repelled particles ($qU_p > 0 \Rightarrow \eta > 0$):

$$I(\eta) = j_0 A_{sph} \exp(-\eta),$$

  where A_{sph} is the area of the spherical probe.

- Attracted particles ($qU_p < 0 \Rightarrow \eta < 0$):

$$I(\eta) = j_0 A_{sph} \frac{r_s^2}{r_p^2} \left[1 - \left(1 - \frac{r_p^2}{r_s^2}\right) \exp\left(-\frac{r_p^2}{r_s^2 - r_p^2}|\eta|\right)\right].$$

  – Thin sheath limit ($r_s - r_p \ll r_p$):

$$I(\eta) = j_0 A_{sph}.$$

  – Thick sheath limit ($r_s \gg r_p$):

$$I(\eta) = j_0 A_{sph} (1 + |\eta|). \tag{1.2.6}$$

The presented expressions suggest that the probe current is independent of the probe voltage in the thin sheath limit. The sheath has, however, finite thickness which varies depending on the probe voltage. If we assume that all particles which enter the sheath hit the probe, the probe current can be written as

$$I = j_0 A_s, \tag{1.2.7}$$

where A_s is the area of the sheath. If we neglect density of the charged particles which are repelled by the probe in the sheath, then its thickness can be calculated from the equations describing the space charge limited emmision from one plane (= the sheath edge in our case) to the other one (= the probe surface)

$$j = \frac{4}{9}\epsilon_0 \left(\frac{2q}{m}\right)^{\frac{1}{2}} \frac{|U_p - U_s|^{\frac{3}{2}}}{(r_s - r_p)^2}. \tag{1.2.8}$$

This is the well-known Child-Langmuir law for space-charge-limited current between two planes. If we consider $U_s = 0$ and $j = j_0$, then we can use the Child-Langmuir law to obtain the value of sheath thickness $(r_s - r_p)$ for a given probe voltage U_p. Consequently, the sheath thickness can be used for evaluation of the sheath area and inserted into the equation (1.2.7). Child-Langmuir law in the form of equation (1.2.8) is derived with the assumption that particles are emitted from the plane with zero kinetic energy. If Maxwellian distribution of the emitted particles is assumed, more precise expression for the space-charge-limited current can be taken into account [Mott-Smith and Langmuir, 1926]

$$j = \frac{4}{9}\epsilon_0 \left(\frac{2q}{m}\right)^{\frac{1}{2}} \frac{|U_p - U_s|^{\frac{3}{2}}}{(r_s - r_p)^2} \left[1 + 2.66 \left(\frac{\mathrm{k_B}T}{qU_p}\right)^{\frac{1}{2}}\right]. \tag{1.2.9}$$

Last two equations describe space charge limited emission in the planar geometry. In the case of cylinders, it is more precise to use the expression [Langmuir and Blodgett, 1923]

$$j = \frac{4}{9}\epsilon_0 \left(\frac{2q}{m}\right)^{\frac{1}{2}} \frac{|U_p - U_s|^{\frac{3}{2}}}{r_p^2 \beta^2} \left[1 + 2.66 \left(\frac{\mathrm{k_B}T}{qU_p}\right)^{\frac{1}{2}}\right], \tag{1.2.10}$$

and in the case of spheres [Langmuir and Blodgett, 1924]

$$j = \frac{4}{9}\epsilon_0 \left(\frac{2q}{m}\right)^{\frac{1}{2}} \frac{|U_p - U_s|^{\frac{3}{2}}}{r_p^2 \alpha^2} \left[1 + 2.66 \left(\frac{\mathrm{k_B}T}{qU_p}\right)^{\frac{1}{2}}\right], \tag{1.2.11}$$

where $\beta = \gamma - 0.4\gamma^2 + ...$, $\alpha = \gamma^2 - 0.6\gamma^3 + ...$ and $\gamma = \ln(r_p/r_s)$. These are the so-called Langmuir-Blodgett space-charge equations.

Usually, measurement of plasma density n from electron saturation current is not convenient. The electron saturation current is usually relatively high and can be dangerous for the probe itself. Moreover, the current collected by the probe can be so large that the significant number of electrons is drained from plasma and it can thus significantly change plasma parameters in the surroundings of the probe. Thus, it is much better to derive plasma density n from the ion saturation current. However, interpretation of the ion current part of the IV characteristics can be difficult since the assumptions of the simple OML theory which was described in the previous paragraphs are not usually satisfied and different theories must be applied. As it was derived in the section 1.1.1, the ions must have a drift velocity when entering the sheath and their velocity distribution is not thus purely Maxwellian at the sheath edge. Moreover, in order for the OML theory to be valid, potential variation has to be gentle enough so that there does not exist an "absorption radius" inside of which the electric field is so strong that no charged particles can escape and are collected by the probe. This condition is not satisfied in the case of ions when sheath edge has to be considered far away to include also electric field which imparts the drift velocity to the ions. As a result, ion current is not independent of the potential shape and one must solve the Poisson's equation for the potential distribution in the surroundings of the probe. For spherical probes and cold ions ($T_i = 0$, meaning that there are no orbital motions and all of the ions are approaching the probe radially), it was done by Allen et al. [1957] and their result is recognized as ABR theory. Later, it was extended to the cylindrical probes by Chen [1965b]. Theory which accounts for both sheath formation and orbital motions was formulated by Bernstein and Rabinowitz [1959] who assumed ions of a single energy E_i. The assumption of monoenergetic ions was abandoned by Laframboise [1966] who extended the theory for Maxwellian ion distribution. The theory is now known as BRL theory and it has been verified by numerous experiments in different operating conditions. However, direct application of the BRL theory on the experimental measurements is not easy task since it requires a lot of complicated computations which has to be done numerically. To overcome this complication, different kinds of approximate fits of the BRL theory which can be directly applied to the experimental results were proposed and plasma density can be thus evaluated from the measured ion current for a wide operating range.

In the thin sheath limit approximation ($r_s - r_p \ll r_p$ or $\lambda_D \ll r_p$), which can be considered in sufficiently dense plasma, the ions enter the sheath with Bohm velocity u_B and plasma density n can be evaluated from the expression for the ion saturation current given by

$$I_B = n_s q A_p u_B = 0.61 n q A_p \left(\frac{\mathrm{k_B}T_e}{m_i}\right)^{\frac{1}{2}}, \tag{1.2.12}$$

where n_s denotes plasma density at the sheath edge, A_p is the probe surface and the factor 0.61 comes from the estimation of the potential drop in the presheath region, see equation (1.1.7). The formula (1.2.12) for the Bohm current is often used to determine plasma density from the ion saturation current due to its simplicity. However, application of this approach in low density plasma ($\lambda_D \gg r_p$) can lead to overestimation of plasma density. Therefore, it is recommended to determine plasma density using the BRL theory if $r_p \lesssim 35\lambda_D$ [Bose et al., 2017].

1.2.2 Effects of collisions on the probe measurement

The expressions in the previous chapter were derived based on the assumption that the charged particles do not undergo collision events with the neutral ones. Clearly, such an assumption is not satisfied in plasmas of medium and high pressures. More precisely, collision events have to be considered if the mean free path λ is not considerably larger than the probe radius r_p or if the mean free path is less than the characteristic length λ_D of the potential change in the sheath. In the first case ($\lambda \lesssim r_p$), the probe is large enough that it blocks significant portion of particles arriving at the sheath edge from the direction of the probe and velocity distribution cannot be thus considered as undisturbed here. In the second case ($\lambda \lesssim \lambda_D$), the motion of the particles in the sheath is affected by collisions and it differs from the free-fall motion which was assumed so far. As a result, potential profile and hence probe current is modified.

If the operating pressure of plasma is higher, collisions of charged particles with the neutrals start to appear in the sheath ($\lambda \lesssim \lambda_D$) and their occurence can affect the current collected by the probe in the two major ways in the OML limit (= thick sheath limit, $r_p \lesssim 3\lambda_D$):

- Collisions with neutrals can lead to destruction of the orbital motion of the charged particles. They lose their energy and they are not able to escape from the attractive electrive field. Ultimately, they reach the probe and the probe current is thus increased. It was shown that this effect is dominant when approximately one collision occurs in the sheath region.

- Scattering of the charged particles on the neutrals in the sheath changes direction of their movement and it leads to decrease of the current collected by the probe. This reduction is dominant at higher pressures when multiple collisions appear in the sheath.

One of the first theories that predicted decrease of the ion current due to elastic scattering of ions on the neutral particles in the sheath was the Talbot and Chou theory [Chou et al., 1966], [Talbot and Chou, 1969]. Their theory describes the effect of collisions as a correction to the Laframboise ion current I_L

$$I_i = \gamma I_L,$$

where the correction factor γ depends on the Knudsen number $Kn_i = \lambda_i/r_p$ and anisothermicity parameter $\tau = T_e/T_i$. The first theory which accounted for both the increase of the probe current due to destruction of the orbital motions and the decrease due to elastic scattering was introduced by Zakrzewski and Kopiczynski

[1974]. The authors also speak about the correction of Laframboise current I_L but they introduce two correction factors

$$I_i = \gamma_1 \gamma_2 I_L,$$

where γ_1 stands for the increase of the probe current due to the destruction of the orbital motions and γ_2 for decrease of the probe current due to the scattering on neutrals. The correction factors generally depend on the number of collisions in the sheath and on the current predicted by ABR theory. The theory of Zakrzewski and Kopiczynski is, however, limited to the cases when only few collisions appear within the probe sheath. The extension of their theory was proposed by Tichy et al. [1994] who suggest to use the scaling factor γ given by Talbot and Chou theory for description of the probe current decrease due to scattering on neutrals instaed of the factor γ_2

$$I_i = \gamma_1 \gamma I_L.$$

The model is known as "modified Talbot and Chou" theory and it is valid for any Knudsen number within the OML regime.

In this place, we present some basic considerations of the collision effects on the Langmuir probe measurements which are summarized in the work Chen [1965a]. The situation $\lambda \lesssim r_p$ can be investigated in the case of a probe which is at plasma potential since there are no electric fields to be taken into account. Let A_p be the surface of a probe immersed in a plasma and let A_λ denote surface which is one mean free path λ from the surface of the probe. In the case of isotropic velocity distribution at the surface A_λ ($\lambda \gg r_p$), the random flux crossing the surface A_λ inwards is

$$\Gamma = \frac{1}{4} n_\lambda v_{th},$$

where n_λ is plasma density at the surface A_λ and v_{th} is the thermal velocity. Current on the probe is then

$$I = \frac{1}{4} n_\lambda v_{th} q A_p. \tag{1.2.13}$$

In the case when $\lambda \lesssim r_p$, surfaces A_λ and A_p are close to each other and velocity distribution at A_λ cannot be isotropic since there are no particles coming from the probe. As a result, density n_λ is only half as large and the probe current is

$$I = \frac{1}{2} n_\lambda v_{th} q A_p.$$

Generally, the expression for the probe current can be written in the form

$$I = \frac{n_\lambda v_{th} q A_p}{4K}, \tag{1.2.14}$$

where the constant K varies between $1/2$ and 1, depending on the relative magnitude of A_λ and A_p.

The probe current in presence of collisions can be also evaluated using drift-diffusion approximation of the particle flux

$$\boldsymbol{\Gamma} = \operatorname{sgn}(q)\, \mu n \boldsymbol{E} - D \nabla n,$$

where μ and D are the coefficients of mobility and diffusion. Electric field can be omitted since we assume that the probe is at space potential. Assuming the conservation of the particle flux, we can write

$$\nabla \cdot \boldsymbol{\Gamma} = -D\Delta n = 0.$$

Making an analogy with electrostatics (with Poisson's equation, in particular), the following expression for the probe current can be derived

$$I = qD(n_0 - n_\lambda)\frac{C}{\epsilon_0}, \tag{1.2.15}$$

where n_0 is the undisturbed plasma density and C is the probe capacitance. We now consider the case of spherical probe with radius r_p and we further use the capacitance of a sphere of radius $r_p + \lambda$

$$C = 4\pi\epsilon_0 \left(r_p + \lambda\right).$$

If the two equations (1.2.14) and (1.2.15) for the probe current are now equated and solved for n_λ, we can derive an expression for the probe current in the form

$$I = \frac{1}{4} n_0 v_{th} q A_p \left(\frac{3}{4}\frac{r_p}{\lambda}\frac{r_p}{r_p + \lambda} + K\right)^{-1}, \tag{1.2.16}$$

where the classical diffusion coefficient $D = \lambda v_{th}/3$ was assumed. In the case of large λ/r_p, K is equal to 1 and the expression (1.2.16) simplifies to the equation (1.2.13) for the collisionless random current. In the opposite case ($\lambda \ll r_p$), the equation (1.2.16) becomes

$$I = \frac{1}{4} n_0 v_{th} q A_p \frac{3}{4}\frac{\lambda}{r_p}, \tag{1.2.17}$$

which suggests that the probe current is reduced by approximately a factor λ/r_p due to the collisions.

Let us now consider the case of a cylindrical probe of radius r_p which is at very large potential U_p and mean free path λ is much shorter than the Debye length λ_D, so that the motion of particles is affected by collisions everywhere, including the sheath. Let the probe potential U_p be such that the particle of the first species are collected ($q_1 U_p < 0$) and let U_p be so high that the particles of the second species are Maxwellian. Under these assumptions, the flux of the first particle species can be described by the drift-diffusion approximation

$$\Gamma_1 = -\mathrm{sgn}\left(q_1\right)\mu n_1 \nabla U - D\nabla n_1, \tag{1.2.18}$$

and Poisson's equation can be considered in a form

$$\Delta U = -\frac{q_1}{\epsilon_0}\left[n_1 - n_0 \exp\left(\frac{-q_2 U}{\mathrm{k_B} T_2}\right)\right],$$

where n_0 is density of undistrubed plasma. Since we assume very large potential (large compared to $\mathrm{k_B} T_1$), the diffusion term in the equation (1.2.18) can be neglected. Thus, we get an expression for the number density n_1

$$n_1 = -\frac{\Gamma_1}{\mathrm{sgn}\left(q_1\right)\mu\nabla U},$$

and for the total probe current I per unit length

$$I = -2\pi r \Gamma_1.$$

Considering $q_2 = -q_1$, we can write Poisson's equation in cylindrical coordinates

$$\frac{1}{r}\frac{\mathrm{d}}{\mathrm{d}r}\left(r\frac{\mathrm{d}U}{\mathrm{d}r}\right) = -\frac{q_1}{\epsilon_0}\left[\frac{I}{2\pi r\mu}\left(\frac{\mathrm{d}U}{\mathrm{d}r}\right)^{-1} - n_0 \exp\left(\frac{q_1 U}{\mathrm{k_B} T_2}\right)\right].$$

In dimensionless form, the equation can be written as

$$\frac{1}{\rho}\frac{\mathrm{d}}{\mathrm{d}\rho}\left(\rho\frac{\mathrm{d}\eta}{\mathrm{d}\rho}\right) = -\frac{i}{\rho}\left(\frac{\mathrm{d}\eta}{\mathrm{d}\rho}\right)^{-1} - \exp\left(-\eta\right),$$

where $\eta = -q_1 U/\mathrm{k_B} T_2$, $\rho = r/\lambda_D$, $\lambda_D^2 = \epsilon_0 \mathrm{k_B} T_2/n_0 q_1^2$, $i = I/I_0$ and $I_0 = 2\pi n_0 \mu \mathrm{k_B} T_2/q_1$. Detailed analysis of the asymptotic behavior of the last equation shows that he problem in cylindrical geometry is not well-formulated one. In reality, the current I is not constant with radius due to ionization and end effects, which were neglected in the present analysis. However, the solution of the equation can be still found if we impose a "sheath edge" at some distance from the probe $r = s$ (or in dimensionless units $\rho = \sigma$) and assume that $\mathrm{d}\eta/\mathrm{d}\rho = 0$ here. Further, we will assume that the probe potential is so highthat the density of the second particle species can be neglected. In these condition, the following relation between the probe potential and its current can be derived

$$\eta - \eta_s = i^{\frac{1}{2}}\left\{\left(\sigma^2 - \rho^2\right)^{\frac{1}{2}} - \sigma \log\left[\frac{\sigma}{\rho} + \left(\frac{\sigma^2}{\rho^2} - 1\right)^{\frac{1}{2}}\right]\right\},$$

which can be viewed as the high-pressure equivalent of the Langmuir-Blodgett space-charge equation (1.2.10). If one turns back to the original units, it can be seen that the dependences on $\mathrm{k_B} T_2$ and n_0 cancel out and, apart from the geometric factor, the current I is proportional to $(U - U_s)^2$ as opposed to $(U - U_s)^{3/2}$ dependence in the collisionless case (1.2.10). A similar procedure for finding the relationship between the probe current and voltage can be applied also in the case of the spherical probe; however, the final integration can be done only numerically.

2. Computer modelling in plasma physics

Computer modelling techniques which are commonly used in plasma physics research are based on the Boltzmann equation for the phase space distribution function $f_i(\boldsymbol{x}, \boldsymbol{v}, t)$ of the particular particle species present in the plasma

$$\frac{\partial f_i}{\partial t} + \boldsymbol{v} \cdot \frac{\partial f_i}{\partial \boldsymbol{x}} + \frac{q}{m} \left(\boldsymbol{E} + \boldsymbol{v} \times \boldsymbol{B} \right) \cdot \frac{\partial f_i}{\partial \boldsymbol{v}} = \left[\frac{\partial f_i}{\partial t} \right]_{coll} .$$

There are multiple approaches to the solution of this equation. The most general are *kinetic models* whose subject is the direct solution of the Boltzmann equation. However, such an approach leads to computationally very demanding calculations since the distribution function is defined in 6D space (3 velocity + 3 spatial coordinates). Moreover, the collision term $[\partial f_i / \partial t]_{coll}$ might be of complicated forms what further makes the calculations difficult. Another approach to the solution of the Boltzmann equation are the so-called *particle models* (Particle-in-Cell method in particular). Their principle consists in sampling of the phase space by numerical superparticles which cover only the most important parts of the phase space and thus keep the kinetic information of the modelled particle ensemble while reducing the computational demands. The advantage of the particle models over the kinetic ones is schematically illustrated in the figure 2.1. If appropriate assumptions on the distribution function in the velocity space are made, velocity moments of the Boltzmann equation can be calculated and the so-called *fluid models* are derived. Sometimes, the advantages of the above mentioned modelling techniques are combined into the so-called *hybrid models*. In the proposed thesis, we focus mainly on the Particle-in-Cell method in the chapter 2.1 and on the fluid models in the chapter 2.2.

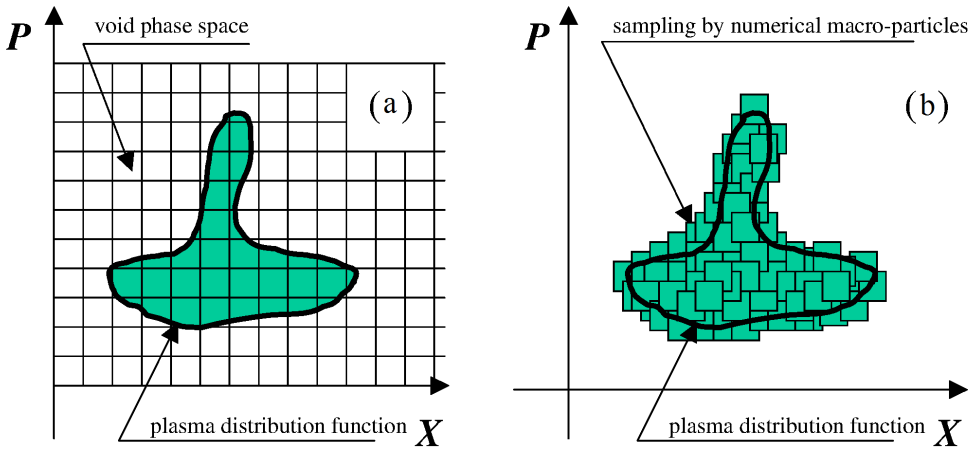

Figure 2.1: Difference between (a) direct solution of the Boltzmann equation and (b) Particle-In-Cell method which uses numerical superparticles for sampling of the phase space. The figure is taken from the article Pukhov [2016].

2.1 Particle-in-Cell (PIC) method

2.1.1 Motivation

Strongly and weakly coupled systems Definition of strongly and weakly coupled systems [Colonna and D'Angola, 2016, Chapter 4.1]:

- Plasma parameter Λ

$$\Lambda = 4\pi n \lambda_D^3.$$

- Number of charged particles in the Debye sphere N_D

$$N_D = \frac{4\pi}{3} n \lambda_D^3 = \frac{4\pi}{3} n \left(\frac{\epsilon_0 k_B T}{q^2 n} \right)^{\frac{3}{2}} = \frac{4\pi}{3} \frac{(\epsilon_0 k_B T)^{\frac{3}{2}}}{q^3 n^{\frac{1}{2}}},$$
$$N_D^{\frac{2}{3}} = \left(\frac{4\pi}{3} \right)^{\frac{2}{3}} \frac{\epsilon_0 k_B T}{q^2 n^{\frac{1}{3}}}.$$

- Plasma coupling parameter Γ is defined as a ratio of electrostatic potential energy $E_P = \frac{q^2}{4\pi\epsilon_0 a}$ [$a = \left(\frac{3}{4\pi n}\right)^{\frac{1}{3}}$ is Wigner-Seitz radius which is the characteristic measure of interparticle distance] to the thermal energy $E_T = k_B T$

$$\Gamma = \frac{E_P}{E_T} = \frac{q^2}{4\pi\epsilon_0 a k_B T} = \frac{1}{4\pi} \left(\frac{4\pi}{3} \right)^{\frac{1}{3}} \frac{q^2 n^{\frac{1}{3}}}{\epsilon_0 k_B T} =$$
$$= \frac{1}{4\pi} \left(\frac{4\pi}{3} \right)^{\frac{1}{3}} \left(\frac{4\pi}{3} \right)^{\frac{2}{3}} \frac{1}{N_D^{\frac{2}{3}}} = \frac{1}{3} \frac{1}{N_D^{\frac{2}{3}}}.$$

- System of charged particles is **strongly coupled** if N_D is small (Γ is large) and **weakly coupled** if N_D is large (Γ is small).

- **Strongly coupled system** - only few charged particles in Debye sphere; potential energy dominates over the thermal energy. Evolution of this system is driven by pairwise electrostatic interactions (collisions) between the charged particles. Relative configuration of any two pairs of particles strongly affects behavior of the system.

- **Weakly coupled system** - large number of particles in Debye sphere; thermal energy dominates over the potential energy. Trajectory of a particle is only little influenced by interactions with other particles since the field in its position is given by superposition of many contributions.

Low temperature plasma and plasma in magnetic fusion devices are examples of weakly coupled systems. The number of particles in the volume of interest in the weakly coupled system is quite large and it is not possible from the computational point of view to follow every single particle in the system. However, the nature of the weakly coupled system allows to make the computational effort manageable by using the *finite-size* particle approach.

Finite-size particles In the weakly coupled systems, charged particles can be viewed as they interact rather with smooth background field than through pairwise interactions (collision). Therefore, there is no need to model mutual interactions of all particles in the system. In that perspective, the so-called *computational particles* or *super-particles* which represent clouds of real particles can be used instead. Computational particles interact more weakly than point particles (figure 2.2): at large distances they interact according to the Coulomb force law; however, when the computational particles start to overlap the force between them decreases since the overlapping area does not contribute to the resultant force and becomes zero at zero distance between the computational particles. Thus, the usage of finite-size particles allows to describe the system by lower number of particles while keeping the nature of weakly coupled system.

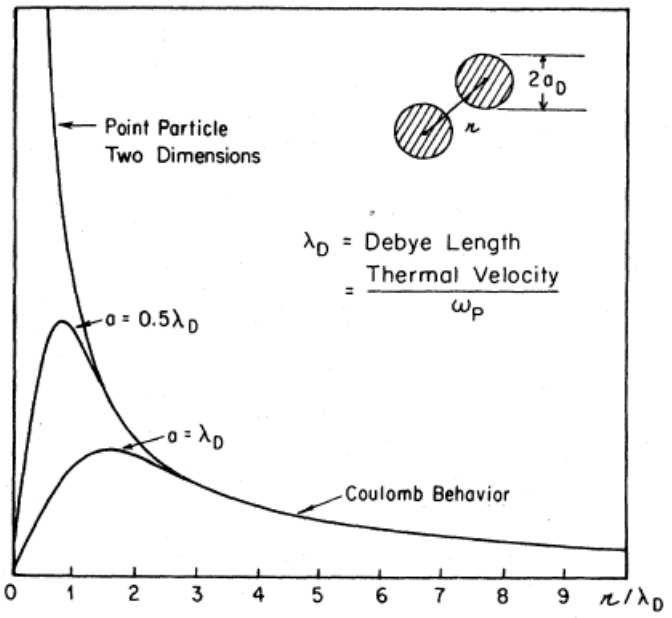

Figure 2.2: Force law between finite-size particles in two dimensions for particles of various size. A Gaussian-shaped charge density profile was used. Taken from the article Dawson [1983].

2.1.2 Theory

Description of the Particle-in-Cell method in this paragraph is based on the derivation which is given in the article Lapenta [2012]. At this place, the Particle-in-Cell method is described in absence of collisions between the charged particles and the neutrals. However, the PIC models are often supplemented by Monte Carlo collision (MCC) modules which account for the collision effects. This is described in more detail in the section 3.2.4.

Let us consider Vlasov equation for the phase space distribution function $f(\boldsymbol{x}, \boldsymbol{v}, t)$ of a given charged particle species,

$$\frac{\partial f}{\partial t} + \boldsymbol{v} \cdot \frac{\partial f}{\partial \boldsymbol{x}} + \frac{q}{m} (\boldsymbol{E} + \boldsymbol{v} \times \boldsymbol{B}) \cdot \frac{\partial f}{\partial \boldsymbol{v}} = 0.$$

In the view of the PIC method, the distribution function can be regarded as a superposition of N_s moving elements of phase space, the so-called superparticles, which represent clouds of N_p physical particles,

$$\begin{aligned} f(\boldsymbol{x}, \boldsymbol{v}, t) &= \sum_{i=1}^{N_s} f_i(\boldsymbol{x}, \boldsymbol{v}, t), \\ f_i(\boldsymbol{x}, \boldsymbol{v}, t) &= N_p S_{\boldsymbol{x}} \left(\boldsymbol{x} - \boldsymbol{x_i}\right) S_{\boldsymbol{v}} \left(\boldsymbol{v} - \boldsymbol{v_i}\right). \end{aligned} \tag{2.1.1}$$

$S_{\boldsymbol{x}}$, $S_{\boldsymbol{v}}$ are the superparticle shape functions and $(\boldsymbol{x_i}, \boldsymbol{v_i})$ is time dependent vector of superparticle position in the phase space.

There are several requirements which the shape functions should satisfy:

1. The support of the shape function is compact, so it describes only a small portion of the phase space.

2. The integral over any direction ξ of the phase space is unitary:

$$\int_{V_\xi} S_\xi \left(\xi - \xi_i\right) \mathrm{d}\xi = 1.$$

3. The shape function is symmetric:

$$S_\xi \left(\xi - \xi_i\right) = S_\xi \left(\xi_i - \xi\right).$$

The common choice of the shape function in the velocity space is Dirac's delta in each direction:

$$S_{\boldsymbol{v}} = \delta \left(v_x - v_{xi}\right) \delta \left(v_y - v_{yi}\right) \delta \left(v_z - v_{zi}\right).$$

It means that the physical particles which are represented by the computational superparticle have the same velocity and they remain close in the phase space during the time evolution. Obviously, it is an approximation since the shape function which initially correctly discretizes phase space would be distorted by electric and magnetic fields during the time evolution in reality. This effect is neglected by the PIC method.

The common choice for the spatial shape functions are the so-called b-splines which are a series of consecutively higher order functions obtained from each other by integration. The zero order b-spline function is the flat-top function $b_0(\xi)$:

$$\begin{aligned} b_0(\xi) &= 1 \quad \text{for } |\xi| < \frac{1}{2}, \\ &= 0 \quad \text{otherwise.} \end{aligned}$$

Higher order b-splines are obtained by integration:

$$b_l(\xi) = \int_{-\infty}^{\infty} b_0(\xi - \xi') b_{l-1} \xi' \mathrm{d}\xi'. \tag{2.1.2}$$

The spatial shape function based on the b-splines which is used in the PIC method is defined as:

$$S_{\boldsymbol{x}}(\boldsymbol{x} - \boldsymbol{x_i}) = \frac{1}{\Delta x_i \Delta y_i \Delta z_i} b_l \left(\frac{x - x_i}{\Delta x_i}\right) b_l \left(\frac{y - y_i}{\Delta y_i}\right) b_l \left(\frac{z - z_i}{\Delta z_i}\right),$$

where Δx_i, Δy_i, Δz_i are the sizes of the superparticles in each direction. The most common choice for spatial shape function is the b-spline of the zero order – it leads to the PIC method implementation which is referred as Cloud-in-Cell (CIC).

To derive equations of motion for superparticles, we take first velocity moments of the Vlasov equation with distribution function in a form (2.1.1). Derivation is described in the article Lapenta [2012] in detail. As a result, we get the following set of equations

$$\begin{aligned} \frac{\mathrm{d}\boldsymbol{x_i}}{\mathrm{d}t} &= \boldsymbol{v_i}, \\ \frac{\mathrm{d}\boldsymbol{v_i}}{\mathrm{d}t} &= \frac{q}{m}\left(\boldsymbol{E_i} + \boldsymbol{v_i} \times \boldsymbol{B_i}\right), \end{aligned}$$

where $i = 1, ..., N_s$ and $\boldsymbol{E_i}$, $\boldsymbol{B_i}$ are the electric and magnetic field in the position of the superparticle. The equations of motion for superparticles have the same form as the equations of motion for the real physical particles.

As the cases which are investigated by the developed PIC code in the further sections allow us to use electrostatic approximation of the Maxwell's set of equations, the equations of motion for the superparticles are coupled only with the equation for the electric field:

$$\nabla \cdot \boldsymbol{E} = \frac{\rho}{\epsilon_0}.$$

The equation for electric field is solved on the discrete calculation grid. The situation is a lot simplified if the grid is chosen as uniform, Cartesian and with cell sizes in each direction equal to particle sizes: $\Delta x_g = \Delta x_i = \Delta x$, $\Delta y_g = \Delta y_i = \Delta y$, $\Delta z_g = \Delta z_i = \Delta z$.

We assume that the motion of the superparticles can be still affected by the constant external magnetic field which then figures in the right-hand-side of the velocity equation for the superparticle.

Solution of the equations of motion provide spatial distribution of the superparticles and thus, spatial distribution of the charge density is obtained. On the other hand, the calculated electric field is used in the equation of motion for the superparticles. The following equations which relate quantities at grid points (marked with index g) with those at the superparticle position (marked with index i) can be derived [Lapenta, 2012]

$$\rho_g = \frac{qN_p}{\Delta x \Delta y \Delta z} \sum_{i=1}^{Ns} W(\boldsymbol{x_g} - \boldsymbol{x_i}),$$

$$\boldsymbol{E_i} = \sum_g \boldsymbol{E_g} W(\boldsymbol{x_g} - \boldsymbol{x_i}),$$

where

$$W(\boldsymbol{x_g} - \boldsymbol{x_i}) = b_{l+1}\left(\frac{x_g - x_i}{\Delta x}\right) b_{l+1}\left(\frac{y_g - y_i}{\Delta y}\right) b_{l+1}\left(\frac{z_g - z_i}{\Delta z}\right).$$

For the most common CIC scheme of the PIC method ($l = 0$), it means linear interpolation between the grid points and superparticle positions.

2.1.3 Stability

The following conditions should be satisfied so that the PIC simulation provides correct and reliable results.

Stability of the explicit time differencing The von Neumann stability analysis for the explicit time differencing leap-frog algorithm for the discretization of the equations of motion [Lapenta, 2012] leads to the condition

$$\omega_p \Delta t < 2,$$

where $\omega_p = \left(\frac{e^2 n_e}{\epsilon_0 m_e}\right)^{\frac{1}{2}}$ is plasma frequency. If the condition is not met, the numerical solution becomes unstable and significant numerical heating of the particles which discards the results appears. It is advised that the time step is even smaller: $\omega_p \Delta t = 0.1$.

Finite grid instability The usage of discrete computational grid is characteristic for the Particle-In-Cell method. The grid is used for calculation of the electromagnetic fields, which values are then interpolated to the particle positions. The particles move in continuum space but their information is projected onto the grid in order to obtain the source terms for the electromagnetic field solution. Thus, part of the information carried by the particles is lost (in particular, it leads to grid aliasing of high-frequency modes, which are not resolved by the grid, to low frequencies) and the so-called finite grid instability can appear. The detailed mathematical analysis of this phenomena was given in the works of Birdsall and Langdon [1991] and Hockney and Eastwood [1988]. In order to avoid the finite grid instability, which also causes numerical heating of the moving particles, the following condition has to be satisfied

$$\frac{\Delta x}{\lambda_D} < C,$$

where λ_D is the Debye length, Δx is the size of the computational grid cell and C is a constant ($C = \pi$ for CIC scheme).

Courant-Friedrichs-Lewy (CFL) condition In our work, we are dealing only with electrostatic PIC simulations; thus, the classical CFL condition for electromagnetic wave propagation ($c\Delta t/\Delta x < 1$) does not have to be satisfied. However, in order that the motion of a charged particle was sufficiently precisely described, we require that the particle does not move (in average) more than 1 cell of the computational mesh per a time step, which leads to a condition similar to the CFL condition:

$$\frac{v \Delta t}{\Delta x} < 1,$$

where v is a characteristic velocity of the particles (e. g. thermal velocity).

Number of superparticles per Debye sphere It was already stated that PIC simulations are intended for weakly coupled systems where there is large number of real physical particles per Debye sphere ($N_D \gg 1$). It is also required

that there is sufficiently large number of computational superparticles per Debye sphere [Hockney and Eastwood, 1988] (in order that there are a sufficiently large number of computational superparticles in the range of velocities near the phase velocity of unstable waves)

$$\frac{N_s}{V}\frac{4}{3}\pi\lambda_D^3 \gg 1.$$

Collisions of superparticles If the number of superparticles per a computational grid cell is too low, the fluctuations of number of superparticles per a grid cell during their movement can lead to large, random fluctuations of electric potential leading to a large local electric field on which the superparticles are scattered off. It was shown that this effect can lead to significant artificial heating (e. g. [Hockney and Eastwood, 1988], [Ueda et al., 1994], [Cormier-Michel et al., 2008]) and that the following condition is necessary:

$$\frac{N_s}{N_c} \gg 1,$$

where N_c is the total number of the computational grid cells.

Characteristic size and time of the simulation In addition, we impose several other conditions regarding the characteristic size L of the computational domain and the total time T of the simulation. It is required that the characteristic length L is much larger than the Debye length λ_D

$$L \gg \lambda_D.$$

Further, it is required that the length of the path which the charged particle moves after the whole time interval T of the simulation is comparable to the characteristic length L so that the initial solution (density and velocity distribution of the particles) can evolve into the meaningful final solution

$$vT > L.$$

Finally, it is required that the length of the path of the charged particle movement between two times (T_{avg}) when the current solution is taken as a statictical sample for the subsequent averaging is larger then the computational cell size Δx so that the statistical samples are independent

$$vT_{avg} > \Delta x.$$

2.2 Fluid models

Under the assumption of the local thermodynamic equilibrium, plasma can be considered as a continuum and can be described by spatial distribution of macroscopic quantities which are the velocity moments of the phase space distribution function $f(\boldsymbol{x}, \boldsymbol{v}, t)$ of a given charged particle species. Usually, first three velocity

moments are used for plasma description – number density n, flux $\boldsymbol{\Gamma}$ and energy ϵ:

$$n(t,\boldsymbol{x}) = \int f(t,\boldsymbol{x},\boldsymbol{v})\mathrm{d}\boldsymbol{v},$$
$$\boldsymbol{\Gamma}(t,\boldsymbol{x}) = n\boldsymbol{u}(t,\boldsymbol{x}) = \int \boldsymbol{v} f(t,\boldsymbol{x},\boldsymbol{v})\mathrm{d}\boldsymbol{v},$$
$$\epsilon(t,\boldsymbol{x}) = \frac{1}{2}mn\int v^2 f(t,\boldsymbol{x},\boldsymbol{v})\mathrm{d}\boldsymbol{v}.$$

The zero velocity moment is obtained by pure integration over the velocity subspace of the phase space

$$\int \frac{\partial f}{\partial t}\mathrm{d}\boldsymbol{v} + \int \boldsymbol{v}\cdot\frac{\partial f}{\partial \boldsymbol{x}}\mathrm{d}\boldsymbol{v} + \frac{q}{m}\int (\boldsymbol{E}+\boldsymbol{v}\times\boldsymbol{B})\cdot\frac{\partial f}{\partial \boldsymbol{v}}\mathrm{d}\boldsymbol{v} = \int \left[\frac{\delta f}{\delta t}\right]_{coll}\mathrm{d}\boldsymbol{v},$$

which leads to the continuity equation

$$\frac{\partial n}{\partial t} + \nabla\cdot(n\boldsymbol{u}) = I - R, \tag{2.2.1}$$

where the terms I and R describe production and loss of the charged particles due to the collision processes. Similarly, the first velocity moment of the Boltzmann equation can be obtained which leads to the equation of momentum conservation. In a general form, it can be written as

$$\frac{\partial(mn\boldsymbol{u})}{\partial t} + \nabla\cdot(mn\boldsymbol{u}\otimes\boldsymbol{u}) = qn(\boldsymbol{E}+\boldsymbol{u}\times\boldsymbol{B}) - \nabla\cdot\mathbb{T} + \boldsymbol{C}, \tag{2.2.2}$$

where $\mathbb{T}$ denotes the stress tensor, $\boldsymbol{C}$ express the momentum balance during the collision processes and operator $\otimes$ stands for the tensor product of two vectors. Stress tensor describes pressure which is a consequence of the thermal motion of the charged particles. Generally, the components of the stress tensor can be written as

$$T_{kl} = mn\overline{w_k w_l} = mn\int w_k w_l f(\boldsymbol{v})\mathrm{d}\boldsymbol{v},$$

where w_k is a component of the chaotic thermal velocity $\boldsymbol{w}$ which is given by expression

$$\boldsymbol{v} = \boldsymbol{u} + \boldsymbol{w} = \frac{1}{n}\int \boldsymbol{v} f(t,\boldsymbol{x},\boldsymbol{v})\mathrm{d}\boldsymbol{v} + \boldsymbol{w}.$$

Generally, the non-diagonal terms of the stress tensor are related to the viscosity of the particular fluid. In case of plasma, it is very small and the non-diagonal terms can be thus neglected. If take into account the assumption of an isotropic and Maxwellian velocity distribution function and if we consider plasma as an ideal gas (pressure $p = nk_BT$), the stress tensor $\mathbb{T}$ can be written in a very simple form

$$\mathbb{T} = p\mathbb{I},$$

where $\mathbb{I}$ is the identity tensor.

The second velocity moment of the Boltzmann equation leads to the energy conservation equation which can be written as

$$\frac{\partial\epsilon}{\partial t} + \nabla\cdot(\epsilon\boldsymbol{u}) = qn\boldsymbol{u}\cdot\boldsymbol{E} - \nabla\cdot(\mathbb{T}\cdot\boldsymbol{u}) - \nabla\cdot\boldsymbol{q} + S, \tag{2.2.3}$$

where ϵ is energy density, $\boldsymbol{q}$ is thermal flux and the term S expresses energy change due to the collision proceses. We can write the following relations:

$$\epsilon = \left(\frac{mnu^2}{2} + e\right), \qquad e = \frac{mn}{2}\overline{w^2}, \qquad \boldsymbol{q} = \frac{mn}{2}\overline{w^2\boldsymbol{w}},$$

where e is internal energy which is (as well as thermal flux $\boldsymbol{q}$) given by the chaotic thermal velocity $\boldsymbol{w}$.

Equations (2.2.1), (2.2.2), (2.2.3) together with Maxwell equations for electromagnetic field create a system of equations for the unknown macroscopic variables $n, \boldsymbol{u}, p, \epsilon, \boldsymbol{E}, \boldsymbol{B}$ and constitute magneto-hydrodynamic model in a general form. The system can be further simplified if additional assumptions are taken into account.

Drift-diffusion approximation Taking into account several assumptions, the equation of momentum conservation (2.2.2) can be simplified to the so-called drift- diffusion approximation which is applicable to the modelling of low-temperature plasma in regimes when the collision processes are dominant. Under the assumption of isotropic Maxwell velocity distribution, the momentum conservation equation (without magnetic field) can be written in the form

$$nm\left(\frac{\partial \boldsymbol{u}}{\partial t} + \boldsymbol{u}\cdot\nabla\boldsymbol{u}\right) = qn\boldsymbol{E} - \nabla p + C. \tag{2.2.4}$$

The pressure term can be written in the form $p = n\mathrm{k_B}T$ and momentum change caused by collision events in the form $C = -nm\nu\boldsymbol{u}$, where ν is the collision frequency. The term $\frac{\partial \boldsymbol{u}}{\partial t}$ is equal to zero in the steady state analysis. In the case of low-temperature plasma, the drift velocity $\boldsymbol{u}$ of electrons is much smaller than the thermal velocity. Moreover, the mass of electrons is very low. As a result, the second term on the left side of the equation (2.2.4), which expresses the inertia, can be neglected in the case of electrons. This leads to the equation for particle flux $\boldsymbol{\Gamma}$ $[\mathrm{m}^{-2}\cdot\mathrm{s}^{-1}]$

$$\boldsymbol{\Gamma} = n\boldsymbol{u} = \frac{qn\boldsymbol{E} - \nabla(n\mathrm{k_B}T)}{m\nu} = \mathrm{sgn}\,(q)\,\mu n\boldsymbol{E} - D\nabla n, \tag{2.2.5}$$

where the last equality holds in the case of constant temperature distribution in the space. The equation (2.2.5) suggests that the flux of charged particles is caused by electric field (drift) and by gradient of number density (diffusion). Coefficients μ and D are mobility and diffusion coefficients, respectively, and describe transport of charged particles

$$\mu = \frac{|q|}{m\nu}, \quad D = \frac{\mathrm{k_B}T}{m\nu}. \tag{2.2.6}$$

The equation (2.2.5) is derived using several assumptions which are valid only for electrons. However, the drift-diffusion approximation is often used also for description of positive ions. This approach is not universally applicable since the mass of ions is much larger. Drift-diffusion approximation brings sufficiently precise results in the cases when the collision frequency of ions is high enough (i. e. bulk plasma). In such conditions, positive ions are not enough to get during the time between subsequent collisions to the area where $\boldsymbol{E}$ and ∇p have different

values. As a result, convective derivation on the left side of the equation (2.2.4) can be neglected also in the case of positive ions. One has to be very careful if the drift diffusion approximation is to be used for modelling of the sheath layer since its characteristic size, Debye length, might be smaller than the mean free path, depending on the plasma parameters.

Two-term approximation The two-term approximation is a more general approach to the solution of the Boltzmann equation

$$\nabla_r \cdot (\boldsymbol{v} f) + \frac{\partial}{\partial \boldsymbol{v}} \cdot \left(\frac{q\boldsymbol{E}}{m} f \right) = \left(\frac{\partial f}{\partial t} \right)_c , \tag{2.2.7}$$

than the drift-diffusion approximation presented in the previous paragraph. It is based on an assumption that the distribution function f is developed in spherical harmonics, of which only the first two terms are considered

$$f(r, \boldsymbol{v}) \simeq f^0(r, v) + \frac{\boldsymbol{v}}{v} \cdot \boldsymbol{f^1}(r, v), \tag{2.2.8}$$

where f^0 and $\boldsymbol{f^1}$ are the isotropic and the anisotropic component of the distribution function f and $\int_0^\infty f^0(r, v) 4\pi v^2 \mathrm{d}v = n(r)$. Such an approach is valid when the distribution function exhibits only small anisotropic deviations from the isotropic solution in both configuration and velocity space. At this place, we present derivation of the two-term approximation only briefly, more details can be found e. g. in the article Alves [2007]. The model is commonly applied to an axially infinite cylindrical discharge maintained by a constant axial electric field, so that equations become one-dimensional in the radial position r. Total electric field can be thus written as $\boldsymbol{E}(r) = E_r(r)\boldsymbol{e}_r + E_z \boldsymbol{e}_z$, where E_z is the axial applied field and E_r is the radial space-charge field.

Substituting the approximation (2.2.8) into the Boltzmann equation (2.2.7) one gets development for each of its terms:

$$\nabla_r \cdot (\boldsymbol{v} f) \simeq \frac{v}{3} \nabla_r \cdot \boldsymbol{f^1} + \boldsymbol{v} \cdot \nabla_r f^0, \tag{2.2.9}$$

$$\frac{\partial}{\partial \boldsymbol{v}} \cdot \left(\frac{q\boldsymbol{E}}{m} f \right) \simeq \frac{1}{3v^2} \frac{\partial}{\partial v} \left[\frac{qv^2}{m} \left(\boldsymbol{E} \cdot \boldsymbol{f^1} \right) \right] + \frac{q\boldsymbol{E}}{m} \cdot \frac{\boldsymbol{v}}{v} \frac{\partial f^0}{\partial v}, \tag{2.2.10}$$

$$\left(\frac{\partial f}{\partial t} \right)_c \simeq \left(\frac{\partial f^0}{\partial t} \right)_{elastic} + \left(\frac{\partial f^0}{\partial t} \right)_{inelastic} - \nu_c \frac{\boldsymbol{v}}{v} \cdot \boldsymbol{f^1}, \tag{2.2.11}$$

where

$$\left(\frac{\partial f^0}{\partial t} \right)_{elastic} \simeq \frac{m}{M} \frac{1}{v^2} \frac{\partial}{\partial v} \left(\nu_c v^3 f^0 \right), \tag{2.2.12}$$

$$\left(\frac{\partial f^0}{\partial t} \right)_{inelastic} \simeq \left(k - \nu_x - \nu_i \right) f^0. \tag{2.2.13}$$

Here, M is the mass of neutral particles, ν_c is the momentum-transfer collision frequency, ν_x is the collision frequency for total excitation, ν_i is the collision frequency for ionization and k represents re-introduction of charged particles in the distribution after inelastic collisions. After regrouping terms in equations

(2.2.9) – (2.2.13), the Boltzmann equation decouples into scalar equation in f^0 and vector equation in $\boldsymbol{f^1}$

$$\frac{v}{3}\nabla_r \cdot \boldsymbol{f^1} - \frac{1}{v^2}\frac{\partial}{\partial v}\left(\frac{m}{M}\nu_c v^3 f^0 - \frac{qv^2}{3m}\boldsymbol{E}\cdot\boldsymbol{f^1}\right) = \left(k - \nu_x - \nu_i\right), \tag{2.2.14}$$

$$\nu_c \boldsymbol{f^1} = -v\nabla_r f^0 - \frac{q}{m}\boldsymbol{E}\frac{\partial f^0}{\partial v}. \tag{2.2.15}$$

The left hand side of the first equation contains terms which represent divergence of the particle flux in configuration and in velocity space, which accounts for the fluxes driven by the total electric field and by collision effects. The particle flux in configuration space in the second equation is given by a diffusion gradient term and by an electric drift term.

The continuity equation is obtained by integrating equation (2.2.14) over the velocity space taking into account condition

$$\int_0^\infty k f^0 4\pi v^2 \mathrm{d}v = n_e\left[\langle\nu_x\rangle + 2\langle\nu_i\rangle\right].$$

Performing the integration, one gets

$$\nabla_r \cdot \int_0^\infty \boldsymbol{f^1}\frac{4\pi v^3}{3}\mathrm{d}v = n_e\langle\nu_i\rangle, \tag{2.2.16}$$

since the term of divergence in velocity space vanishes by using Green's theorem. The integral on the left-hand side represents the total particle flux and it can be obtained using equation (2.2.15)

$$\begin{aligned}\Gamma_r &\equiv \int_0^\infty f_r^1\frac{4\pi v^3}{3}\mathrm{d}v = -\nabla_r\left(Dn\right) + \mathrm{sgn}(q)\mu n E_r, \\ \Gamma_z &\equiv \int_0^\infty f_z^1\frac{4\pi v^3}{3}\mathrm{d}v = \mathrm{sgn}(q)\mu n E_z,\end{aligned} \tag{2.2.17}$$

where Γ_r and Γ_z are the radial and axial components of the total flux $\boldsymbol{\Gamma}$ and quantities D and μ are diffusion coefficient and mobility, respectively, which are given by

$$D(r)n(r) \equiv \int_0^\infty \frac{v^2}{3\nu_c(v)} f^0\left(r,v\right) 4\pi v^2 \mathrm{d}v, \tag{2.2.18}$$

$$\mu(r)n(r) \equiv \int_0^\infty \frac{|q|v}{3m\nu_c(v)}\frac{\partial f^0\left(r,v\right)}{\partial v} 4\pi v^2 \mathrm{d}v \tag{2.2.19}$$

Finally, the continuity equation can be written based on the equations (2.2.16) and (2.2.17) as

$$\nabla_r \cdot \boldsymbol{\Gamma}_r = n\langle\nu_i\rangle. \tag{2.2.20}$$

In summary, the description of the particle transport includes the continuity equation (2.2.20) and the momentum transfer equation (2.2.17) whose solution is density n and particle flux $\boldsymbol{\Gamma}$.

3. Developed plasma models

In this section, we present computer models which were applied to obtain physical results that are presented in the section 4. The 2D PIC/MCC code was developed within the diploma thesis Hromádka [2013], the other models were built within the work on the proposed doctoral thesis.

3.1 Particle 2D PIC/MCC code

The 2D PIC/MCC code was developed and described in detail in the thesis Hromádka [2013]. Thus, we bring only very brief description of the code at this place.

The code is written in C programming language and takes advantage of the procedural programming techniques. It is a 2d3v electrostatic model of argon plasma; the code resolves motion of charged particles in the background created by neutral argon atoms and in the presence of generally biased solids immersed in the modelled plasma. The code works with electrons and positive argon ions Ar^+; optionally, negative oxygen ions O^-, which are the most dominant negative ion species in oxygen plasma, can be also included in the simulation and a very simple model of Ar/O_2 plasma can be thus created and investigated. The charged particles can undergo several types of collision events with the neutrals: elastic scattering, excitation, ionization or charge exchange event. Collision events are resolved according to the modified null collision method which is described in detail in the article Roucka and Hrach [2011]. The model works on a rectangular computational domain which is discretized by cartesian computational mesh. Poisson equation is resolved by finite difference method using the central difference scheme. The resultant sparse linear system of equations is solved by means of UMFPACK library [Davis, 2004] which takes advantage of the unsymmetric multifrontal method. Zero Dirichlet boundary condition is prescribed on the outer boundary of the computational domain which represents interface with the bulk plasma. Generally, non-zero Dirichlet boundary conditions are prescribed on the surfaces of the solids which are immersed into the computational domain. In case of cylindrical probes, discretization scheme is adjusted in such a way that its curved surface is approximated with second order of accuracy. This is achieved by moving the particular nodes of the cartesian computational mesh onto the curved boundary of the probe. The immersed solids are considered as perfectly absorbing, no secondary emission is supposed. The computational domain is surrounded by the source of the charged particles with Maxwellian velocity distribution. Cloud-in-Cell algorithm is employed for the collection of the charge density and velocity Verlet algorithm is used for time integration of the equations of motion of the charged particles. The code was used to investigate only the steady state cases; this allowed us to use different time steps of the simulation for different particle species to speed up the needed calculation time.

Characteristic parameters of the simulations

- Typical size of computational grid: (400×400) cells

- Typical number of charged particles: 2.0×10^6 particles (≈ 12 particles per cell)
- Typical dimensions of the computational domain: $(4.0 \times 4.0) \times 10^{-2}$ m
- Typical number of simulated time steps: $(2 - 5) \times 10^5$ time steps to reach steady state, additional $(1 - 2) \times 10^5$ time steps to collect stochastic samples and get averaged results
- Typical duration of 1 time step: 0.5 s
- Typical clock time of a simulation run: $(42 - 97)$ hours

3.2 Particle 3D PIC/MCC code

3.2.1 Code characteristics

The 3D particle code which was developed within the framework of the proposed thesis is based on the explicit Particle-In-Cell method (PIC) with Monte Carlo implementation of the collision module (MCC). The code was developed in C++ programming language and takes advantage of object-oriented programming techniques. The code has altogether 8 380 lines of the source code and it is supplied with a package of Python scripts for post-postprocessing of the results.

The developed model is able to work with an arbitrary number of the charged particle species. An arbitrary number of collision types can be defined for each charged particle species and these might happen with an arbitrary number of neutral species. Energy dependent collision cross sections are provided to the code by means of text files. Collision events can happen not only in the computational domain but also in the source of the charged particles so that the distribution function of the particles which enter the computational domain can be in general non-maxwellian. The code works with regular Cartesian computational mesh and only probes of rectangular shapes can be modelled. The code is written in a very modular way so that its modifications can be done easily, e. g. adding a new probe type or import of electric field which was calculated outside the developed PIC code (an extension towards the hybrid modelling techniques). The only part of the code which is parallelized is the Poisson solver.

The code works with the following C++ classes:

- `Initializer` – it is a container where all input parameters of the code are stored and with the help of which the values of input parameters are delivered to the particular other objects. It has a method which allows reading of the input parameters from a configuration file.
- `Simulation` – it is a class which is responsible for performing the main time cycle of the calculation. It calls the methods of the particular objects in the order which corresponds to the classical PIC/MCC scheme: 1. Update the positions of the charged particles, 2. Solution of the Poisson equation, 3. Update the velocities of the charged particles, 4. Collisions with the neutrals, 5. Post-processing methods.

- `Particle` – it is the basic data structure of the code. It contains information about the position and velocity of the particular charged particle. Physical properties of the charged species (e.g. mass, charge) which are represented in the simulation are stored as static variables of this class.

- `Bulk` – it represents a volume which is filled with the ensemble of the particles and where their movement takes place. It has two subclasses implemented:

  - `Domain` – it resolves the movement of the charged particles in the self-consistent electrostatic field which is provided by Poisson solver. It also has multiple methods which allow to obtain different kinds of post-processing quantities.
  - `Source` – it does not have the Poisson solver implemented. Charged particles do not mutually interact, their movement can be affected only by uniform external electric field.

- `Mesh` – it represents regular Cartesian mesh which is used by the Poisson solver. It has methods for interpolation of the respective quantities between the particle positions and the mesh nodes.

- `Scatter` – it implements methods which resolve collisions of the charged particles with the neutral ones. The implementation of the collision module is described in detail in the chapter 3.2.4.

- `Probe` – it represents metal probes which are immersed into the modelled plasma. It implements methods which ensure that the particles which land on the probe are excluded from the modelled ensemble of particles and methods for calculation of the current density on the probe. It has multiple subclasses which implement probes of different geometries:

  - `Wall` – it is a model of an infinitely large planar probe which can be assigned to an outer face of the computational domain with the modelled plasma.
  - `Rectangular` – it is a model of a 3D probe of a rectangular shape which can be immersed inside the computational domain.

The 3D PIC/MCC code was developed in Microsoft Visual Studio Community 2015 (Version 14.0.25431.01 Update 3) and Intel® Compiler 17.0 Update 5 for C++ Windows was used for its compilation. Calculations were performed on the workstation which was equipped by 2 processors Intel® Xeon® E5-2687W v2 @ 3.40 GHz, each having 8 cores/16 threads, and by 64 GB of RAM memory (4 modules of Kingston 9965516-138.A 16GB DDR3-1600MHz PC3-12800).

Characteristic parameters of the simulations

- Typical size of computational grid: $(80 \times 80 \times 80)$ cells

- Typical number of charged particles: 2.0×10^6 of computational superparticles, each representing 1.0×10^3 of real physical particles

- Typical dimensions of the computational domain: $(1.0 \times 1.0 \times 1.0) \times 10^{-2}\,\mathrm{m}$
- Typical number of simulated time steps: $(1-2) \times 10^5$ time steps to reach steady state, additional $(1-2) \times 10^5$ time steps to collect stochastic samples and get averaged results
- Typical duration of 1 time step: $(1.5 - 2.0)\,\mathrm{s}$
- Typical clock time of a simulation run: $(80 - 200)$ hours

Post-processing quantities It is the main benefit of the PIC method that it provides detailed microscopic information about the modelled ensemble of the particles – positions and velocities of all charged particles. The developed code processes this information and derives macroscopic quantities which can be further used for interpretation of the modelled case or for monitoring of the running calculation. For the purpose of the post-processing, Python package of the scripts based on the Matplotlib library [Hunter, 2007] was developed.

The first group of the post-processing quantities are global monitors which are evaluated at each time step (index i denotes the particular particle species):

- Current number N_i of the particles of each species in the simulation
- Mean kinetic energy ϵ_i
$$\epsilon_i = \frac{1}{2} m_i \frac{\sum_{j=1}^{N_i} v_j^2}{N_i}$$
- Drift velocity $\boldsymbol{u}_i$
$$\boldsymbol{u}_i = \frac{\sum_{j=1}^{N_i} \boldsymbol{v}_j}{N_i}$$
- Collision frequency ν_i
$$\nu_i = \frac{N_{coll,i}}{\mathrm{d}t},$$
where N_{coll} is the number of particles which underwent collision event during the current time iteration and $\mathrm{d}t$ is the time step of the simulation
- Current density of each particle species on the probes which are present in the simulation
$$j_i = \frac{q_i}{A} \frac{N_{l,i}}{\mathrm{d}t},$$
where N_l is the number of particles which landed on the probe and A is the area of the probe surface
- Execution time of the particular parts of the code: solution of the Poisson equation, time integration of the equations of motion for each particle, resolution of the colisional events, post-processing.

The other group of the post-processing quantities are those which are evaluated in the nodes of the computational mesh; linear interpolation (Cloud-in-Cell scheme) is used to transfer the particular information from the position of a particle to the position of a mesh node (index k denotes the particular mesh node). Due to the stochastic nature of the PIC/MCC model, quantities evaluated on

the computational mesh show a considerable degree of fluctuations. To get sufficiently smooth solution, defined number of the solution samples ($\sim$ hundreds of samples) is averaged after the steady state solution is reached.

- Electric potential ϕ_k – it is directly provided by the implemented Poisson solver.
- Electric field intensity $\boldsymbol{E}_k$

$$E_{k,x} = -\frac{\phi_{k+1} - \phi_{k-1}}{2\mathrm{d}x};$$

  y and z component of the electric field are derived analogically.

- Number density $n_{i,k}$

$$n_{i,k} = \frac{\sum_{j=1}^{N_i} w_{j,k}}{\mathrm{d}x\mathrm{d}y\mathrm{d}z},$$

  where $w_{j,k}$ is the weighting factor of the linear interpolation belonging to a particle j of a species i for the mesh node k (for the nodes which belong to the mesh cell inside which the particle is present, $w_{j,k}$ reflects the distance between the particle position and the mesh node in the sense of the CIC scheme; $w_{j,k} = 0$ for the other nodes; $\sum_k^{N_n} w_{j,k} = 1$, where N_n is the total number of the mesh nodes).

- Velocity distribution $\boldsymbol{u}_{i,k}$

$$\boldsymbol{u}_{i,k} = \frac{\sum_{j=1}^{N_i} w_{j,k}\boldsymbol{v}_j}{n_{i,k}\mathrm{d}x\mathrm{d}y\mathrm{d}z},$$

  where $\boldsymbol{v}_j$ is the velocity of a particle.

- Particle flux $\boldsymbol{\Gamma}_{i,k}$

$$\boldsymbol{\Gamma}_{i,k} = n_{i,k}\boldsymbol{u}_{i,k}.$$

- Pressure tensor $\mathbb{T}_{i,k}$

$$\left(\mathbb{T}_{i,k}\right)_{rs} = m_i n_{i,k} \frac{\sum_{j=1}^{N_i} w_{j,k}(v_{j,r} - u_{i,k,r})(v_{j,s} - u_{i,k,s})}{n_{i,k}\mathrm{d}x\mathrm{d}y\mathrm{d}z},$$

  where indexes r, s denote the rs component of the pressure tensor.

- Internal energy $(\epsilon_{int})_{i,k}$

$$(\epsilon_{int})_{i,k} = \frac{1}{2}\frac{\left(\mathbb{T}_{i,k}\right)_{11} + \left(\mathbb{T}_{i,k}\right)_{22} + \left(\mathbb{T}_{i,k}\right)_{33}}{n_{i,k}}.$$

- Flow energy $(\epsilon_{flw})_{i,k}$

$$(\epsilon_{flw})_{i,k} = \frac{1}{2}m_i|\boldsymbol{u}_{i,k}|^2.$$

- Total energy $(\epsilon_{tot})_{i,k}$

$$(\epsilon_{tot})_{i,k} = (\epsilon_{int})_{i,k} + (\epsilon_{flw})_{i,k}.$$

- Diffusion coefficient $D_{i,k}$ – calculation of the diffusion coefficient is based on the expression (2.2.18) which was derived within the framework of the two-term approximation. The expression can be rewritten in the form

$$D = \frac{1}{3}\left\langle \frac{v^2}{n_g \sigma(v) v} \right\rangle, \tag{3.2.1}$$

  which can be further used for the calculation of the distribution of the diffusion coefficient on the computational mesh

$$D_{i,k} = \frac{1}{3n_g} \frac{1}{n_{i,k} \mathrm{d}x\mathrm{d}y\mathrm{d}z} \sum_{j=1}^{N_i} w_{j,k} \frac{v_j}{\sigma\left(v_j\right)}.$$

- Mobility coefficient $\mu_{i,k}$ – calculation of the mobility coefficient is based on the expression

$$\mu = \frac{|q|}{m \left\langle n_g \sigma(v) v \right\rangle}, \tag{3.2.2}$$

  which leads to the expression

$$\mu_{i,k} = \frac{|q|}{m n_g} \left(\frac{\sum_{j=1}^{N_i} w_{j,k} v_j \sigma\left(v_j\right)}{n_{i,k} \mathrm{d}x\mathrm{d}y\mathrm{d}z} \right)^{-1}.$$

- Energy distribution function $f_{i,k}(\epsilon)$ – histograms of the charged particles according to their energy are recorded in every node of the computational mesh; energy distribution function can be thus found at any point.

3.2.2 Poisson solver

Cartesian computational mesh with cubic cells was cosidered for solution of the Poisson equation. Cloud-in-Cell algorithm, which was more discussed in the chapter 2.1, was implemented for interpolation between the mesh nodes and superparticle positions.

Fast Poisson solver routines of the Intel® Math Kernel Library (MKL) [Intel Corporation, 2017] were implemented in the developed code for the solution of the Poisson equation

$$\Delta\phi = -\frac{\rho}{\epsilon_0}.$$

The MKL library involves the standard software libraries for numerical linear algebra as BLAS, BLACS, LAPACK, ScaLAPACK. For a solution of the Poisson equation, it offers a group of highly parallelized routines which are based on the discrete Fourier transform. It was shown in various works (e. g. [Gholami et al., 2016], [Garcia-Risueno et al., 2014], [Ibeid et al., 2020]) that methods for solving the Poisson equation on the uniform computational grid which are based on the fast Fourier transform are methods of choice from the point of view of the computational speed and accuracy compared to the other methods which also scale well up to very large number of unknowns (such as fast multipole method, multigrid methods or method of conjugate gradients). Fast Poisson solver methods of the Intel® MKL library were used in the 3D PIC/MCC code

because the routines of this library are highly optimized for Intel® processors and show very good performance compared to the alternative implementations (e. g. [Khokhriakov et al., 2018], [Gambron and Thorne, 2020], [Kalinkin et al., 2009]).

In the developed 3D PIC/MCC code, we took advantage of the 3D fast Poisson solver of the MKL libtrary in a Cartesian coordinate system which works on parallelepiped domain $a_x < x < b_x$, $a_y < y < b_y$, $a_z < z < b_z$. Two types of boundary conditions (BC) which MKL library provides were implemented on the outer boundaries of the computational domain in the 3D PIC/MCC code: Dirichlet BC modelling a wall with a fixed value of the electric potential and periodic BC modelling symmetrical cases. MKL library Poisson solver routines, however, do not allow to precribe Dirichlet BC on the mesh nodes which are inside the computational domain. This is needed for modelling of the metal solids immersed into the plasma in the computational domain. The MKL routines allow only charge density to be the source of the electric field in the computational domain. Modelling of the internal potentials was thus adressed by a workaround in the developed code. In the first step, electrostatic solver of the ANSYS® Maxwell Academic Student software [ANSYS, Inc., 2021] was used to calculate electrostatic solution of the modelled immersed solid object with prescribed value of the electric potential. Zero potential boundary condition was applied on the outer boundaries of the computational domain. Apart from the distribution of the electric potential, the ANSYS® Maxwell software provides also distribution of the surface charge density σ on the surface of the modelled solid object. According to the Gauss's law, the entirety of the charge of the conductor resides on its surface and can be expressed by the equation

$$\sigma = \epsilon_0 E,$$

where E is the electric field measured at an infinitesimally small distance from the surface of the conductor. Consequently, the obtained surface charge density was exported for the purpose of the 3D PIC/MCC code and converted to the volume charge density ρ by dividing by the size of a computational grid cell. Finally, this pattern of the volume charge density was superposed to the plasma space charge density in every time step of the simulation and thus, it was modelling the immersed biased solid. It should be noted that it is the normal component of the electric field E on the surface of the immersed solid which is prescribed in this way (= Neumann boundary condition for the electric potential ϕ) rather than the fixed value of the electric potential on the solid. During the run of the 3D PIC/MCC code, plasma creates sheath in the surroundings of the immersed solid and electric potential which is finally established on its surface might be different from that one which was an input for the vacuum solution in the ANSYS® Maxwell software.

The methodology of modelling of the internal potentials immersed in the computational domain is illustrated in the figure 3.1 where the calculation of electric field of a rectangular probe ($2 \times 2 \times 0.5$) mm with 1 V of electric potential is shown. Cubic computational domain of 1×10^{-2} m edge and zero potential boundary condition on its outer surface was considered for the calculation. Surface charge density calculated by the ANSYS® Maxwell software was converted to the volume charge density using three different meshes and vacuum electric field (without plasma) was evaluated by the 3D PIC/MCC code (figure 3.1b,

3.1b). It can be seen that with finer mesh, the 3D PIC/MCC code solution approaches to the original solution obtained by the ANSYS® Maxwell software. In the subsequent physical calculations presented in the chapters 4.2 and 4.4, the mesh with cell size of $\mathrm{d}x = 1.25 \times 10^{-4}$ m was used as a trade-off between the solution accuracy and the needed solution time.

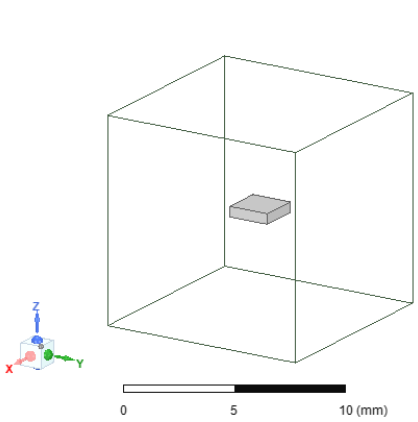

(a) Geometry of the rectangular probe and computational domain.

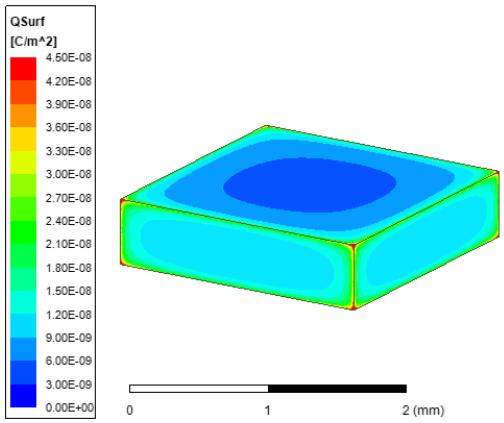

(b) Surface charge density on the rectangular probe with 1 V of electric potential calculated by ANSYS® Maxwell software.

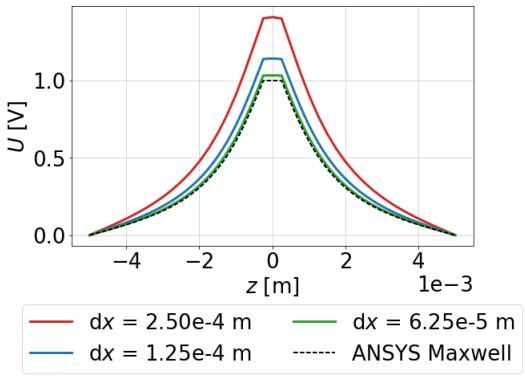

(c) Comparison of electric potential calculated by the 3D PIC/MCC code for different mesh cell sizes with original solution provided by ANSYS® Maxwell software.

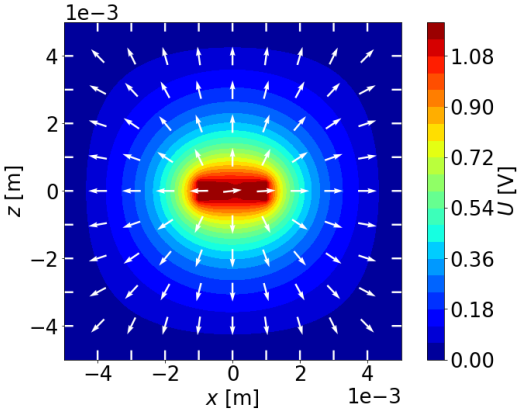

(d) Distribution of electric potential in the surroundings of the rectangular probe calculated by the 3D PIC/MCC code. Mesh cell size $\mathrm{d}x = 1.25 \times 10^{-4}$ m, white arrows represent unit vector of electric field $\boldsymbol{E}$.

Figure 3.1: Methodology of the modelling of the internal potentials in the developed 3D PIC/MCC code.

3.2.3 Particle mover

Integration of the equations of motion for the charged particles is done by explicit particle mover based on the velocity Verlet algorithm which is a good compromise between the accuracy of the solution and computational costs. The algorithm for transition from the time level t_k to the level t_{k+1} for the i-th charged particle of

the simulated ensemble can be written in the form

$$\begin{aligned}
\boldsymbol{x}_i^{k+1} &= \boldsymbol{x}_i^k + \boldsymbol{v}_i^k \Delta t + \frac{1}{2m_i} \boldsymbol{F}_i^k \Delta t^2, \\
\boldsymbol{F}_i^{k+1} &= \ldots, \\
\boldsymbol{v}_i^{k+1} &= \boldsymbol{v}_i^k + \frac{1}{2m_i} \left(\boldsymbol{F}_i^k + \boldsymbol{F}_i^{k+1} \right) \Delta t.
\end{aligned}$$

Global discretization error of the velocity Verlet algorithm is $O(\Delta t^2)$ in both position and velocity. Stability condition of the second order explicit time differencing schemes used in the PIC codes was discussed in the chapter 2.1.3. Velocity Verlet algorithm can be used only in cases when the force does not depend on the velocity of the particle since the velocity $\boldsymbol{v}_i^{k+1}$ is calculated after the evaluation of the force $\boldsymbol{F}_i^{k+1}$. In our case, the velocity Verlet algorithm can be used only for electrostatic calculations. In the developed 3D PIC/MCC code, the Verlet integration is implemented in the following way ($\boldsymbol{E}_{ext}$ denotes electric field given by external sources):

1. Calculate $\boldsymbol{a}_i^k = \frac{q_i}{m_i} \left(\boldsymbol{E}^k + \boldsymbol{E}_{ext} \right)$.
2. Calculate $\boldsymbol{v}_i^{k+1/2} = \boldsymbol{v}_i^k + \boldsymbol{a}_i^k \frac{\Delta t}{2}$.
3. Calculate $\boldsymbol{x}_i^{k+1} = \boldsymbol{x}_i^k + \boldsymbol{v}_i^{k+1/2} \Delta t$.
4. Solve Poisson equation to obtain electric field $\boldsymbol{E}^{k+1}$.
5. Calculate $\boldsymbol{a}_i^{k+1} = \frac{q_i}{m_i} \left(\boldsymbol{E}^{k+1} + \boldsymbol{E}_{ext} \right)$.
6. Calculate $\boldsymbol{v}_i^{k+1} = \boldsymbol{v}_i^{k+1/2} + \boldsymbol{a}_i^{k+1} \frac{\Delta t}{2}$.

3.2.4 Collision module

Scattering processes of charged particles with neutrals are resolved by null collision method [Skullerud, 1968], [Roucka and Hrach, 2011]. More details about the particular implementation that was used in the developed code can be found in appendix A.2. After certain time given by the collisions cross sections and particle energy, charged particle collides with neutral particle and its velocity is appropriately modified. Movement of neutral particles is not resolved by the model. In case of a collision, neutral particle is randomly generated from Maxwellian velocity distribution.

At the beginning of the simulation each particle that undergoes collisions is assigned time-to-scatter τ_i which is randomly generated from distribution

$$f(t) = \nu_{max} \exp\left(-\nu_{max} t\right). \tag{3.2.3}$$

The constant ν_{max} is unique for each charged particle species and it is determined as

$$\nu_{max} = n_g \max_{\boldsymbol{v_r}} \{ |\boldsymbol{v_r}| \sum_i \sigma_i(\boldsymbol{v_r})) \}, \tag{3.2.4}$$

where n_g is the number density of the neutrals and the maximum is considered over all possible relative velocities between charged and neutral particles

$\boldsymbol{v_r} = \boldsymbol{v_1} - \boldsymbol{v_2}$ that might occur in the simulation. The sum is taken over all collision types (described by cross sections σ_i) that the charged particle species can undergo. During the simulation each charged particle is checked whether its time-to-scatter was already reached. If yes, the concrete collision type is selected and the velocity of the particle is appropriately modified. New time-to-scatter for the charged particle is then generated.

The collision module is implemented in such a way that the collision effects are applied continuously with respect to the time axis. It means that collision events happen not only in the time steps of the main time cycle of the simulation but it might happen also in between the two following time steps. This approach is beneficial especially for modelling of medium and high pressure plasma where time-to-scatter is quite low. Particle mover (which updates particle positions and velocities) is applied only in the time steps of the main time cycle.

Cross sections of charged species collision types are energy dependent in general. To be able to use the expression 3.2.3 for generation of time-to-scatter we introduced new collision type called *null collision* which cross section is

$$\sigma_0(\boldsymbol{v}) = \frac{\nu_{max}}{n_g|\boldsymbol{v}|} - \sum_i \sigma_i(\boldsymbol{v}).$$

Null collision does not have any effect on the charged particle velocity when selected.

When it is decided that the charged particle undergoes a collision, modification of its velocity then happens in the way described further (for more detailed description of the following steps, we refer to appendix A.3). Let us denote 2 particles that collide: incident particle no. 1 with mass m_1 and velocity $\boldsymbol{v_1}$ and target particle no. 2 with mass m_2 and velocity $\boldsymbol{v_2}$. It is assumed that the collision is in general inelastic, no external forces act on the particles and there is also zero mutual force between the particles. The particles are treated as mass points. Particle velocities $\boldsymbol{v_1'}$, $\boldsymbol{v_2'}$ after the collision are to be determined.

1. step: Determine the following quantities

Relative velocity	$\boldsymbol{v_r} = \boldsymbol{v_1} - \boldsymbol{v_2}$, $v_r = \lvert\boldsymbol{v_r}\rvert$
Reduced mass	$\mu_r = \frac{m_1 m_2}{m_1+m_2}$
Velocity of centre-of-mass	$\boldsymbol{v_{CM}} = \frac{m_1\boldsymbol{v_1}+m_2\boldsymbol{v_2}}{m_1+m_2}$
Relative kinetic energy	$\epsilon_r = \frac{1}{2}\mu_r v_r^2$

2. step: Determine cross section $\sigma_i(\boldsymbol{v}_r)$ and collision frequency $\nu_i = n_g v_r \sigma_i(\boldsymbol{v}_r)$ for each collision type applicable for given incident and target particle (including null collision). Then, select one collision type with probability proportional to the particular collision frequencies. If null collision is selected, step no. 7 is applied directly.

3. step: Determine magnitude v_r' of the relative velocity vector $\boldsymbol{v_r'} = \boldsymbol{v_1'} - \boldsymbol{v_2'}$ after the collision.

- Elastic collision

$$v_r' = v_r.$$

- Excitation

$$v_r' = \left(v_r^2 - \frac{2\epsilon_{exc}}{\mu_r}\right)^{\frac{1}{2}},$$

where ϵ_{exc} is excitation energy.

- Ionization

$$v'_r = \left(v_r^2 - \frac{2\Delta E}{\mu_r} \right)^{\frac{1}{2}},$$
$$\Delta E = \epsilon_{ion} + \epsilon_{ej},$$

where ϵ_{ion} is ionization energy and ϵ_{ej} is energy taken by ejected electron. Energy ϵ_{ej} can be determined in several ways.

  - Generally, energy ϵ_{ej} has distribution described by differential ionization cross section $\frac{\mathrm{d}\sigma_{ion}}{\mathrm{d}\epsilon}(\epsilon_r, \epsilon)$. Energy ϵ_{ej} can then be determined

$$r_{ion} = \frac{\int_0^{\epsilon_{ej}} \frac{\mathrm{d}\sigma_{ion}}{\mathrm{d}\epsilon}(\epsilon_r, \epsilon)\mathrm{d}\epsilon}{\sigma_{ion}(\epsilon_r)},$$

    where $r_{ion} \in [0, 1]$ is random number generated from uniform distribution and $\sigma_{ion}(\epsilon_r)$ is integral ionization cross section; $\sigma_{ion}(\epsilon_r) = \int_0^{\epsilon_{ej,max}} \frac{\mathrm{d}\sigma_{ion}}{\mathrm{d}\epsilon}(\epsilon_r, \epsilon)\mathrm{d}\epsilon$, where $\epsilon_{ej,max} = \epsilon_r - \epsilon_{ion}$.
  - As a special case, differential ionization cross section can be independent of the energy ϵ of the ejected electron, $\frac{\mathrm{d}\sigma_{ion}}{\mathrm{d}\epsilon}(\epsilon_r, \epsilon) = \frac{\mathrm{d}\sigma_{ion}}{\mathrm{d}\epsilon}(\epsilon_r)$, and the resultant kinetic energy is then divided among scattered and ejected electrons according to random uniform distribution

$$\epsilon_{ej} = r_{ion} \left(\frac{1}{2} \mu_r v_r^2 - \epsilon_{ion} \right), \tag{3.2.5}$$

    where $r_{ion} \in [0, 1]$ is random number generated from uniform distribution.

4. step: Determine direction of the relative velocity vector $\boldsymbol{v}'_{\boldsymbol{r}}$ after the collision $\rightarrow$ determine polar and azimuthal scattering angles χ and η.

- Polar angle $\chi \in [0, \pi]$

  - Anisotropic scattering: distribution of deflection polar angle χ is given by differential cross section $\sigma_d(\epsilon_r, \chi)$ and angle χ can be determined according to

$$r_\chi = \frac{\int_0^\chi \sigma_d(\epsilon_r, \chi') \sin\chi' \mathrm{d}\chi'}{\int_0^\pi \sigma_d(\epsilon_r, \chi') \sin\chi' \mathrm{d}\chi'}, \tag{3.2.6}$$

    where $r_\chi \in [0, 1]$ is random variable generated from the uniform distribution.
  - Isotropic scattering: in this case, $\sigma_d(\epsilon_r, \chi) = \sigma_d(\epsilon_r)$ and expression 3.2.6 is simplified to

$$\cos\chi = 1 - 2r_\chi.$$

- Azimuthal angle $\eta \in [0, 2\pi]$

$$\eta = 2\pi r_\eta,$$

where $r_\eta \in [0, 1]$ is random variable generated from the uniform distribution.

5. step: Transformation of the relative velocity vector $\boldsymbol{v}_r'$

$$\boldsymbol{v}_r' = \left(v'_{r,\widehat{x}}, v'_{r,\widehat{y}}, v'_{r,\widehat{z}}\right) = (v'_r \cos\eta \sin\chi, v'_r \sin\eta \sin\chi, v'_r \cos\chi)$$

from the local coordinate system $(\widehat{x}, \widehat{y}, \widehat{z})$ to the laboratory one (x, y, z) – see more in the figure 3.2 and appendix A.4

$$\begin{pmatrix} v'_{r,x} \\ v'_{r,y} \\ v'_{r,z} \end{pmatrix} = \begin{pmatrix} \cos\phi & -\sin\phi\cos\theta & \sin\phi\sin\theta \\ \sin\phi & \cos\phi\cos\theta & -\cos\phi\sin\theta \\ 0 & \sin\theta & \cos\theta \end{pmatrix} \begin{pmatrix} \cos\eta\sin\chi \\ \sin\eta\sin\chi \\ \cos\chi \end{pmatrix} v'_r,$$

where

$$\sin\theta = \frac{\sqrt{v_{r,x}^2 + v_{r,y}^2}}{v_r}, \qquad \cos\theta = \frac{v_{r,z}}{v_r},$$

$$\sin\phi = \frac{v_{r,x}}{\sqrt{v_{r,x}^2 + v_{r,y}^2}}, \qquad \cos\phi = -\frac{v_{r,y}}{\sqrt{v_{r,x}^2 + v_{r,y}^2}}.$$

6. step: Determine velocity $\boldsymbol{v}_1'$ of the incident particle after the collision

$$\boldsymbol{v}_1' = \boldsymbol{v}_{CM} + \frac{m_2}{m_1 + m_2}\boldsymbol{v}_r'.$$

7. step: New time-to-scatter τ_i for the charged particle is generated from the random distribution

$$f(t) = \nu_{max} \exp\left(-\nu_{max} t\right).$$

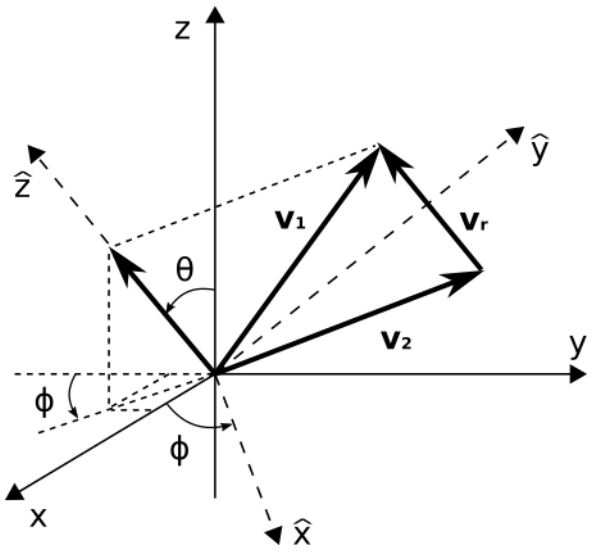

Figure 3.2: Transformation from the local coordinate system $(\widehat{x}, \widehat{y}, \widehat{z})$ to the laboratory one (x, y, z).

3.2.5 Code tests

Stability tests

At first, we bring stability test of the explicit time differencing scheme. Collisionless bulk argon plasma composed of Ar^+ ions and electrons was modelled;

input parameters of the PIC simulation are listed in the table 3.1. The simulation was done in a cubic computational domain of $1.0\,\mathrm{mm}^3$ volume. Number of real particles within one computational superparticle was set to $N_p = 1$ which led to $N_s = 2.0 \times 10^6$ of the computational superparticles for which the equations of motion were solved. The product $\omega_p \Delta t$ ranges from $\omega_p \Delta t = 1.78 \times 10^{-2}\,\mathrm{rad}$ (which is well bellow the needed 0.1 rad limit discussed in the chapter 2.1.3) for the smallest time step $\Delta t = 1.0 \times 10^{-11}\,\mathrm{s}$ up to $\omega_p \Delta t = 1.78\,\mathrm{rad}$ for the largest considered time step. Size of the computational mesh cell Δx was such that the condition controlling the finite grid instability $\Delta x / \lambda_D = 1.70 \times 10^{-2} < \pi$ was satisfied. Time evolution of the mean energy of the electrons was monitored for different time steps of the simulation and it is depicted in the figure 3.3. It can be seen that the increase of the electron mean energy during the simulation is lower with decreasing time step. This result is in agreement with theory – energy of the moving particles is well preserved if the condition $\omega_p \Delta t < 0.1\,\mathrm{rad}$ is satisfied. It can be seen that for the three smallest selected time steps of the simulation the increase of the electron mean energy is well below 0.1 % increase from the initial energy.

Temperature	$T_e = 11\,600\,\mathrm{K}$ $(= 1\,\mathrm{eV})$, $T_i = 300\,\mathrm{K}$
Number density	$n_e = n_i = 10^{15}\,\mathrm{m}^{-3}$
Plasma frequency	$\omega_p = 1.78 \times 10^9\,\mathrm{rad} \cdot \mathrm{s}^{-1}$
Debye length	$\lambda_D = 2.35 \times 10^{-4}\,\mathrm{m}$
Size of a grid cell	$\Delta x = 4.0 \times 10^{-5}\,\mathrm{m}$
Time step	$\Delta t = \{1.0 \times 10^{-11}, 5.0 \times 10^{-11}, 1.0 \times 10^{-10}, 5.0 \times 10^{-10}, 1.0 \times 10^{-9}\}\,\mathrm{s}$

Table 3.1: Input parameters of the simulations for stability tests of the explicit time differencing scheme used in the developed 3D PIC/MCC code. Plasma parameters are typical e. g. for positive column of low-temperature glow discharge plasma.

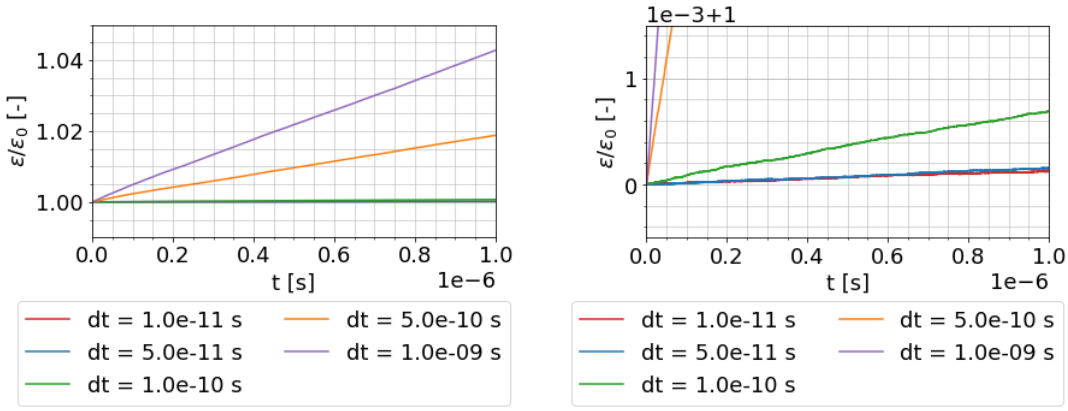

Figure 3.3: Time evolution of the mean energy ϵ of the electrons for various time steps of the PIC simulation (ϵ_0 – initial mean energy of the electrons). Number of real physical particles per one computational superparticle $N_p = 1$.

In the next step, finite grid instability of the developed 3D PIC/MCC code was tested. The test was done also for collisionless argon plasma of the parameters

which are listed in the table 3.2. Temperature 300 K was considered for electrons. Such low value is not typical for low-temperature plasma; however, it was used in order to obtain sufficiently low Debye length for the subsequent parametric study. The ratio $\Delta x/\lambda_D$ ranged from $\Delta x/\lambda_D = 0.53$ (which is well below the needed limit $\Delta x/\lambda_D = \pi$ discussed in the chapter 2.1.3) for the smallest grid cell size considered in the table 3.2 up to $\Delta x/\lambda_D = 5.29$ for the largest size of the grid cell. Apart from the three cases considered in the table 3.2, plasma with electrons of 3 000 K temperature was investigated with grid cell size $\Delta x = 2.0 \times 10^{-5}$ m to obtain even lower ratio $\Delta x/\lambda_D = 0.17$. Similarly, plasma of number density $n = 2.0 \times 10^{15}\,\mathrm{m}^{-3}$ with grid cell size $\Delta x = 2.0 \times 10^{-4}$ m leading to high ratio $\Delta x/\lambda_D = 7.48$ was also investigated. All of the cases are depicted in the figure 3.3 in terms of mean electron energy time evolution. It can be clearly seen that the non-physical increase of electron energy is lower for lower grid cell size which is well in agreement with theory. The three investigated cases which satisfy condition $\Delta x/\lambda_D < \pi$ preserve electron energy up to 2.5 % in the considered time interval.

Temperature	$T_e = 300\,\mathrm{K}$, $T_i = 300\,\mathrm{K}$
Number density	$n_e = n_i = 10^{15}\,\mathrm{m}^{-3}$
Plasma frequency	$\omega_p = 1.78 \times 10^{9}\,\mathrm{rad \cdot s}^{-1}$
Debye length	$\lambda_D = 3.78 \times 10^{-5}\,\mathrm{m}$
Size of a grid cell	$\Delta x = \{2.0 \times 10^{-5}, 4.0 \times 10^{-5}, 2.0 \times 10^{-4}\}$ m
Time step	$\Delta t = 1.0 \times 10^{-11}\,\mathrm{s}$

Table 3.2: Input parameters of the simulations for tests of the finite grid instability of the developed 3D PIC/MCC code. Plasma parameters correspond to rather hypothetical plasma which was used only for the stability tests of the developed particle code.

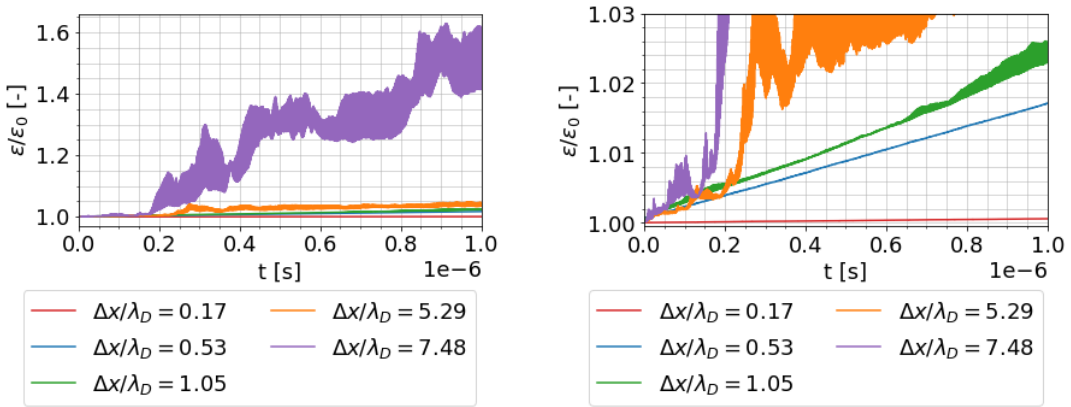

Figure 3.4: Time evolution of the mean energy ϵ of the electrons for various ratios of the computational grid cell size Δx to the Debye length λ_D (ϵ_0 – initial mean energy of the electrons). Number of real physical particles per one computational superparticle $N_p = 1$.

Reid's benchmark

In the article Reid [1979], a couple of tests that are suitable for validation collision modules implemented in PIC codes were proposed. The tests consist in determination of transport properties of electron swarms in model gases with various combinations of elastic and inelastic cross sections, in some cases with anisotropic scattering distribution. The authors compare two methods of determination electron energy distribution functions and transport coefficients: Monte Carlo simulations and analytical solution of the Boltzmann equation in the two-term approximation. Below, results obtained by the developed collision module for the 3D PIC/MCC model are compared with the original Reid results in terms of drift velocity v_{dr} of the electron swarm and mean energy $\langle\epsilon\rangle$ of the electrons. First, simple isotropic scattering models are proposed; further, hydrogen-like model to examine the effect of anisotropic elastic and inelastic scattering is proposed.

In the original Reid's work [Reid, 1979], it is assumed that the electron which is ejected during the ionization process takes zero energy. In the developed 3D PIC/MCC code, it is assumed (by default) that the resultant kinetic energy after the ionization is divided among the incident and ejected electrons according to random uniform distribution (equation 3.2.5). For the purpose of comparison with the original Reid's results, the code was temporarily changed and zero energy of the ejected electron was assumed.

Typical values of the 3D PIC/MCC simulation parameters were the following: number of the monitored electrons $N_e = 3.0 \times 10^6$, time step of the simulation $\mathrm{d}t = 5.0 \times 10^{-13}\,\mathrm{s}$, number of the iterations $N_{iter} = 5.0 \times 10^5$, maximal kinetic energy for determination of ν_{max} (equation 3.2.4) in the null collision method $E_{max} = 4\,\mathrm{eV}$ (up to 30 eV in some cases), discretization of the energy axis in the definition of collision cross sections $\mathrm{d}E = 0.1\,\mathrm{eV}$.

Isotropic scattering models

Constant cross sections The first model used elastic cross section which was everywhere independent of energy and inelastic ionization cross section which increased discontinuously to a constant value at the treshold energy. Model parameters are listed in the table 3.3. Simulations were carried out for multiple values Q of the inelastic cross section σ_i and at the two values of the reduced electric field $E/N = \{1.0, 24\}$ Td. Comparison of the 3D PIC/MCC code results with the original Reid's results is presented in the figures 3.5 and 3.6.

Very good agreement between the results of the 3D PIC/MCC code and the original Reid's results is observed in the case of $E/N = 1\,\mathrm{Td}$ for all values of σ_i. In the case $E/N = 24\,\mathrm{Td}$, significant differences between the particle models and Boltzmann analysis are observed for larger values of σ_i ($\sigma_i > 0.5\sigma_e$), especially for the values of the drift velocity v_dr. However, the 3D PIC/MCC model results are still well in agreement with the Reid's results obtained by Monte Carlo solution. The discrepancies between the particle models and Boltzmann analysis originate from the errors introduced by the two-term approximation used in the Boltzmann analysis solution as it was explained and verified in the original Reid's work.

Molecular weight	$M = 4.0\,\text{a.m.u.}$
Gas temperature	$T = 0\,\text{K}$
Gas number density	$N = 10^{23}\,\text{m}^{-3}$
Reduced electric field	$E/N = \{1.0, 24\}$ Td
Elastic cross section	$\sigma_e = \sigma_{m,e} = 6.0 \times 10^{-20}\,\text{m}^2$
Inelastic treshold	$\epsilon_i = 0.2\,\text{eV}$
Inelastic cross section	$\sigma_i(\epsilon) = 0$ for $\epsilon < \epsilon_i$
	$\sigma_i(\epsilon) = Q$ for $\epsilon \geq \epsilon_i$
	$Q = (0 - 6) \times 10^{-20}\,\text{m}^2$ for $E/N = 1\,\text{Td}$
	$Q = (0 - 10) \times 10^{-20}\,\text{m}^2$ for $E/N = 24\,\text{Td}$

Table 3.3: Parameters of the isotropic scattering models with constant cross sections.

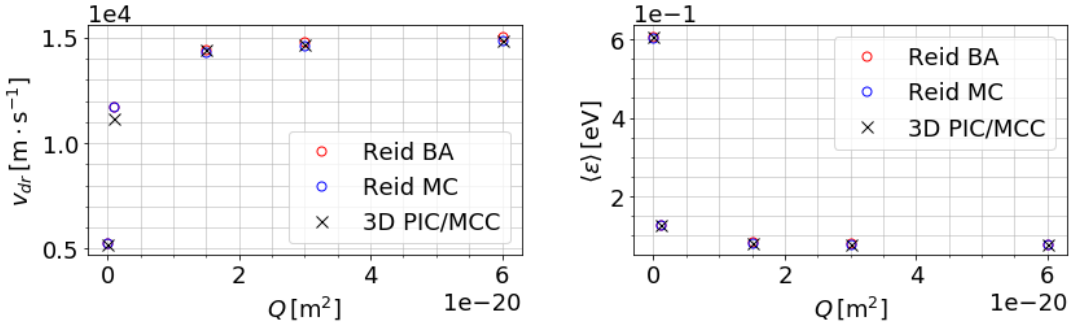

Figure 3.5: Comparison of the original Reid's results [Reid, 1979] (BA – Boltzmann analysis, MC – Monte Carlo solution) with the results of the developed 3D PIC/MCC code. Isotropic scattering model with constant cross section of both elastic and inelastic collisions, $E/N = 1\,\text{Td}$.

'Ramp' inelastic cross sections More realistic model of the inelastic cross section was used in the next step. The model had the same properties as that one used in the previous paragraph (table 3.3) except that the inelastic cross section was a linear function of energy beyond the treshold energy. The calculations were done for multiple values of the slope k of the inelastic cross section and at the two values of the reduced electric field $E/N = \{1.0, 24\}$ Td (table 3.4). Further, the simulations were also carried out for multiple values of E/N while keeping $k = 10^{-19}\,\text{m}^2\,\text{eV}^{-1}$. Results of the performed study are presented in the figures 3.7, 3.8 and 3.9.

Inelastic cross section	$\sigma_i(\epsilon) = 0$ for $\epsilon < \epsilon_i$
	$\sigma_i(\epsilon) = k\,(\epsilon - \epsilon_i)$ for $\epsilon \geq \epsilon_i$
	$k = (3 - 50) \times 10^{-20}\,\text{m}^2\,\text{eV}^{-1}$ for $E/N = 1\,\text{Td}$
	$k = (1 - 10) \times 10^{-20}\,\text{m}^2\,\text{eV}^{-1}$ for $E/N = 24\,\text{Td}$
	$E/N = (1 - 40)$ Td for $k = 10^{-19}\,\text{m}^2\,\text{eV}^{-1}$

Table 3.4: Parameters of the isotropic scattering models with 'ramp' cross sections.

It can be stated that similar trends as in the constant cross section case can be observed – difference between the Boltzmann analysis results and particle model

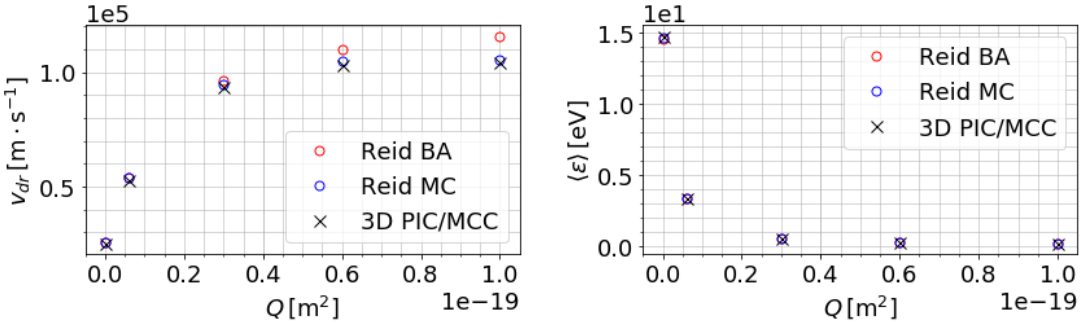

Figure 3.6: Comparison of the original Reid's results [Reid, 1979] (BA – Boltzmann analysis, MC – Monte Carlo solution) with the results of the developed 3D PIC/MCC code. Isotropic scattering model with constant cross section of both elastic and inelastic collisions, $E/N = 24$ Td.

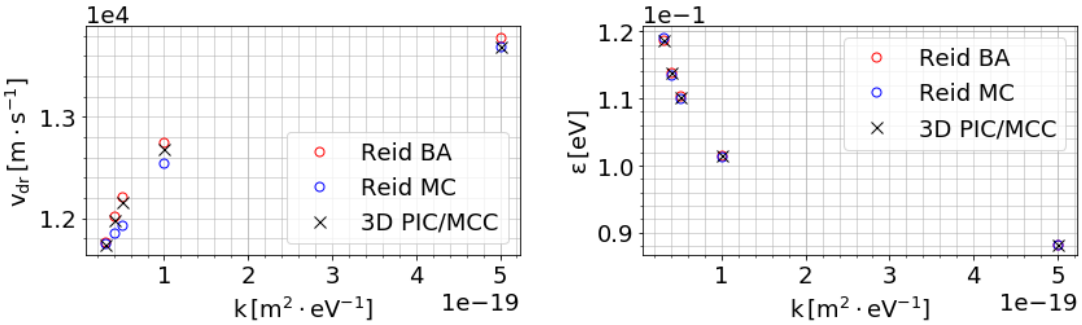

Figure 3.7: Comparison of the original Reid's results [Reid, 1979] (BA – Boltzmann analysis, MC – Monte Carlo solution) with the results of the developed 3D PIC/MCC code. Isotropic scattering model with constant cross section of the elastic collisions and 'ramp' cross section of the inelastic collisions, $E/N = 1$ Td.

results are larger for higher ratio σ_i to σ_e as can be clearly seen for the case $E/N = 24$ Td. It is a consequence of the errors introduced by the two-term approximation in the Boltzmann analysis solution. In the case $E/N = 1$ Td, it can be seen that the 3D PIC/MCC model results are closer to the Boltzmann analysis results than to the Reid's Monte Carlo solution. Both particle models differ in the implementation of the collision module which might be the reason of the observed differences. However, at the low values of σ_i/σ_e ratio, Boltzmann analysis should provide satisfactorily precise results and therefore, the 3D PIC/MCC model results can be also regarded as sufficiently precise in this region. The results in the figure 3.9 show increasing difference between the particle models results and the results of the Boltmann analysis with increasing electric field E/N – it is due to the increasing ratio of σ_i to σ_e which is a consequence of the linear energy dependence of the inelastic cross section.

Anisotropic scattering models In this section, we consider that total scattering is anisotropic. The anisotropy is described by function $I(\chi), \chi \in [0, \pi]$ and differential cross section is assumed in the form

$$\sigma_d(\epsilon_r, \chi) = \frac{1}{2\pi}\sigma(\epsilon_r)\mathcal{I}(\chi),$$

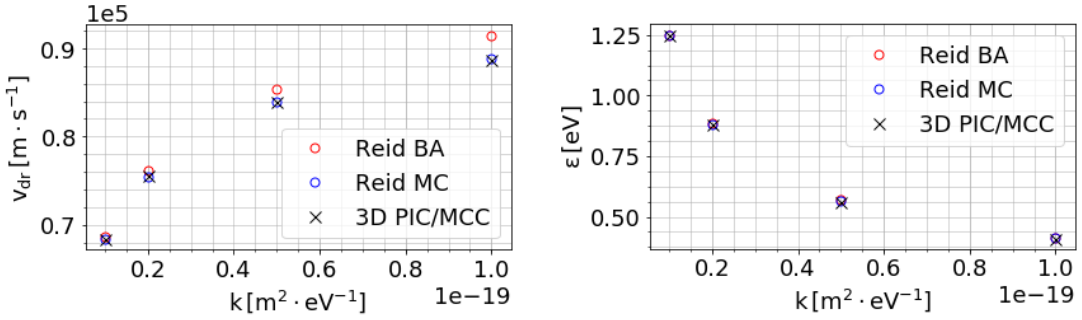

Figure 3.8: Comparison of the original Reid's results [Reid, 1979] (BA – Boltzmann analysis, MC – Monte Carlo solution) with the results of the developed 3D PIC/MCC code. Isotropic scattering model with constant cross section of the elastic collisions and 'ramp' cross section of the inelastic collisions, $E/N = 24$ Td.

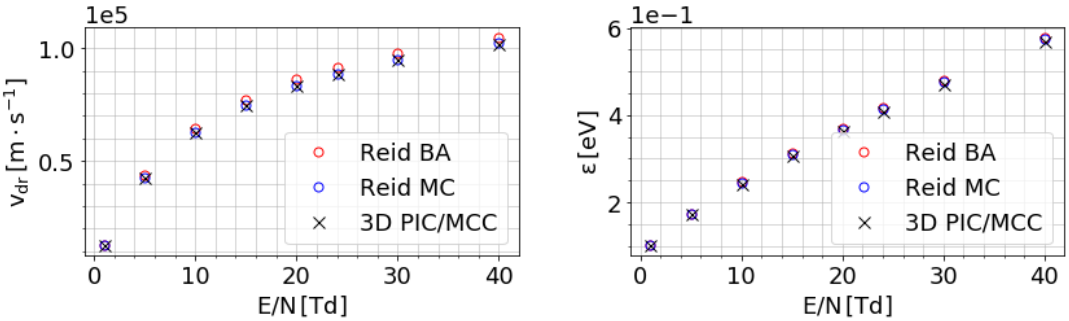

Figure 3.9: Comparison of the original Reid's results [Reid, 1979] (BA – Boltzmann analysis, MC – Monte Carlo solution) with the results of the developed 3D PIC/MCC code. Isotropic scattering model with constant cross section of the elastic collisions and 'ramp' cross section of the inelastic collisions, $k = 10^{-19}\,\mathrm{m}^2\,\mathrm{eV}^{-1}$.

where

$$\mathcal{I}(\chi) = \frac{I(\chi)}{\int_0^\pi I(\chi)\sin\chi \mathrm{d}\chi}.$$

If the assumed form of the differential cross section is inserted into the general expression 3.2.6, we get the following expression which relates random variable $r_\chi \in [0,1]$ and polar angle χ which is to be selected by the Monte Carlo method

$$r_\chi = \int_0^\chi \mathcal{I}(\chi')\sin\chi' \mathrm{d}\chi'.$$

The study was done for four generally anisotropic models – two models were symmetric about $\chi = \pi/2$, the other two were asymmetric. For each of the models, we also present the resultant expression for calculation of the polar angle χ.

1. Symmetric scattering

   (a) Isotropic scattering (model A)

$$I(\chi) = 1,$$
$$\cos\chi = 1 - 2r_\chi.$$

(b) Pronounced forward and back scattering (model B)

$$I(\chi) = \cos^4 \chi,$$
$$\cos \chi = (1 - 2r_\chi)^{\frac{1}{5}}.$$

2. Asymmetric scattering

(a) Predominantly back scattering (model C)

$$I(\chi) = \exp\left[-1.5\left(\cos\chi + 1\right)\right],$$
$$\cos\chi = -\frac{2}{3}\ln\{r_\chi\left[1 - \exp\left(-3\right)\right] + \exp\left(-3\right)\} - 1.$$

(b) Predominantly back and forward scattering (model D)

$$\begin{aligned} I(\theta) &= 1 \text{ for } 0 < \theta < 0.134\pi \\ &= 0 \text{ for } 0.134\pi \leq \theta < 3\pi/4 \\ &= 1 \text{ for } 3\pi/4 \leq \theta \end{aligned}$$

Let us define $C = 2 + \cos\frac{3\pi}{4} - \cos\left(0.134\pi\right)$. Polar angle χ is then given in the following way:

$$r_\chi < \frac{1}{C}\left[1 - \cos\left(0.134\pi\right)\right] \Rightarrow \cos\chi = 1 - r_\chi C,$$
$$r_\chi \geq \frac{1}{C}\left[1 - \cos\left(0.134\pi\right)\right] \Rightarrow \cos\chi = 1 - r_\chi C + \cos\frac{3\pi}{4} - \cos\left(0.134\pi\right).$$

The computational study of anisotropic scattering models was done for hydrogen-like model at the reduced field $E/N = 25$ Td. Constant elastic cross section and linearly ramped inelastic cross setion with energy treshold 0.516 eV, which corresponds to the vibrational excitation cross section, were considered in the calculations. All of the simulation parameters are summarized in the table 3.5. Investigation of the asymmetric anisotropic scattering was done for two distributions with the same ratio of $\sigma_{m,e}$ to σ_e ($\sigma_{m,e} = 1.438\sigma_e$). In order to keep the transport properties approximately the same as those for symmetric scattering models, the total elastic scattering cross section was reduced to $6.954 \times 10^{-20}\,\mathrm{m}^2$; thus, maintaining $\sigma_{m,e} = 10.0 \times 10^{-20}\,\mathrm{m}^2$. Results of the anisotropic scattering study are presented in the figure 3.10.

Molecular weight	$M = 2.0$ a.m.u.
Gas temperature	$T = 0\,\mathrm{K}$
Gas number density	$N = 10^{23}\,\mathrm{m}^{-3}$
Drift field	$E = 2.5 \times 10^3\,\mathrm{Vm}^{-1}$
Elastic momentum transfer cross section	$\sigma_{m,e} = 10.0 \times 10^{-20}\,\mathrm{m}^2$
Inelastic treshold	$\epsilon_i = 0.516\,\mathrm{eV}$
Inelastic cross section	$\sigma_i(\epsilon) = 0$ for $\epsilon < \epsilon_i$
	$\sigma_i(\epsilon) = 0.4\,(\epsilon - \epsilon_i)$ for $\epsilon \geq \epsilon_i$

Table 3.5: Parameters of the anisotropic scattering models.

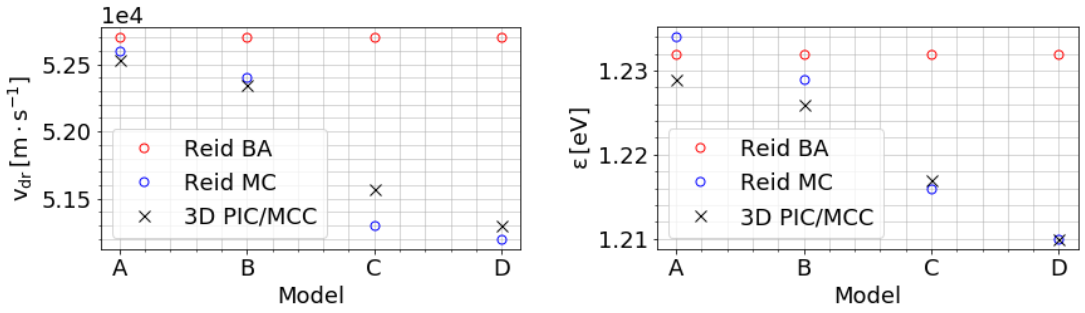

Figure 3.10: Comparison of the original Reid's results [Reid, 1979] (BA – Boltzmann analysis, MC – Monte Carlo solution) with the results of the developed 3D PIC/MCC code. Comparison of different anisotropic scattering models.

The results obtained by the developed 3D PIC/MCC code show the same trends as the original Reid's results of the Monte Carlo analysis – it means very good agreement with the Botzmann analysis results for the symmetric scattering models A and B, while differences in the v_{dr} and ϵ values of the order $2-3\%$ in the case of the asymmetrical models C and D. It is caused by the approximation used in the Boltzmann analysis which assumes that the momentum transfer cross section of the inelastic collision is equal to the total cross section and which is valid only for the models A and B.

Conclusion of the 3D PIC/MCC code tests according to the Reid's benchmark The vast majority of the results obtained by the developed 3D PIC/MCC code shows very good agreement (differences up to $\sim 3\%$) with the original Reid's results obtained by the Monte Carlo analysis and similar trends with respect to the original Reid's results based on the Boltzmann analysis.

3.3 3D fluid code

Finite element method was employed for the solution of the partial differential equations originating from the fluid description of plasma. The FEniCS project [Alnæs et al., 2015] was used for the numerical solution of the fluid plasma models. The FEniCS project allows to turn the weak formulation of the respective set of equations into the numerical scheme by means of Python scripting interface.

Weak formulation of the drift-diffusion approximation Let us consider plasma containing multiple charged particle species. The minimal self-consistent steady-state model based on the drift-diffusion approximation is the following set of continuity and momentum conservation equations for the unknown density n_j and potential ϕ distribution functions:

$$\begin{aligned} \nabla \cdot \boldsymbol{\Gamma}_j &= 0, \\ \boldsymbol{\Gamma}_j &= -\mathrm{sgn}\,(q_j)\,\mu_j n_j \nabla\phi - D_j \nabla n_j, \\ \Delta\phi &= -\frac{1}{\epsilon_0}\sum_j q_j n_j, \end{aligned} \tag{3.3.1}$$

where the index j denotes the respective particle species.

Let us first derive the weak formulation of the Poisson equation. The equation is supplemented by Dirichlet and Neumann boundary conditions for the potential ϕ:

$$\begin{aligned} \phi &= \phi_D^i && \text{on } \partial\Omega_D^i, \quad i = 0, 1, ... \\ \boldsymbol{n} \cdot \nabla\phi &= 0 && \text{on } \partial\Omega_N^i, \quad i = 0, 1, ... \end{aligned}$$

At first, the equation is multiplied by test function v and integration over the computational domain Ω by parts is then performed.

$$\int_\Omega \Delta\phi v \mathrm{d}x = -\frac{1}{\epsilon_0} \int_\Omega \sum_j q_j n_j v \mathrm{d}x,$$

$$\int_\Omega \nabla\phi \cdot \nabla v \mathrm{d}x - \int_{\partial\Omega} \boldsymbol{n} \cdot \nabla\phi v \mathrm{d}s = \frac{1}{\epsilon_0} \int_\Omega \sum_j q_j n_j v \mathrm{d}x.$$

The boundary integral vanishes on the Dirichlet part of the boundary since $v = 0$ here. It also vanishes on the Neumann part of the boundary since homogeneous Neumann boundary condition is considered there. Finally, we get the following variational problem

$$F(\phi, v) = \int_\Omega \nabla\phi \cdot \nabla v \mathrm{d}x - \frac{1}{\epsilon_0} \int_\Omega \sum_j q_j n_j v \mathrm{d}x = 0.$$

Similarly, weak formulation of the continuity equation, which can be regarded as the equation for the unknown density function n_j, is derived. The continuity equation is supplied by the following Dirichlet and Neumann boundary conditions:

$$\begin{aligned} n_j &= n_{j,D}^i && \text{on } \partial\Omega_D^i, \quad i = 0, 1, ... \\ \boldsymbol{n} \cdot \boldsymbol{\Gamma}_j &= 0 && \text{on } \partial\Omega_N^i, \quad i = 0, 1, ... \end{aligned}$$

If the homogeneous Neumann boundary conditions are applied in the model, they are used at the outer boundaries of the computational domain and represent planes of symmetry to which the particle flux is tangential. In this case, homogenous Neumann boundary condition is applied also for potential on this part of the boundary. Neumann parts of the boundaries are the same ones for Poisson and also continuity equation. In this view, we can consider

$$\boldsymbol{n} \cdot \nabla n_j = 0 \qquad \text{on } \partial\Omega_N^i, \quad i = 0, 1, ...$$

Weak formulation of the continuity equation is obtained by its multiplication by test function v_j and integration by parts over the whole computational domain:

$$\int_\Omega \nabla \cdot \boldsymbol{\Gamma}_j v_j \mathrm{d}x = 0,$$

$$\int_\Omega \boldsymbol{\Gamma}_j \cdot \nabla v_j \mathrm{d}x - \int_{\partial\Omega} \boldsymbol{n} \cdot \boldsymbol{\Gamma}_j v_j \mathrm{d}s = 0,$$

$$\int_\Omega \left[\mathrm{sgn}(q_j)\mu_j n_j \nabla\phi + D_j \nabla n_j\right] \cdot \nabla v_j \mathrm{d}x -$$

$$- \int_{\partial\Omega} \left[\mathrm{sgn}(q_j)\mu_j n_j \boldsymbol{n} \cdot \nabla\phi + D_j \boldsymbol{n} \cdot \nabla n_j\right] v_j \mathrm{d}s = 0.$$

The boundary integral vanishes on the Dirichlet part of the boundary since $v_j = 0$ here. It also vanishes on the Neumann part of the boundary since homogeneous Neumann boundary condition for density and potential is considered there. As a result, we get the following variational problem:

$$F_j(n_j, v_j) = \int_\Omega [\mathrm{sgn}(q_j)\mu_j n_j \nabla\phi + D_j \nabla n_j] \cdot \nabla v_j \mathrm{d}x = 0. \tag{3.3.2}$$

Weak formulations of the Poisson and continuity equations create a nonlinear coupled system of equations which can be implemented within the FEniCS project as a coupled nonlinear variational problem in the form

$$F + \sum_j F_j = 0. \tag{3.3.3}$$

4. Physical results

4.1 1D models of plasma sheath

This chapter brings results of a computational study of plasma sheaths created in front of an infinitely large planar probe. Geometry configuration of the investigated problem is depicted in the Figure 4.1. The nature of the problem is one dimensional; however, 3D PIC/MCC model with periodic boundary conditions applied in Y, Z directions was used for its solution. Charged particles were injected to the computational domain from the source of particles with Maxwellian velocity distribution. The results of the particle model are compared to the particular 1D fluid models and differences between these two modelling approaches are discussed. The object of the study is electropositive argon plasma consisting of electrons e^- and simple argon ions Ar^+; plasma parameters and settings of the model are listed in the Table 4.1. Number of physical particles per one computational superparticle was set to $N_p = 1$. Both collisionless and collisional plasma was investigated.

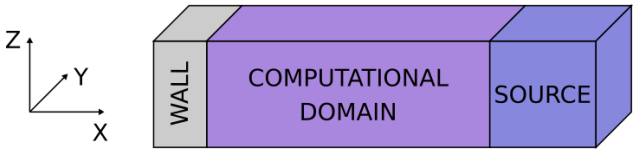

Figure 4.1: Geometry of 1D plasma sheath model.

Temperature	$T_e = 11\,600\,\mathrm{K}$ $(= 1\,\mathrm{eV})$, $T_i = 300\,\mathrm{K}$
Number density	$n_e = n_i = 10^{15}\,\mathrm{m}^{-3}$
Plasma frequency	$\omega_p = 1.78 \times 10^9\,\mathrm{rad \cdot s}^{-1}$
Debye length	$\lambda_D = 2.35 \times 10^{-4}\,\mathrm{m}$
Size of a grid cell	$\Delta x = 4.0 \times 10^{-5}\,\mathrm{m}$
Time step	$\Delta t = 1.0 \times 10^{-11}\,\mathrm{s}$
Computational domain	$(10 \times 0.4 \times 0.4) \times 10^{-3}\,\mathrm{m}$

Table 4.1: Plasma parameters and settings of the 3D PIC/MCC model used for the study of 1D plasma sheaths.

4.1.1 Collisionless plasma

The calculation of collisionless plasma sheath was performed mainly to validate that the developed 3D PIC/MCC code is able to reproduce the results predicted by the theory which was presented in the chapter 1.1.1. Only the sheath region was covered by the simulation – this was achieved by the fact that the positive argon ions entered the computational domain already at Bohm velocity ($u_B = \sqrt{k_B T_e / m_i} = 1.55 \times 10^3 \mathrm{m \cdot s}^{-1}$ in the considered case) directed towards the planar probe. In reality, pre-sheath with potential drop $\phi_p = k_B T_e / 2\mathrm{e}$ would be created in front of the sheath region.

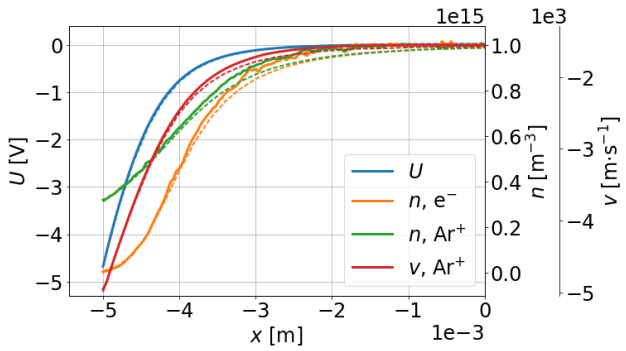

(a) Number density and potential profiles in front of a metal wall which is at the floating potential $U_f = -4.68\,\mathrm{V}$. (Solid lines – 3D PIC/MCC model results, dashed lines – analytical predictions.)

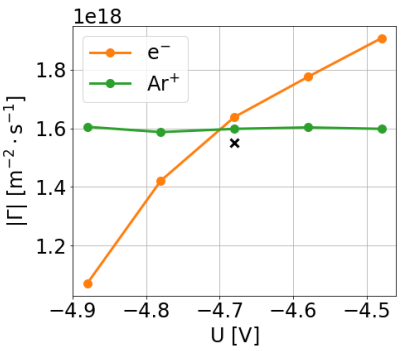

(b) Fluxes of charged particles on the metal wall for its different biases. Black cross marks the value $\Gamma = n_i u_B$.

Figure 4.2: Collisionless plasma sheath in front of an infinitely large metal wall.

Very good agreement can be seen between the number density and potential profiles in front of a metal wall at floating potential ($U_f = -4.68\,\mathrm{V}$ for given plasma conditions) predicted by equations (1.1.1), (1.1.2), (1.1.3) and those which were calculated by the developed 3D PIC/MCC code (Figure 4.2a). As the fluxes of positively and negatively charged particles on the wall at the floating potential should be equal, the accuracy of the 3D PIC/MCC model can be assessed also from their mismatch which is about 2.5 % of their nominal value (Figure 4.2b). As expected, variation of the bias of the metal wall around the floating potential value leads to an increasing inequality of the positive and negative fluxes.

4.1.2 Collisional plasma

To study sheaths in collisional plasma, scattering processes between charged and neutral particles were taken into account for the considered argon plasma (table 4.1). For simplicity, only isotropic elastic scattering on argon neutrals with constant collision cross section σ was defined for both electrons ($\sigma_e = 2.0 \times 10^{-20}\ \mathrm{m}^2$) and argon ions Ar^+ ($\sigma_i = 7.0 \times 10^{-19}\ \mathrm{m}^2$). The used values of the cross sections are based on the work Bogaerts et al. [1999] in the case of electrons and on the database Phelps [2013] in the case of Ar^+ ions. Several values of the neutral gas pressure ranging from 13.3 Pa to 532 Pa were considered. The temperature of the neutral gas was 300 K. (In particular, electrons scattered on the neutral argon particles of 1 eV temperature, so the same temperature as the electrons had. In such (rather artificial) settings, electrons did not loose their energy during the collisions with neutrals. In reality, electrons would be cooled down by the elastic collisions with neutrals; however, their energy would be supplemented by an energy source maintaining plasma which was not modelled in the 3D PIC/MCC calculations.)

The figure 4.3 shows how the profile of plasma number density in front of an infinitely large planar probe, which is kept at plasma potential (probe bias $U_p = 0\,\mathrm{V}$), changes for different values of neutral gas pressure. It can be clearly seen that the solution gets closer to the analytical solution of diffusion equation with increasing neutral gas pressure. The simple diffusion equation describing steady

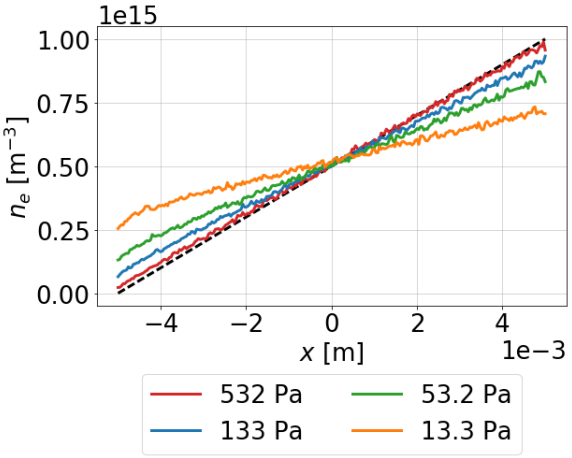

Figure 4.3: Electron number density profiles in front of an infinitely large planar probe with 0 V bias (= the probe is at plasma potential) for different values of neutral gas pressure. The dashed black line represents analytical solution of diffusion equation in 1D geometry.

state situation can be obtained from the continuity equation (2.2.1) where the expression for particle flux in the drift-diffusion approximation (2.2.5) is inserted

$$\begin{aligned} \frac{\partial n}{\partial t} + \nabla \cdot (n\boldsymbol{u}) &= I - R, \\ \nabla \cdot (n\boldsymbol{u}) &= \nabla \cdot [\operatorname{sgn}(q)\, \mu n \boldsymbol{E} - D\nabla n] = 0, \\ -D\Delta n &= 0. \end{aligned}$$

We assume that production I and loss R of charged particles is perfectly balanced; further, electric field can be neglected since no external potentials are considered in the investigated case and plasma can be regarded as quasi-neutral. Taking into account boundary conditions $n(x = x_A) = 0$ at the probe surface and $n(x = x_B) = n_0$ at the edge of bulk plasma, linear profile of the number density in front of the planar probe is obtained in the investigated 1D geometry. At higher pressures, the collisions between charged and neutral particles are frequent enough so the velocity distribution of the charged particles is isotropic and the assumptions of the drif-difusion approximation are well satisfied. It can be seen in the table 4.2 that the mean free path of electrons is much lower than the characteristic dimension of the considered computational domain in the case of the highest considered neutral gas pressure. On the contrary, large mean free path at low pressure is the reason why the number density profile approaches constant value of $0.5n_0$ – this would be a solution in the limit of collisionless plasma since only half of the particles with isotropic velocity distribution which are present in the plasma source enter the computational domain (only those with velocity directed towards the computational domain) and as there is no mechanism which would change the direction of the charged particle movement, strongly anisotropic half-Maxwellian velocity distribution of the charged particles is observed in the computational domain as a result.

Clearly, the solutions of the number density profile at higher considered gas pressures strongly depend on the size of the computational domain – in case

Neutral gas		Electrons		Ar^+ ions	
p [Pa]	n_g [m^{-3}]	λ_e [m]	τ_e [s]	λ_i [m]	τ_i [s]
1.33×10^1	3.21×10^{21}	1.56×10^{-2}	2.33×10^{-8}	4.45×10^{-4}	1.12×10^{-6}
5.32×10^1	1.28×10^{22}	3.91×10^{-3}	5.84×10^{-9}	1.12×10^{-4}	2.80×10^{-7}
1.33×10^2	3.21×10^{22}	1.56×10^{-3}	2.33×10^{-9}	4.45×10^{-5}	1.12×10^{-7}
5.32×10^2	1.28×10^{23}	3.91×10^{-4}	5.84×10^{-10}	1.12×10^{-5}	2.80×10^{-8}

Table 4.2: Characteristic parameters of electron and Ar^+ ion collisions at different values of neutral gas pressure.

of the larger computational domain, the gradient of number density would be lower. It is a consequence of the fact that an ideal 1D case with infinitely large metal wall is being resolved. Further, it can be seen that in the selected settings, really the transition regime between collisional and collisionless plasma has been captured. In the following paragraphs, the case of **neutral gas pressure 532 Pa** is investigated in detail. Such a pressure is high enough for the drift-diffusion approximation to be valid with sufficient accuracy, and results of the developed 3D PIC/MCC model could thus be directly compared with fluid models based on the drift-diffusion approximation.

If electric bias (with respect to the plasma potential) is applied on the probe, sheath layer is created. In the figures 4.4 and 4.5, solution of the sheath layer which was obtained by particle and fluid models is presented for different values of the probe bias. Fluid model results are based on the drift-diffusion approximation (3.3.1). Two variants of the fluid model were implemented: the first one with constant transport coefficients μ and D whose values are given by expressions (2.2.6)

$$\mu = \frac{|q|}{m\nu}, \quad D = \frac{\mathrm{k_B}T}{m\nu}. \tag{4.1.1}$$

Collision frequency in these expressions was evaluated according to the relation

$$\nu = n_g \sigma v_{th} = n_g \sigma \left(\frac{8\mathrm{k_B}T}{\pi m} \right)^{1/2}, \tag{4.1.2}$$

which follows from the more general expression

$$\nu = n_g \int \sigma(v_r) v_r f_1(\boldsymbol{v_1}) f_2(\boldsymbol{v_2}) \mathrm{d}\boldsymbol{v_1} \mathrm{d}\boldsymbol{v_2}, \tag{4.1.3}$$

taking into account several assumptions: collision cross section is independent of the relative velocity $v_r = |\boldsymbol{v_1} - \boldsymbol{v_2}|$; the characteristic velocities of the target particles are much less than those of the incident particles ($v_r \approx |\boldsymbol{v_1}|$); velocity distribution of the incident particles is isotropic and Maxwellian. Taking into account the simplified relations (4.1.1) for the considered plasma (table 4.1), the values presented in the table 4.3 are obtained.

The second variant of the fluid model used spatially varying profiles of the transport coefficients which were calculated by the 3D PIC/MCC model according to the expressions (3.2.1), (3.2.2)

$$\mu_{PIC} = \frac{|q|}{m \left\langle n_g \sigma(v) v \right\rangle}, \quad D_{PIC} = \frac{1}{3} \left\langle \frac{v^2}{n_g \sigma(v) v} \right\rangle. \tag{4.1.4}$$

	Electrons	Ar^+ ions
ν_{const} $[s^{-1}]$	1.71×10^9	3.57×10^7
μ_{const} $[m^2 \cdot V^{-1} \cdot s^{-1}]$	1.03×10^2	6.76×10^{-2}
D_{const} $[m^2 \cdot s^{-1}]$	1.03×10^2	1.75×10^{-3}

Table 4.3: Collision frequency ν and transport coefficients μ and D of the modelled plasma evaluated according to the equations (4.1.1) and (4.1.2).

	Electrons	Ar^+ ions
ν_{PIC} $[s^{-1}]$	1.70×10^9	5.05×10^7
μ_{PIC} $[m^2 \cdot V^{-1} \cdot s^{-1}]$	1.03×10^2	6.76×10^{-2}
D_{PIC} $[m^2 \cdot s^{-1}]$	8.68×10^1	1.48×10^{-3}

Table 4.4: Collision frequency ν and transport coefficients μ and D of the modelled plasma evaluated by the 3D PIC/MCC code in the case when the probe is at plasma potential ($U_p = 0\,\mathrm{V}$).

In the case when the probe is at plasma potential ($U_p = 0\,\mathrm{V}$), the particle model provides spatially constant transport coefficients of the values which are presented in the table 4.4.

Comparing the values in the tables 4.3 and 4.4, it can be seen that the 3D PIC/MCC model provides the same value of the electron collision frequency as the analytical prediction whereas it shows different value for the Ar^+ ions. The reason of this discrepancy is that the analytical prediction according to the expression (4.1.2) neglects the movement of neutral gas particles. In the case of Ar^+ ions, this effect has to be taken into account since their mass and temperature is the same as of the argon neutrals; even stationary Ar^+ ion might undergo significant number of collisions with the neutral particles in the background. This effect is implicitly involved in the 3D PIC/MCC model results and thus, it shows larger value of the Ar^+ ion collision frequency. Further, it can be seen that the values of the mobility coefficients provided by the 3D PIC/MCC model are exactly the same as the analytical prediction. The reason is that the 3D PIC/MCC model uses simplified way for mobility coefficient evaluation which lies in the averaging of the expression $n_g\sigma(v)v$ over the velocity distribution of the charged particles. If the velocity distribution function is isotropic and Maxwellian, it is equivalent to the expression (4.1.2). However, it should be noted that this approach does not provide correct values of the mobility coefficient for Ar^+ ions for which the more general and more computationally demanding expression (4.1.3) should be used instead. Finally, it can be seen that the values of diffusion coefficients for both electrons and Ar^+ ions which are evaluated by the 3D PIC/MCC model are about 15% lower than the analytical prediction. The reason is inconsistency of both definitions of the diffusion coefficient. If Maxwellian distribution function is assumed, the expression (4.1.4) for the diffusion coefficient can be written in the form

$$D_{PIC} = \frac{1}{3}\left\langle \frac{v^2}{n_g\sigma(v)v} \right\rangle = \frac{1}{3}\left\langle \frac{v}{n_g\sigma(v)} \right\rangle = \frac{1}{3}\frac{v_{th}}{n_g\sigma} = \frac{1}{3n_g\sigma}\left(\frac{8k_BT}{\pi m}\right)^{1/2}.$$

According to this expression, we obtain $D_e = 8.71 \times 10^1$ m$^2 \cdot$ s^{-1} for electrons and $D_{Ar} = 1.48 \times 10^{-3}$ m$^2 \cdot$ s^{-1} for Ar$^+$ ions of the considered plasma. These values well agree with the results of the 3D PIC/MCC model reported in the table 4.4. Taking into account the equality $1/2mv_{rms}^2 = 3/2k_BT$ which holds for the ideal monatomic gas, the expression (4.1.1) for the diffusion coefficient can be written in the form

$$D_{const} = \frac{\mathrm{k_B}T}{m\nu} = \frac{\mathrm{k_B}T}{mn_g\sigma v_{th}} = \frac{1}{3}\frac{v_{rms}^2}{n_g\sigma v_{th}} = \frac{1}{n_g\sigma}\left(\frac{\pi k_BT}{8m}\right)^{1/2}.$$

As a result, there is a difference between both definitions

$$\frac{D_{PIC}}{D_{const}} = \frac{8}{3\pi}.$$

It can be seen that the expression D_{const} could be obtained from definition of D_{PIC} if the mean value over the particle distribution function in the expression (4.1.4) would be considered separately in the numerator and denominator

$$D_{const} = D'_{PIC} = \frac{1}{3}\frac{\langle v^2\rangle}{\langle n_g\sigma(v)v\rangle}.$$

Let us now consider the case when the planar probe is at the plasma potential ($U_p = 0$ V). Flux on the probe is given only by diffusion in this case since the electric field is zero and density of electric current j on the probe can be evaluated using the following expression

$$j = q\Gamma = qD|\nabla n| = qDn_0/L, \tag{4.1.5}$$

where Γ is the charged particle flux on the probe which is perpendicular to the probe in the considered geometry, n_0 is plasma density and L is the size of the computational domain. 1D nature of the problem with linear decrease of plasma number density from n_0 at the plasma source towards zero at the probe surface allows us to consider the equality $|\nabla n| = n_0/L$. In the table 4.5, currrent densities on the probe according to the expression (4.1.5) for previously discussed diffusion coefficients D_{const} and D_{PIC} are compared to the values calculated by the 3D PIC/MCC model. It can be seen that very good agreement between electron current density calculated by 3D PIC/MCC model and its value based on the D_{PIC} coefficient is obtained. On the contrary, quite different values of Ar$^+$ ion current density are reported, especially for the 3D PIC/MCC model results. The reason of this discrepancy might be the fact that both predictions of the current density based on the diffusion coefficients D_{const} and D_{PIC} use the simplified expression for the collision frequency (4.1.2) instead of the more accurate expression (4.1.3) which is implicitly involved in the calculations by the 3D PIC/MCC model. Another reason might be the accuracy of the 3D PIC/MCC model which is limited by the discrete nature of the modelled particle ensemble. The ion current is very low, particles impinge the probe surface only occasionally and this might distort the value of the current density which is obtained by averaging of its fluctuations in time.

Before we get to the detailed discussion of the obtained results, we will summarize the general observations regarding the differences between each of the modelling techniques used in this place.

Model	$j_e\,[\mathrm{A}\cdot\mathrm{m}^{-2}]$	$j_{Ar}\,[\mathrm{A}\cdot\mathrm{m}^{-2}]$
$j = qD_{const}\lvert\nabla n\rvert$	-1.64	2.80×10^{-5}
$j = qD_{PIC}\lvert\nabla n\rvert$	-1.39	2.38×10^{-5}
3D PIC/MCC	-1.33	3.71×10^{-5}

Table 4.5: Comparison of the analytical predictions and 3D PIC/MCC model results of the current density on the solid wall which is at the plasma potential.

Inertial term The developed fluid models are based on the drift-diffusion approximation which can be considered at high enough pressure when the movement of the charged particles is significantly determined by their collisions with neutrals. This assumption is certainly fulfilled in the studied case of neutral gas pressure 532 Pa, as can be seen in the figure 4.3. The usage of drift-diffusion approximation is well defensible for electrons with their low mass and high thermal energy. In their case, it is possible to neglect the inertial term on the left side of the equation of motion (2.2.4), which is not possible to do in the case of positive ions with their large mass and low temperature. In this aspect, fluid models differ from the PIC/MCC model, which implicitly includes the influence of the inertial term for positive ions in its results.

And what does neglection of the inertial term actually means? Let us consider the equation of motion of the charged particles in the following form

$$nm\left(\frac{\partial \boldsymbol{u}}{\partial t} + \boldsymbol{u}\cdot\nabla\boldsymbol{u}\right) = qn\boldsymbol{E} - \nabla p - nm\nu\boldsymbol{u}.$$

Let us further consider steady state and let us neglect collisions at the moment (assuming e. g. that the drift velocity $\boldsymbol{u}$ is very low). Thus, we end up with the following equation of motion

$$nm\boldsymbol{u}\cdot\nabla\boldsymbol{u} = qn\boldsymbol{E} - \nabla p.$$

Neglection of the inertial term on the left side of the equation of motion leads to the equation

$$0 = qn\boldsymbol{E} - \nabla p,$$

which leads to the Boltzmann expression for number density (assuming $\boldsymbol{E} = -\nabla\phi$ and $p = n\mathrm{k_B}T$)

$$n = n_0 \exp\left(-\frac{q\phi}{\mathrm{k_B}T}\right).$$

Neglection of the inertial term thus means that positive ions are in thermal equilibrium with the electric field.

Anisotropy of the distribution function In its simplest form, drift-diffusion approximation (2.2.5) assumes isotropic Maxwellian distribution function, or very small deviations from this distribution in the case of a two-term approximation (2.2.8). On the contrary, PIC/MCC model does not impose any assumptions on the distribution function and it is able to precisely describe cases with general, (strongly) anisotropic distribution function. In the case of the studied infinitely

large planar probe, this condition can occur in the close proximity to the probe, where no charged particles come from its direction. The strong anisotropy of the distribution function manifests itself only in a region with a characteristic size corresponding to the mean free path of the particles, which is very low in the studied case of 532 Pa pressure (see table 4.2). In the rest of the computational domain, the distribution function is only weakly anisotropic – a directed flow of charged particles towards the probe is observed which means that the number of particles with velocity directed towards the probe must prevail over those which move in the opposite direction at each point of the computational domain. Since the modelled planar probe is infinitely large, the disturbance caused by its presence manifests itself even at great distances. As a consequence, linear profile of number density between the probe and source of the charged particles is established.

Boundary conditions For calculation of the electric potential and number density distribution in the computational domain, the developed fluid models impose Dirichlet boundary conditions (BC) at its outer boundaries corresponding to the probe surface and to the interface with undisturbed plasma. The PIC/MCC model also uses Dirichlet BC for calculation of the electric potential distribution – probe bias U_p with respect to the plasma potential is prescribed on the probe surface and $U_p = 0$ V is prescribed at the boundary between the computational domain and the source of the charged particles. It turns out that in the case of negative probe bias it would be advisable to perform the calculations on larger computational domain. In the current settings, it can be seen (e. g. figure 4.4a) that the decrease of the negative potential in the direction from the probe is relatively slow and there is a non-zero electric field at the outer boundary of the computational domain which is adjacent to the charged particle source. In contrast, the electric field is zero in the particle source, where undisturbed plasma is assumed, and it leads to a "jump" in the distribution function of the charged particles at this boundary. Computational domain should be larger in order to model the pre-sheath region accurately enough. (In fact, the calculated profile of the electric field should be independent of the chosen size of the computational domain.) In the PIC/MCC model, number density of the charged particles at the boundaries of the computational domain is established self-consistently, according to the solution of the equations of motion. In the fluid models, Dirichlet BC are prescribed at the outer faces of the computational domain: $n = n_0$ at the interface with undisturbed plasma and $n = 0$ on the probe surface. (The usage of the Dirichlet BC $n = 0$ on the probe surface is questionable – in some cases, it is more appropriate to prescribe flux of the charged particles on the probe which corresponds to the Neumman boundary condition. Prescription $n = 0$ on the probe surface can significantly affect number density profile in the sheath which influences its size and also distance at which the electric bias of the probe is shielded off.)

General comparison of the models The fluid model with constant transport coefficients does not include their dependence on the mean energy of the particles (through the temperature and collision frequency) which can vary a lot in the computational domain. In this view, it is the simplest and least accu-

rate model used. The fluid model with variable transport coefficients is more accurate; however, it is still limited by the assumptions of the fluid modelling approach which were discussed in the previous paragraphs. Implicitly, the most accurate is the PIC/MCC model. The results of the fluid models are presented primarily for a deeper understanding of the achieved results. Comparison of different modelling approaches allows us to distinguish manifestations of different physical mechanisms in the results.

In total, we can summarize the following:

- The developed fluid models neglect the inertial term in the equation of motion which can be important for positive ions.
- The fluid models assume isotropic Maxwellian distribution functions of the charged particles and dominance of collisions with neutral particles.
- The applied boundary conditions can significantly affect the obtained solution, especially in the case of negative probe bias.
- Transport coefficients can significantly vary within the computational domain.

Characteristic lengths The modelled plasma has the following characteristic lengths:

- Debye length: $\lambda_D = 2.35 \times 10^{-4}$ m,
- Mean free path of electrons: $\lambda_e = 3.91 \times 10^{-4}$ m,
- Mean free path of Ar^+ ions: $\lambda_i = 1.12 \times 10^{-5}$ m.

It can be seen that $\lambda_i \ll \lambda_D$ and we can thus speak about collisional sheath in the case of positive ions where dozens of collisions can happen ($\lambda_D/\lambda_i \approx 20$). In the case of electrons, $\lambda_e > \lambda_D$ does apply, but if we consider that sheath typically has a size of several Debye lengths ($\approx 3\lambda_D$), then we can also speak of a collisional sheath for electrons where units of collisions can happen ($3\lambda_D/\lambda_e \approx 1.8$). Moreover, Debye length λ_D can be higher at the sheath edge because lower number density of the charged particles is observed here.

Description of the sheath structures In the figures 4.4 and 4.5, sheath structures in front of the infinitely large planar probe are presented in terms of the spatial profiles of electric potential and number density of the charged particles. Profiles of the transport coefficients calculated by the 3D PIC/MCC model are presented as well. The figures display plasma sheaths for various values of the electric bias (negative and positive) of the probe with respect to the plasma potential. The figures show results of three different modelling approaches (those ones which were already discussed in the previous paragraphs) – 3D PIC/MCC model, fluid model with constant transport coefficients given by expressions (4.1.1) and fluid model with variable transport coefficients which were evaluated by the 3D PIC/MCC model.

It can be seen that the character of the plasma sheath is different when the probe is biased negatively or positively. In the case of positive bias, the probe potential is well shielded within the computational domain and the applied boundary conditions do not have a major effect on the solution. In the case of negative bias, the shielding is ensured by positive ions whose shielding effect is weakened by electrons which, thanks to their high thermal energy, can get very close to the probe. Further, part of the electric field penetrates into the pre-sheath so that the ions can be accelerated to a high enough speed to overcome the thermal energy of electrons and to be able to create positive space charge in front of the probe. As a result, negative probe potential is shielded on larger distance and the applied boundary conditions can significantly affect the obtained solution.

Let us now look at the results in more detail. In the case of **the positive bias** of the probe, both fluid models give similar results regarding the shape of the sheath. It is due to the fact that the transport coefficients do not change much in the computational domain and both fluid models are therefore equivalent here. Transport coefficients begin to change more significantly only in the sheath area, where the concentration of charged particles is relatively low. It can be seen that both fluid models differ quite a lot from the 3D PIC/MCC model – they show that the shielding of the electric potential occurs at greater distance and the area where quasi-neutrality is violated is also larger. In the end, the fluid models and the 3D PIC/MCC model use the similar amount of charge to shield the probe potential – the 3D PIC/MCC model shows a higher value of negative charge density on a smaller area, compared to a lower value of charge density on a larger area in the case of the fluid model. The reason for the different behavior of both types of models is apparently the neglect of the inertial term in the case of the drift-diffusion approximation, on which both fluid models are based. Neglecting the inertial term in the equation of motion of the ion (if we do not consider collisions at the moment) means that their distribution follows the Boltzmann relation for number density as in the case of electrons and they are therefore in thermal equilibrium with the electric field. As a result, the ions are more mobile, no energy of the electric field is consumed on the inertial term and they can thus significantly reduce the shielding effect of the electrons which are in front of the positively biased probe. In this consequence, the electric potential is shielded at greater distance and greater electron flow into the sheath is needed, which is manifested by a steeper number density profile in the area between the undisturbed plasma and the sheath edge. This can be also observed in the figure with IV characteristics (figure 4.7), where for the positive probe bias higher values of the electron current can be observed in the fluid model than in the 3D PIC/MCC model.

Let us now take a closer look at the case of **negative probe bias**. It can be seen that electric field penetrates outside of the sheath area, which we consider to be the area of quasi-neutrality violation. Here, the electric field accelerates the positive ions to a sufficiently high directional speed so that they can overcome the thermal energy of the electrons and form a shielding layer with a positive space charge density. This behavior is demonstrated e. g. in the figure 4.6 where the sheath structure in front of the planar probe at $U_p = -8$ V bias is shown. Such a bias approximately corresponds to the floating potential, which was evaluated at $U_f = -8.79$ V from the IV characteristic calculated by the

3D PIC/MCC model (see figure 4.7 and table 4.6). It can be seen from the 3D PIC/MCC model results that the positive ions have a directed velocity of about 40 $\mathrm{m \cdot s^{-1}}$ at the sheath edge (at $x = -1.0 \times 10^{-3}$ m). This value is many times lower than the theoretical value of the Bohm velocity u_B, which for the electrons with a temperature of $T_e = 1$ eV is about $u_B = 1550$ $\mathrm{m \cdot s^{-1}}$ (equation (1.1.5)). According to the theory, in the presence of collisions between the charged particles and neutrals, the velocity of the ions at the sheath edge is actually lower than the Bohm velocity. The equation (1.1.13) predicts the value $u_s = 240$ $\mathrm{m \cdot s^{-1}}$ and the equation (1.1.14) predicts $u_s = 190$ $\mathrm{m \cdot s^{-1}}$. (These values are obtained for $T_e = 1$ eV and $n_e = 2.5 \times 10^{14}$ $\mathrm{m^{-3}}$ which corresponds to the electron number density at the sheath edge.) The value predicted by the 3D PIC/MCC model is still lower than the values predicted by the theory of the collisional sheaths. One of the reasons could be that the expressions (1.1.13) and (1.1.14) include only the effect of ion collisions and do not take into account electron collisions with neutrals. Another reason could be that the energy of the electrons at the sheath edge is lower than 1 eV since they are slowed down by the repulsive electric field of the probe here. As a result, the Bohm velocity is also lower, from which the ion velocity at the sheath edge is calculated according to the relations (1.1.13) and (1.1.14). A third reason for the lower observed ion velocity at the sheath edge than predicted by the theory may be the effect of the Dirichlet boundary condition applied to the electric field at the interface between the computational domain and the source of the charged particles, which significantly affects the distribution of the electric field.

In general, in the case of a negative bias of the probe, it can be observed that the potential is shielded in fluid models at shorter distances than shown by the 3D PIC/MCC model. This is the opposite situation than in the case of a positive probe bias, where the potential given by the fluid models is attenuated at greater distances. The reason is apparently again related to the neglect of the inertial term for positive ions in the case of fluid models. Due to the neglect of the inertial term, the positive ions are more mobile, they shield the negative bias of the probe well and do not allow the electrons to interfere as much with the positive sheath.

In the case of the probe bias of $U_p = -2$ V (figure 4.4a) it can be observed that the number density profile given by the fluid model with variable transport coefficients is closer to the results of the 3D PIC/MCC model at a greater distance from the probe than to the results of the fluid model with constant transport coefficients. The reason is a significant decrease in the diffusion coefficient in the direction towards the probe (figure 4.4b) – in order to maintain the flux of charged particles, gradient of the number density must increase in this direction, leading to a concave number density profile in the case of 3D PIC/MCC model and fluid model with variable transport coefficients. Near the probe, both fluid models give the same results, which differ from the 3D PIC/MCC model – it is apparently due to the application of the Dirichlet boundary condition $n = 0$ on the probe surface in the case of the fluid models. Due to the fact that both fluid models in the sheath area are identical in terms of the number density distribution, the potential is shielded by the sheath in the same way and the electric field that gets outside the sheath decreases at the same rate. As a result, both fluid models give the same course of the electric potential in the entire computational domain,

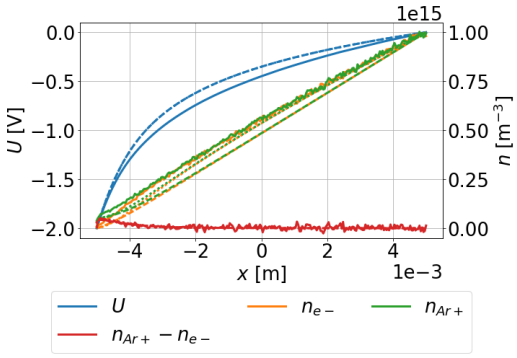

(a) Potential and number density profiles in case of $U_p = -2\,\mathrm{V}$ probe bias

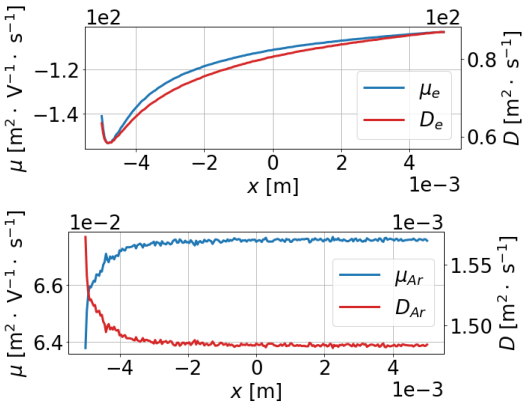

(b) Profiles of transport coefficients in case of $U_p = -2\,\mathrm{V}$ probe bias

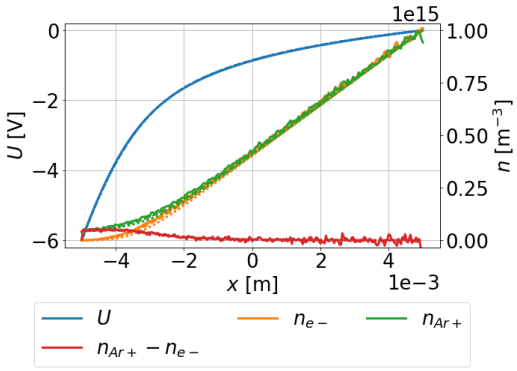

(c) Potential and number density profiles in case of $U_p = -6\,\mathrm{V}$ probe bias

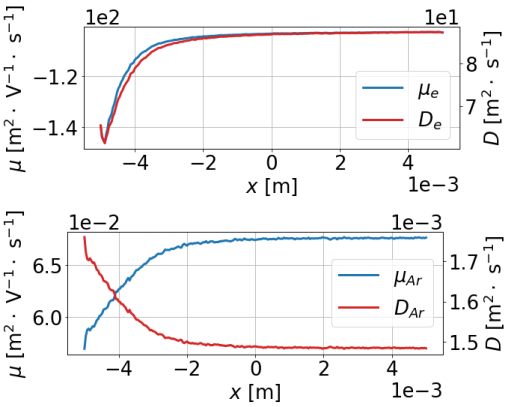

(d) Profiles of transport coefficients in case of $U_p = -6\,\mathrm{V}$ probe bias

Figure 4.4: Sheath structure in front of an infinitely large planar probe which is kept at **negative** electric bias with respect to the plasma potential, neutral gas pressure 532 Pa. Figures on the left compare results of 3D PIC/MCC model (full line) with those of fluid model with constant (dashed line) and with spatially dependent transport coefficients (dotted line). Profiles of transport coefficients on the right were calculated by 3D PIC/MCC model.

despite the fact that they differ in the course of the number density of the charged particles in the region of the quasi-neutral plasma.

Interestingly, for the probe bias of $U_p = -6$ V, all models show the same number density and electric potential profiles. The fact that the 3D PIC/MCC model approaches fluid models at higher voltages would indicate that the positive ions start to behave according to the Boltzmann relation for the number density in these conditions – at a higher electric field, the ratio between the potential energy of the positive ions and their kinetic energy is greater, and the inertial term thus apparently loses its meaning. However, the models still show different values of the (primarily electron) current, as can be seen in the figure 4.7 with IV characteristics. This is apparently due to the different values of the diffusion coefficients used in the models.

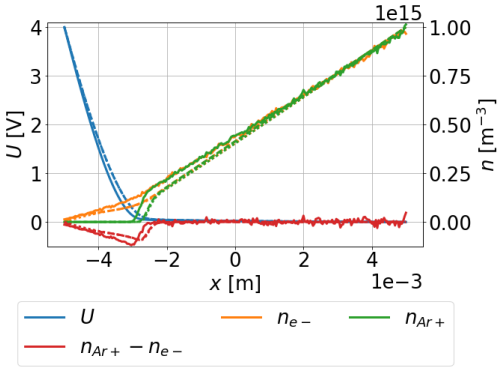

(a) Potential and number density profiles in case of $U_p = 4\,\mathrm{V}$ probe bias

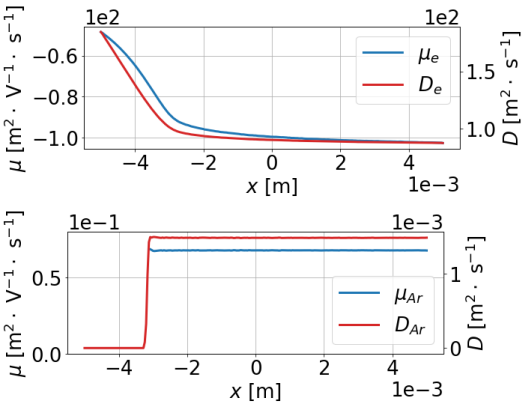

(b) Profiles of transport coefficients in case of $U_p = 4\,\mathrm{V}$ probe bias

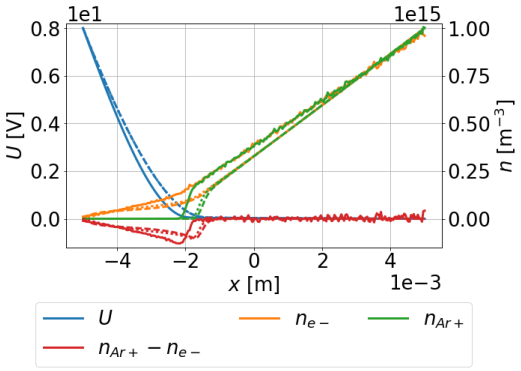

(c) Potential and number density profiles in case of $U_p = 8\,\mathrm{V}$ probe bias

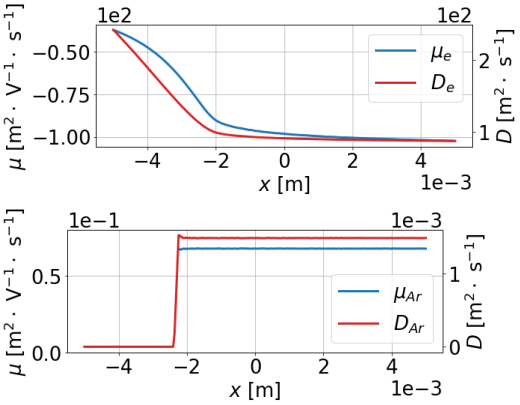

(d) Profiles of transport coefficients in case of $U_p = 8\,\mathrm{V}$ probe bias

Figure 4.5: Sheath structure in front of an infinitely large planar probe which is kept at **positive** electric bias with respect to the plasma potential, neutral gas pressure 532 Pa. Figures on the left compare results of 3D PIC/MCC model (full line) with those of fluid model with constant (dashed line) and with spatially dependent transport coefficients (dotted line). Profiles of transport coefficients on the right were calculated by 3D PIC/MCC model.

IV characteristics Figure 4.7 shows the IV characteristics calculated using the particular models, and table 4.6 presents the values of the plasma parameters that were derived from them.

Let us now look in more detail at the calculated IV characteristics in the figure 4.7. The gray lines in the figure represent the linear fits of the electron current in the area of the negative probe bias from which the electron temperature is derived. In the case of the IV characteristic calculated using the 3D PIC/MCC model, one point was omitted – the one for the probe bias of $U_p = -12\,\mathrm{V}$, because it deviated significantly from the linear dependence. In the case of the IV characteristics calculated using the fluid model with constant transport coefficients, two fits are presented. The first fit (solid line) is done for all values of the electron current at the negative probe bias. However, it can be seen that for a low probe voltage the dependence is not exactly linear and therefore it is more appropriate to perform the fitting only in the linear part of the characteristic, which can be observed for

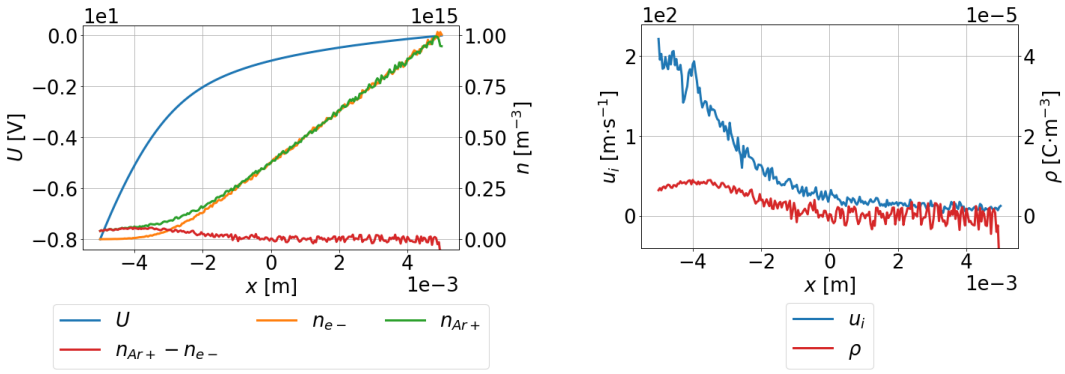

(a) Electric potential and number density

(b) Net space charge density and drift velocity of positive ions

Figure 4.6: Sheath structure in front of an infinitely large planar probe which is kept at negative electric bias $U_p = -8$ V with respect to the plasma potential calculated by the 3D PIC/MCC model, neutral gas pressure 532 Pa.

a higher negative probe voltage, and it is the second fit (dashed line).

In the case of the **positive probe bias**, both fluid models show a larger electron current than the 3D PIC/MCC model and also show its faster growth with increasing probe bias. The fluid model with variable transport coefficients and the 3D PIC/MCC model show a very good agreement of the magnitude of the electron current for the probe bias voltage $U_p = 0$ V. The fluid model with constant transport coefficients, in contrast to them, shows a higher value of the electron current, precisely in proportion to the diffusion coefficients used in the particular models (see the discussion on the coefficients D_{const} and D_{PIC} for tables 4.3, 4.4, 4.5 and 4.6). As the positive bias of the probe increases, both fluid models maintain this systematic offset in the value of the electron current drained by the probe. Compared to the 3D PIC/MCC model, they show a faster growth of the electron current with increasing positive probe bias. This is apparently related to differences in the shape of the sheath at positive probe bias, which lead to a steeper number density profile between the undisturbed plasma and the sheath edge and thus to a higher flux of charged particles to the probe (see the detailed discussion of the sheath shape in the case of the positive probe bias in one of the previous paragraphs).

In the case of the **negative probe bias**, it can be observed that the electron current given by the fluid model with constant transport coefficients is much larger than the current given by the 3D PIC/MCC model. This is due to the fact that the fluid model with constant transport coefficients neglects the drop in electron diffusivity towards the probe – it thus overestimates their thermal energy and as a result a higher electron current is observed. Further, it can be observed that the fluid model with constant transport coefficients does not follow linear dependence of the electron current for the small negative bias of the probe which would indicate that the electrons do not behave according to the Maxwellian distribution in this region. On the contrary, the fluid model with variable transport coefficients show lower electron current than the 3D PIC/MCC model. With the 3D PIC/MCC model, it has the same profile of transport coefficients, so the reason for the difference is rather the neglect of the inertial

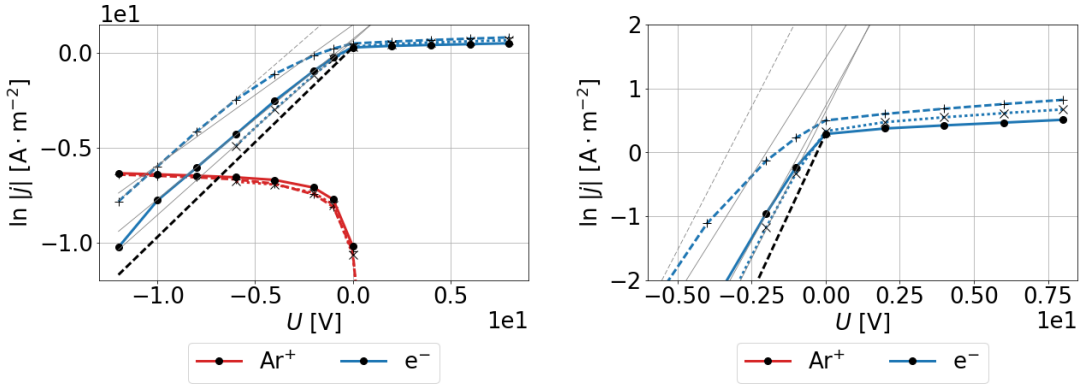

(a) Full voltage range

(b) Detail on the electron current density

Figure 4.7: IV characteristics of an infinitely large planar probe. Three modelling approaches are compared: 3D PIC/MCC model (full line), drift-diffusion fluid model with constant transport coefficients (dashed line) and drift-diffusion model with spatially dependent transport coefficients (dotted line). Black dashed line denotes current density of electrons with temperature $T_e = 11\,605$ K in the collisionless case according to the equation (1.2.2). Gray lines represent linear fits of the particular IV characteristics.

term in the drift-diffusion approximation of the fluid model – the more mobile ions shield the negative bias of the probe well and do not allow the electrons (with their high thermal energy) to interfere so much with the positive sheath. As a result, lower electron current is observed by the fluid model with variable transport coefficients. It is interesting that the ion current values match fairly well for all the models used.

Let us now focus on the values of plasma parameters which are listed in the table 4.6; let us first explain what they mean. The values in the row labeled "Collisionless" correspond to either the analytical values for the collisionless plasma or to the input parameters of the models: $j_{e,0}$ is the electron saturation current given by expression

$$j_{e,0} = \frac{1}{4} e n_0 v_{th} = \frac{1}{4} e n_0 \left(\frac{8 k_B T_e}{\pi m_e} \right)^{\frac{1}{2}},$$

U_f is the floating potential given by equation (1.1.9) and j_f is the current density of the charged particles on the probe which is at the floating potential (equation (1.1.8)). Number density n_e and temperature T_e are the parameters of the undisturbed plasma – from the point of view of the models, these are the input parameters defining the charged particles in the source. We want to obtain these values by evaluating the calculated IV characteristics and verify in this way that the models give correct results and the methodology for evaluating the IV characteristics is correct. The values in the remaining rows of the table 4.6 are obtained from the outputs of the particular models used. Current density $j_{e,0}$ is direct output of the models and it is the current density of electrons on the probe which is at the plasma potential ($U_p = 0$ V). These values were already discussed in the table 4.5. The temperature T_e was obtained by fitting the electron current in the region of the negative bias of the probe and calculating according to the formula

Model	$j_{e,0}$ [A · m^{-2}]	T_e [K]	n_e [m^{-3}]	U_f [V]	j_f [A · m^{-2}]
Collisionless	26.8	11 605	1.00×10^{15}	−4.68	1.52×10^{-1}
3D PIC/MCC	1.33	13 884	4.54×10^{13}	−8.79	1.58×10^{-3}
Fluid – variable μ, D	1.39	12 632	4.97×10^{13}	−7.80	1.48×10^{-3}
Fluid – constant μ, D	1.65	18 614	4.86×10^{13}	−10.9	1.57×10^{-3}

Table 4.6: Evaluation of the IV characteristics of an infinitely large planar probe which are presented in the figure 4.7.

(1.2.4). Number density n_e was evaluated according to the formula (1.2.5) where $j_{e,0}$ given by the particular model and T_e obtained by the fitting procedure were substituted. The floating potential U_f and its corresponding current density j_f were read from the IV characteristics graph as the intersection of the electron and ion current densities.

In the case when the probe is at the plasma potential ($U_p = 0$ V), the values of the electron current obtained from the 3D PIC/MCC model ($j_{e,0} = 1.33$ A · m^{-2}) and from the fluid model with variable transport coefficients ($j_{e,0} = 1.39$ A · m^{-2}) match very well. In contrast, the current given by the fluid model with constant transport coefficients is higher, precisely in proportion to the magnitude of the diffusion coefficients used ($j_{const} = j_{var} D_{const}/D_{PIC} = 1.39 \cdot 1.03 \times 10^2/(8.68 \times 10^1) = 1.65$ A · m^{-2}, see also the tables 4.3 and 4.4). Compared to the Maxwellian flow of a collisionless plasma, these values are approximately 20× smaller. It should be noted that the values of the current given by all of the used computer models are closely related to the size of the computational domain which directly affects the magnitude of the number density gradient and thus the flux of the charged particles.

It can be seen that all the used computer models show a higher electron temperature than their temperature entered in the undisturbed plasma ($T_e = 11\,605$ K). All models show a higher electron current in the area of the negative bias of the probe than would correspond to Maxwellian electrons at a temperature of $T_e = 11\,605$ K. The biggest deviation (+60%) can be seen in the results of the fluid model with constant transport coefficients, where the reason is the neglect of the drop in diffusivity of electrons near the probe due to their decreasing root mean square velocity in this direction which ultimately leads to an overestimation of their thermal energy (see also discussion on the figure 4.7). However, higher electron temperature is observed also for the 3D PIC/MCC model (+20%) and for the fluid model with variable transport coefficients (+9%). The reason for the increased observed temperature cannot be the neglect of the inertial term in the drift-diffusion approximation in the fluid models, since the increased temperature is also observed for the 3D PIC/MCC model. Collisions with neutral particles should also not be a reason, as these do not increase the temperature of charged particles. In the 3D PIC/MCC model, we try to keep the numerical heating under control by choosing the appropriate time step and the size of the grid cells. However, it can have a smaller effect and may be the reason why the 3D PIC/MCC model gives higher values of the electron current (and thus also the temperature) than the fluid model with variable transport coefficients in the area of the negative bias of the probe. Perhaps the higher than expected value of

the electron current (by all used computer models) could be due to the presence of positive ions in front of the negatively biased probe. Indeed, the collisionless theory of probe measurements (see the chapter 1.2.1) assumes that the fluxes of the different charged particle species to the probe are independent of each other and can be calculated separately. Formula 1.2.2, from which follows relation 1.2.4 for evaluating the electron temperature, was derived without taking into account the presence of positive ions in front of the negatively charged probe. Their presence effectively reduces the negative potential of the probe which is "seen" by electrons and more of them can thus reach its surface.

Due to the lower observed electron current $j_{e,0}$ in the case of the probe bias $U_p = 0$ V, we observe for all models after evaluation according to formula 1.2.5 a proportionally lower ($\approx 20\times$) number density of electrons n_e than that prescribed in the source of the charged particles. We can therefore conclude that the used methodology for evaluating the IV characteristic is not appropriate in the studied case.

All the models used show a lower value of the floating potential U_f than the theoretical value corresponding to a collisionless plasma. The reason is apparently the slower decreasing observed electron current on the probe in the case of its negative bias (due to the effectively higher electron temperature) and apparently also a lower ion current. It can be observed that the value of the current density j_f at the floating potential is similar for all used models, but it is two orders of magnitude lower than the theoretical value corresponding to a collisionless plasma. The reason can be both collisions with neutral particles, which limit the flux of charged particles, and also low number density of the charged particles at the sheath edge.

4.2 Plasma sheath of a planar probe in 3D

The results in this chapter demonstrate the ability of the developed 3D PIC/MCC code to resolve 3D problems. For that purpose, sheath profiles and IV characteristic of a simple planar probe in 3D space were calculated. The investigation was done for argon plasma of the same properties as in the previous chapter 4.1.2. Plasma parameters and settings of the 3D PIC/MCC model are summarized in the table 4.7. Geometry of the computational domain with the planar probe is depicted in the figure 4.8. The particle source adjoins the computational domain on all of its outer faces.

At first, characteristic lengths of the modelled case will are discussed. They are as follows:

- Debye length: $\lambda_D = 2.35 \times 10^{-4}$ m,
- Mean free path of electrons: $\lambda_e = 3.91 \times 10^{-4}$ m,
- Mean free path of Ar^+ ions: $\lambda_i = 1.12 \times 10^{-5}$ m,
- Equivalent probe radius: $r_p = 7.82 \times 10^{-4}$ m. (We model a planar probe of finite dimensions, which can be viewed from a sufficiently large distance as a spherical probe of equivalent radius r_p. The radius r_p corresponds to a sphere that has the same volume as the modelled planar probe of finite dimensions.)

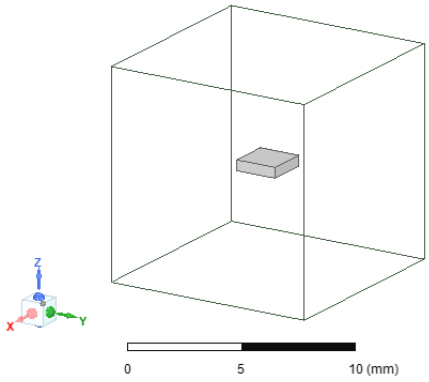

Figure 4.8: Geometry of the planar probe and 3D computational domain.

Temperature	$T_e = 11\,600\,\mathrm{K}$ $(= 1\,\mathrm{eV})$, $T_i = 300\,\mathrm{K}$
Number density	$n_e = n_i = 10^{15}\,\mathrm{m}^{-3}$
Plasma frequency	$\omega_p = 1.78 \times 10^9\,\mathrm{rad} \cdot \mathrm{s}^{-1}$
Debye length	$\lambda_D = 2.35 \times 10^{-4}\,\mathrm{m}$
Elastic cross section	$\sigma_e = 2.0 \times 10^{-20}\ \mathrm{m}^2$, $\sigma_i = 7.0 \times 10^{-19}\ \mathrm{m}^2$
Neutral gas	$p = 532\,\mathrm{Pa} (= 4\,\mathrm{Torr})$, $T = 300\,\mathrm{K}$
No. particles per a superparticle	$N_p = 2.0 \times 10^3$ particles
Size of a grid cell	$\Delta x = 1.25 \times 10^{-4}\,\mathrm{m}$
Time step	$\Delta t_e = 1.0 \times 10^{-11}\,\mathrm{s}$, $\Delta t_i = 1.0 \times 10^{-9}\,\mathrm{s}$
Planar probe dimensions	$(2 \times 2 \times 0.5) \times 10^{-3}\,\mathrm{m}$
Computational domain	$(10 \times 10 \times 10) \times 10^{-3}\,\mathrm{m}$

Table 4.7: Plasma parameters and settings of the 3D PIC/MCC model used for the study of plasma sheath of a planar probe in 3D.

Debye length λ_D and mean free paths λ_e, λ_i are exactly the same as in the case which was studied in the previous chapter 4.1.2. By comparing Debye length λ_D and mean free paths λ_e, λ_i, we come to the same conclusion that in the case of both types of charged particles, we can speak of a collisional sheath, where one can observe units of collisions of electrons with neutral particles ($3\lambda_D/\lambda_e \approx 1.8$) and dozens of collisions of positive ions with neutrals ($\lambda_D/\lambda_i \approx 20$).

From the figure 1.3 it can be seen that if the probe radius r_p is at least three times the Debye length λ_D ($r_p > 3\lambda_D$), we can speak of a thin sheath. This is also our studied case, since $r_p = 3.33\lambda_D$. The required inequality is only closely satisfied and we can thus speak of a borderline case that corresponds to a rather thin sheath.

If the mean free path λ is smaller than the probe radius r_p, then there is a situation where we cannot speak of undisturbed plasma at the sheath edge, since the probe, by its presence, blocks a significant amount of the charged particles that would otherwise come to the sheath edge from its direction, which was discussed in the chapter 1.2.2. As a result, a number density profile is established, which decreases towards the probe according to the solution of the diffusion equation. This situation is also our studied case, since both $\lambda_e < r_p$ and $\lambda_i < r_p$.

Let us look at the figures 4.9 and 4.10 where the distribution of electric po-

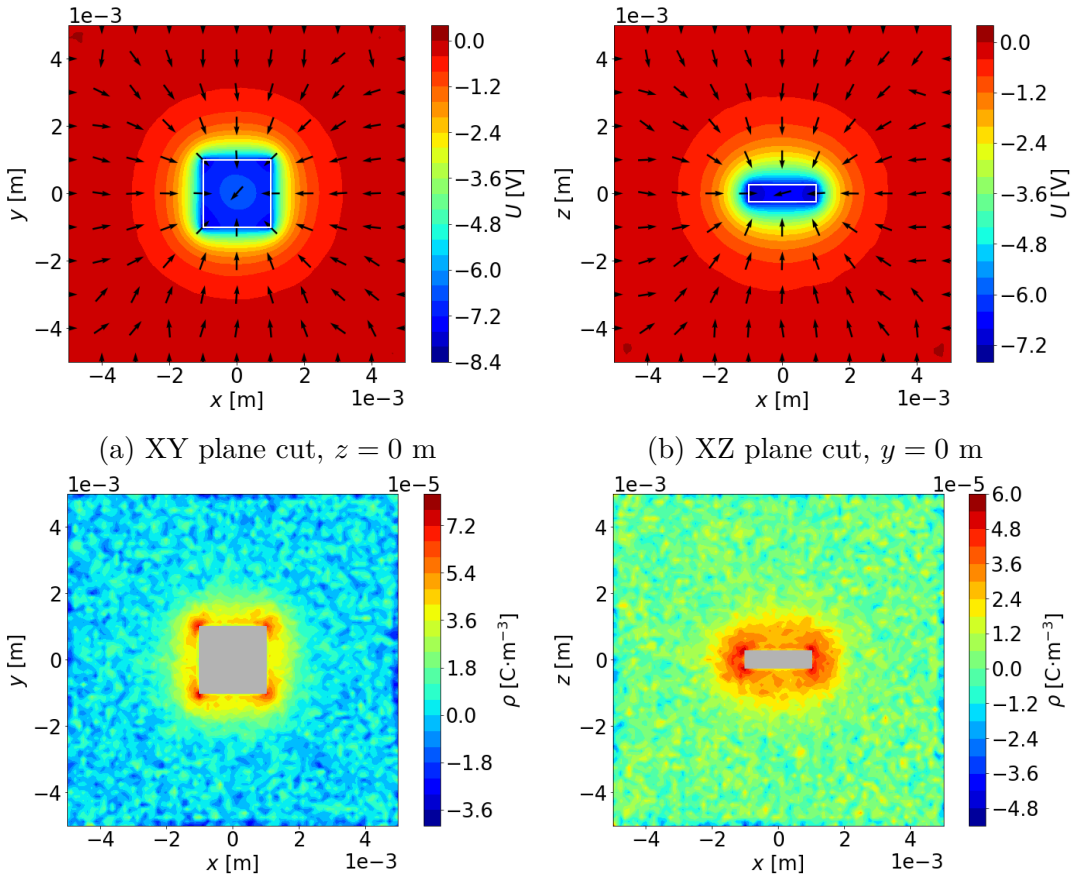

(a) XY plane cut, $z = 0$ m

(b) XZ plane cut, $y = 0$ m

(c) XY plane cut, $z = 0$ m

(d) XZ plane cut, $y = 0$ m

Figure 4.9: Electric potential and space charge density distribution in the surroundings of the negatively biased planar probe modelled in 3D space, $U_p = -7.0$ V.

tential and space charge density in the vicinity of the probe is plotted. It can be observed that the probe potential is not constant across the surface of the probe as it should actually be. It is the effect of the finite cell size of the computational grid that affects the "smearing" of the surface charge density on the probe (see also chapter 3.2.2, figure 3.1). The situation would be better if a finer computational mesh was used, which would, however, lead to much longer calculations. For evaluation purposes, the probe potential is thus reported as the average value of the electrical potential over the probe volume. Further, relatively large spatial fluctuations of the results can be observed, especially of the space charge density. The presented results were obtained by averaging the total number of 200 solution samples, which were taken in the steady state of the calculation and between which 2 000 time iterations took place. The results would be smoother if a higher number of samples were averaged, which would, once again, lead to much longer calculations.

Again, the negative probe potential is shielded at greater distances compared to the positive probe bias, which was also observed in the previous chapter 4.1.2. Also now, the reason is the large thermal energy of the electrons, which weaken the effect of positive ions shielding the negative bias of the probe, and also the need for an electric field in the pre-sheath, which would sufficiently accelerate the

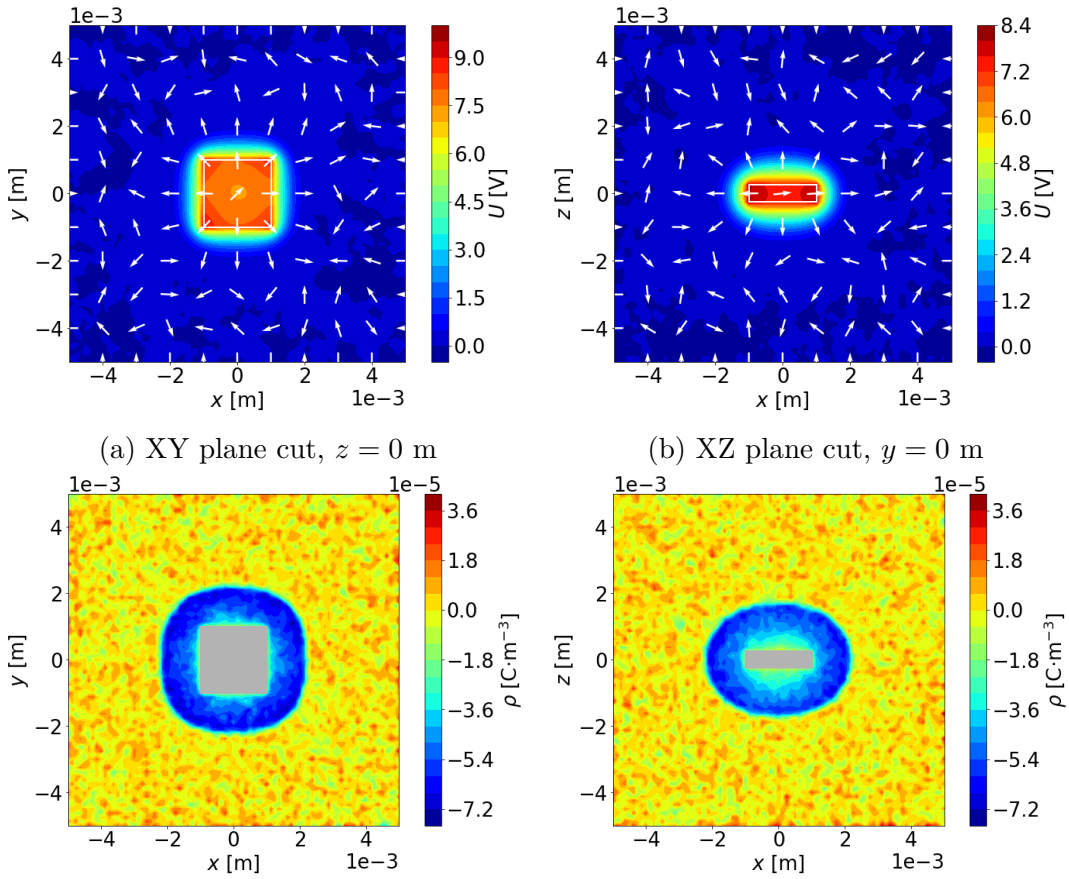

(a) XY plane cut, $z = 0$ m

(b) XZ plane cut, $y = 0$ m

(c) XY plane cut, $z = 0$ m

(d) XZ plane cut, $y = 0$ m

Figure 4.10: Electric potential and space charge density distribution in the surroundings of the negatively biased planar probe modelled in 3D space, $U_p = 8.0$ V.

positive ions so that they could create an area of positive space charge in front of the negatively charged probe. In the figures 4.9c and 4.9d, we see that the positive space charge density in this case accumulates at the edges and corners of the probe, which are the places of strong electric field. In contrast, in the case of a positive bias of the probe, the negative space charge density remains rather at the flat surface of the probe (figures 4.10c and 4.10d). In the case of the positive probe bias, we also observe that the sheath edge is clearly defined – the sheath is formed by a negative charge, and the low thermal energy of positive ions does not allow them to weaken the shielding effect of electrons, as happens in the case of a negative probe bias, when electrons with high thermal energy weaken the shielding effect of the positive ions.

In the figures 4.11 and 4.12, profiles of electric potential, number density and transport coefficients along the z axis, which is perpendicular to the probe surface, are depicted for the negative and positive probe bias cases. It can be observed that the number density of the charged particles decreases towards the surface of the probe just as it was observed in the 1D case in the chapter 4.1.2. Compared to the 1D case, where the decrease was linear, however, we now observe a $1/r$ decrease (r – radial distance from the probe), which corresponds to the solution of the diffusion equation in spherical symmetry. Ideally, the computational domain should be larger, as it can be seen from the figures that its limited size can,

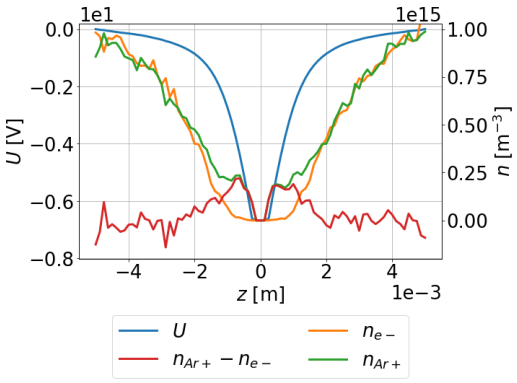

(a) Profiles of electric potential and number density of the charged particles

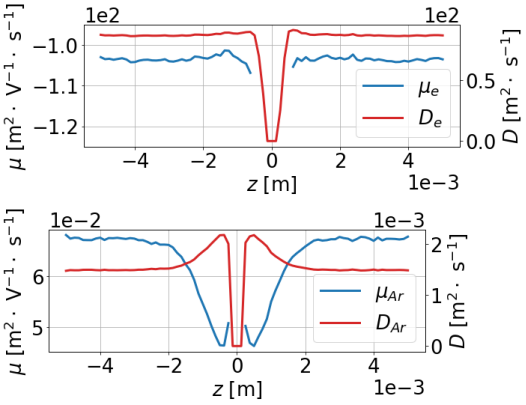

(b) Profiles of transport coefficients

Figure 4.11: Sheath structure in front of the negatively biased planar probe modelled in 3D space, $U_p = -7.0$ V.

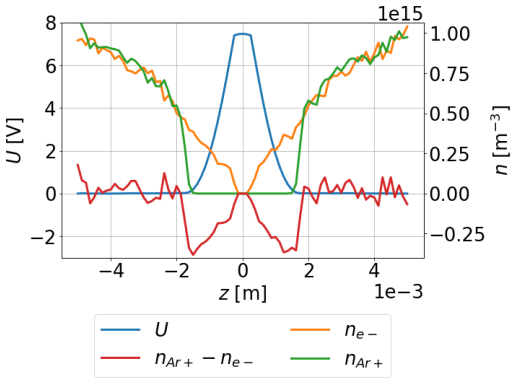

(a) Profiles of electric potential and number density of the charged particles

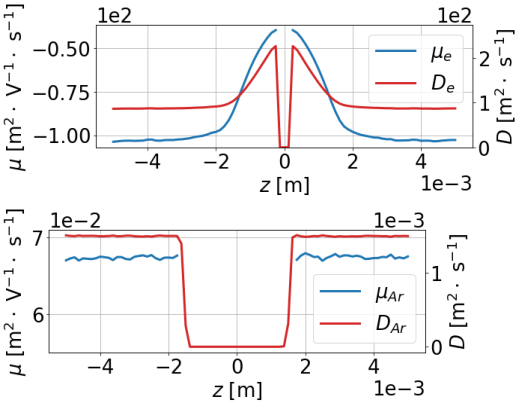

(b) Profiles of transport coefficients

Figure 4.12: Sheath structure in front of the negatively biased planar probe modelled in 3D space, $U_p = 8.0$ V.

through the applied boundary conditions, significantly affect the distribution of the number density of the charged particles and the profile of the electric potential of the negatively biased probe. However, a larger computational domain would mean significantly longer calculations and was therefore not used.

In the case of negative and positive bias of the probe, which are more or less comparable in their absolute value in the figures 4.11a and 4.12a, the sheath, which we consider to be the region in which the quasi-neutrality of the plasma is disturbed, is comparatively large – it extends to a distance of approx. 1.75 mm from the probe, which is approx. $7 \times \lambda_D$. This is perhaps a bit surprising as we would expect a larger sheath in the case of a negative probe bias. In this case, we observe that the positive space charge density is accumulated more near the surface of the probe, in the case of a positive bias of the probe, it is kept more near the sheath edge.

Let us focus more on the figure 4.11a. It corresponds approximately to the situation when the probe is at floating potential – from the IV characteristic, its value was evaluated at $U_f = -6.79$ V (see the table 4.8 below). It can be seen

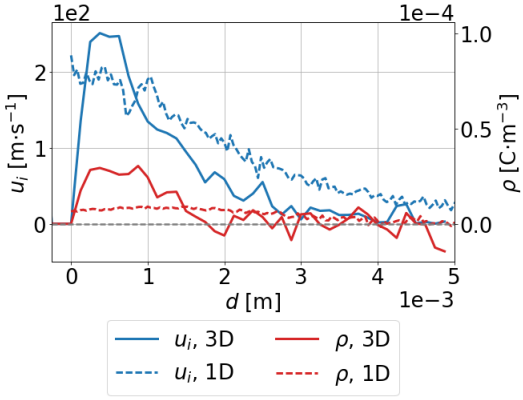

Figure 4.13: Net space charge density and drift velocity of positive ions in front of the planar probe which is approximately at floating potential, comparison of 1D and 3D model results.

that the potential drop in the pre-sheath is approx. $U_{ps} = 1$ V (the sheath, i.e. the region of disturbed quasi-neutrality of the plasma, is approximately 2 mm large; at this distance the potential drop with respect to the undisturbed plasma is just approx. 1 V), which is a value higher than the expected value $U_{ps} = 0.5$ V in the case of a collisionless plasma (according to the equation (1.1.6) assuming an electron temperature of 1 eV). The reason is apparently collisions with neutral particles, which cause a resistance force that the positive ions must overcome so that they can be accelerated to a sufficiently high velocity (= Bohm velocity), which apparently requires a higher potential drop than in the case of a collisionless plasma. Further, for a collisionless plasma, the expected number density of the charged particles at the sheath edge is $n_s = 0.61 n_0$ (according to the equation (1.1.7)), but in the modelled case the number density at the sheath edge is lower, only about $n_s = 0.4 n_0$. It can be due to the diffusion $1/r$ profile of the number density, which is established due to the presence of collisions with neutral particles.

In the figure 4.13, it can be seen how the positive ions before entering the sheath are accelerated by an electric field that penetrates outside the sheath into the pre-sheath. Positive ions upon entering the sheath reach directed velocity of approximately 50 m · s^{-1}, which, as in the 1D case described in the chapter 4.1.2, is less than the theoretical value for collisional plasma: the equation (1.1.13) predicts the value $u_s = 270$ m · s^{-1} and the equation (1.1.14) predicts $u_s = 213$ m · s^{-1}. (These values are obtained for $T_e = 1$ eV and $n_e = 4.0 \times 10^{14}$ m^{-3} which corresponds to the electron number density at the sheath edge.) The reasons for this difference between the calculated and theoretical values are apparently the same as in the 1D case. Further, it can be noticed that the higher values of the directed velocity of ions entering the sheath (both observed and theoretically predicted) compared to the 1D case are apparently related to the higher number density of the charged particles at the sheath edge ($n_s = 4.0 \times 10^{14}$ m^{-3}) than in the 1D case ($n_s = 2.5 \times 10^{14}$ m^{-3}), which leads to a lower value of the Debye length λ_{Ds} at the sheath edge, which is applied in the equations (1.1.13) and (1.1.14), and thus to a higher value of u_s.

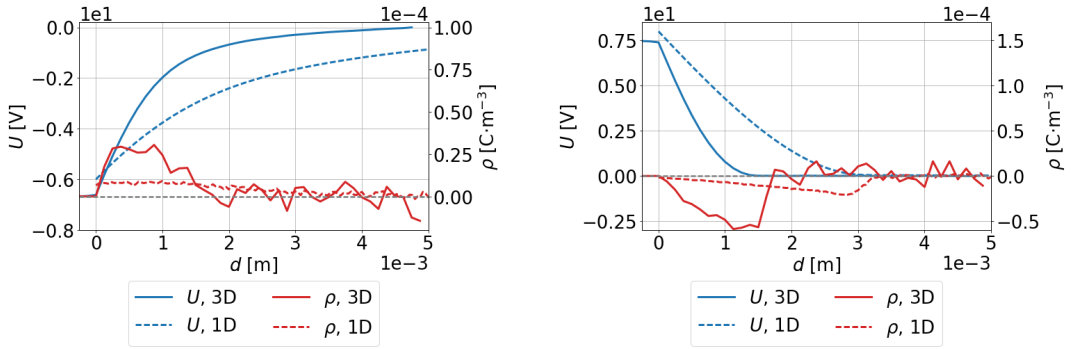

(a) Negatively biased probe

(b) Positively biased probe

Figure 4.14: Comparison of electric potential and space charge density in front of the finite planar probe modelled in the 3D space with infinitely large planar probe described by symmetrical 1D model.

Figure 4.14 shows a comparison of the obtained results with the 1D model of the planar probe that was presented in the chapter 4.1.2. (Note that the probe bias is not exactly the same in both cases.) The 3D model shows that the electric potential is shielded at shorter distances for both positive and negative probe bias compared to the 1D model. Further, it can be seen that the maximum value of the charge density in the sheath is significantly lower in the 1D case than in the 3D model. The reason for these differences is apparently the different value of the number density of charged particles in the area of the sheath edge. In the vicinity of the probe, the number density of charged particles in the 3D model decreases as $1/r$, and a higher number density can be thus observed at the sheath edge than in the case of the 1D model, which shows linear decrease of the number density towards the probe. Another reason is also the choice of the dimensions of the computational domain. In the 1D model, the distance between the probe surface and the undisturbed plasma is equal to 10 mm. In the 3D model, the planar probe is embedded in the center of the computational domain, and the distance between the probe surface and the undisturbed plasma is only about 5 mm. Consequently, in the 3D model, the gradient of the number density between the undisturbed plasma and the probe is higher, and a higher number density of charged particles can be observed in the sheath edge region. It can also be seen that the charge density profile in the sheath has a similar character in both cases, i.e. in the 3D and in the 1D model – in the case of a negative probe bias, it accumulates at the surface of the probe, while in the case of a positive bias, it stays more at the sheath edge.

Now let us take a closer look at the figure 4.15, where the calculated IV characteristic is shown. From the figure 4.15a, we can see that the calculated IV characteristic has a typical course and that the electron current in the region of the negative bias of the probe is higher than what would correspond to the Maxwellian electrons with a temperature of 1 eV. This behavior was also observed in the case of the 1D model of the infinitely large planar probe described in the previous chapter 4.1.2. Figure 4.15b then shows a comparison of the IV characteristics resulting from the 1D and 3D model of the planar probe – the currents on the probe (ion and electron) were renormalized by such a factor that the electron current $j_{e,0}$ on the probe at its zero bias is equal to 1 in both cases.

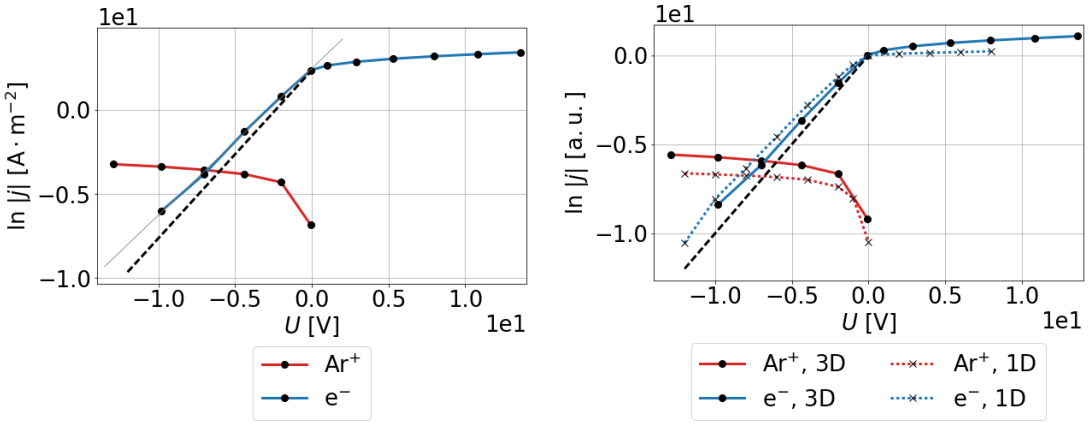

(a) 3D model results.

(b) Comparison between 1D and 3D model results.

Figure 4.15: IV characteristics of the planar probe modelled in 3D space. (Black dashed line marks current density which would correspond to the Maxwellian electrons of temperature $T_e = 11\,605$ K.)

From this graph it can be seen that in the 3D model we observe a steeper drop in the electron current in the area of the negative bias of the probe which leads to a lower electron temperature evaluated from the IV characteristic. We can also observe that in the case of the 3D model, the ratio between ion and electron current is higher than in the 1D model, leading to a higher floating potential U_f than that observed in the 1D model. Further, we observe a faster growth of the electron current in the case of a positive probe bias in the 3D model compared to the 1D model. To a certain extent (at a sufficiently large distance), a 3D model of a planar probe of finite dimensions can be considered a spherical probe, and for it the collisionless theory of probe measurements predicts a linear growth of the electron current with increasing probe bias (see equation (1.2.6)). Electron collisions with neutrals, which perturb the orbital motions of the electrons around the probe, appear to cause the observed current growth to be slower than linear growth; however, the growth is still nonzero (zero growth = constant current is predicted by the collisionless theory for an infinitely large planar probe, see equation (1.2.3)).

Let us discuss plasma parameters which were obtained by evaluation of the calculated IV characteristic and which are listed in the table 4.8, where they are compared with the values relevant to the ideal collisionless case and with the values obtained in the previous chapter 4.1.2 from 1D model of the infinitely large planar probe. At first, let us focus on the value of the electron current at zero bias of the probe and let us compare it with the value predicted by theory according to the equation (1.2.17). We consider the following values: mean free path of electrons $\lambda_e = 3.91 \times 10^{-4}$ m, mean free path of ions $\lambda_i = 1.12 \times 10^{-5}$ m, equivalent probe radius $r_p = 7.82 \times 10^{-4}$ m. Collisionless thermal flux of electrons at the given conditions ($n_e = 1 \times 10^{15}$ m^{-3}, $T_e = 1$ eV) is

$$j_{e,th} = \frac{1}{4} q n_e \left(\frac{8 \mathrm{k_B} T_e}{\pi m} \right)^{\frac{1}{2}} = 26.8 \text{ A} \cdot \text{m}^{-2}.$$

If we insert this value into the equation (1.2.17) for the collisional current density,

Model	$j_{e,0}\,[\mathrm{A\cdot m^{-2}}]$	$T_e\,[\mathrm{K}]$	$n_e\,[\mathrm{m^{-3}}]$	$U_f\,[\mathrm{V}]$	$j_f\,[\mathrm{A\cdot m^{-2}}]$
Collisionless	26.8	11 605	1.00×10^{15}	-4.68	1.52×10^{-1}
PIC/MCC – 3D	10.8	13 294	3.77×10^{14}	-6.79	2.93×10^{-2}
PIC/MCC – 1D	1.33	13 884	4.54×10^{13}	-8.79	1.58×10^{-3}

Table 4.8: Evaluation of the IV characteristics of the planar probe modelled in 3D space and comparison with 1D model results.

we obtain the value

$$j_{e,c} = j_{e,th}\frac{3}{4}\frac{\lambda_e}{r_p} = 10.1\ \mathrm{A\cdot m^{-2}},$$

which is **in very good agreement** with the result of the PIC/MCC model, $j_{e,c} = 10.8\ \mathrm{A\cdot m^{-2}}$ (i.e. only +7 % difference).

Using the standard evaluation of the IV characteristic, we also see that the temperature of the electrons is 14.5 % higher than their temperature in the particle source (11 605 K). A similar difference was also observed in the case of the 1D model of the infinitely large planar probe in the previous chapter. Even in the case of the 3D model, this difference can apparently be explained by the presence of a positive charge in front of the negatively charged probe, the effect of which is not included in the formula (1.2.4) for the evaluation of the electron temperature and which may play a role in the case of the collisional plasma sheath. The standard evaluation of the IV characteristic also shows significantly lower electron number density ($n_e = 3.77\times10^{14}\ \mathrm{m^{-3}}$) than its value in an undisturbed plasma ($n_0 = 1.0\times10^{15}\ \mathrm{m^{-3}}$). This lower value corresponds rather to the value of the electron number density at the sheath edge which is lower than n_0 due to the diffusion profile of the solution between the undisturbed plasma and the sheath edge. If the correct value of the number density of charged particles in the undisturbed plasma should be obtained from the IV characteristic measured under the given conditions, to evaluate the electron current to the probe, which is at the plasma potential, relation (1.2.17) for collisional plasma would have to be used instead of the relation (1.2.5) for collisionless plasma. In the table 4.8, we can also observe that the floating potential U_f is higher in the case of the 3D model of the probe compared to the 1D model, but still lower than the theoretical value for collisionless plasma. The reason for the higher value of U_f compared to the 1D model will probably be a higher ratio of the ion current to the electron current which can probably be attributed to the edge effects that lead to an increased accumulation of positive charge at the edges of the negatively charged probe (see the figures 4.9c and 4.9d) and thus proportionally increase the ion current to the probe.

4.3 Mutual interaction of plasma sheaths in 2D

4.3.1 Electropositive plasma

Results presented in this section were published in the article Hromadka et al. [2014] and were obtained by means of the developed 2D PIC/MCC model which was described in the section 3.1.

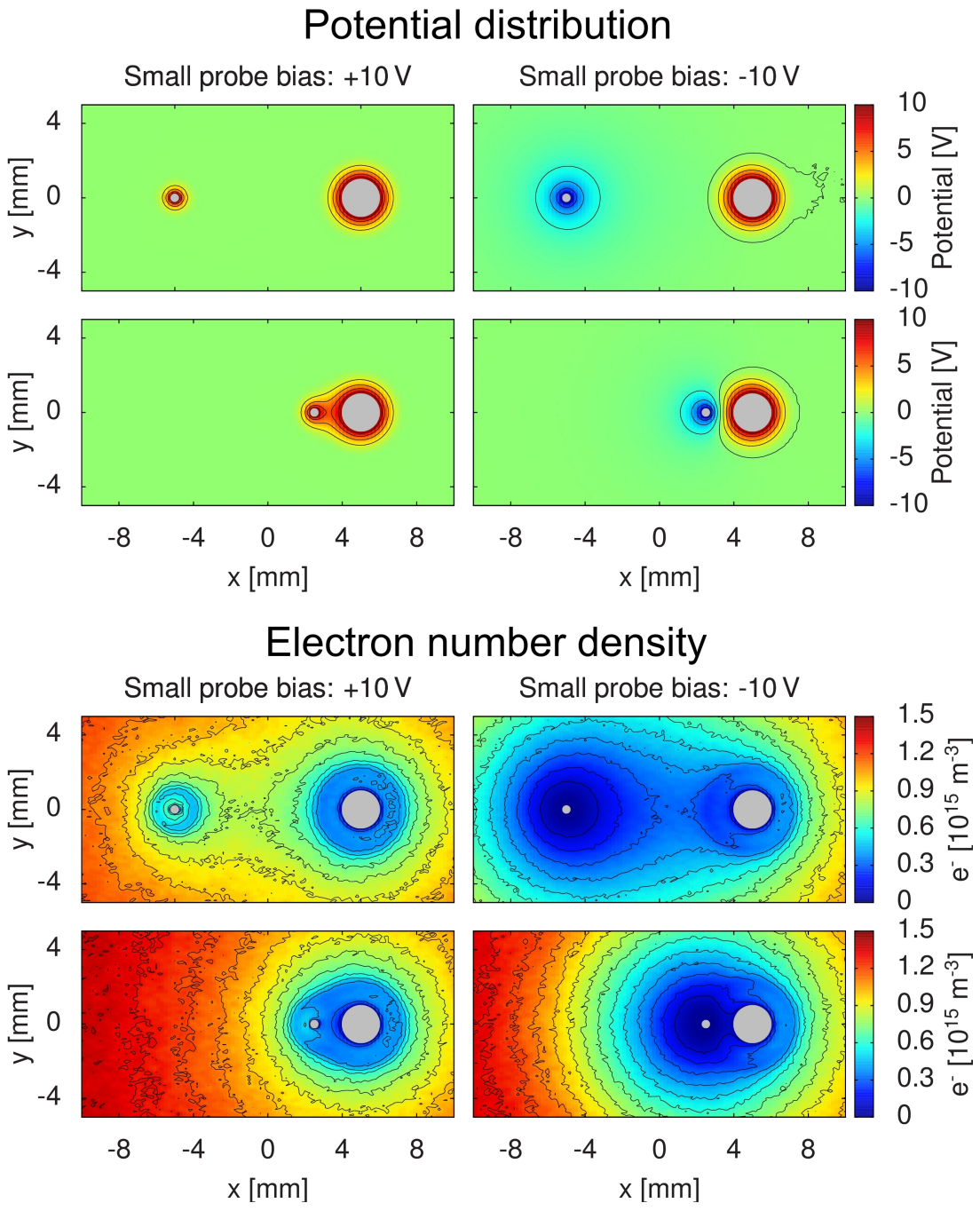

Figure 4.16: Potential distribution and electron number density in the computational domain for two positions and two biases of the smaller probe. The distances between the centers of the probes are 10 mm and 2.5 mm.

Motivation Measurement of plasma parameters by means of cylindrical Langmuir probe is well established technique to determine basic plasma parameters. Classical theories of the probe measurement assume that the probe is immersed into quasi-neutral plasma. However, is it possible to obtain plasma parameters by probe measurement also in areas where quasi-neutrality is broken? Example of such a case might be the situation when the measuring probe is present in the sheath layer of the another one. Further, biased auxiliary probe can be

used to regulate charged particle fluxes and their energy distribution on the other immersed solid [Zeng et al., 1998].

Model settings Electropositive argon plasma of 133 Pa pressure was modelled. Number density of charged particles (electrons and Ar^+ ions) was set to $n_{e,i} = 1.0 \times 10^{15}$ m^{-3}, electron temperature $T_e = 2$ eV. Collisions of electrons e^- with argon neutrals that were considered: elastic scattering, excitation (11.55 eV) and ionization (15.76 eV); collisions of Ar^+ ions with neutrals: elastic scattering and charge transfer. Energy dependance of the particular cross sections were prescribed according to the article Havlickova et al. [2007]. Two different geometry configurations were investigated: a large cylindrical probe with a smaller test cylindrincal probe immersed in its sheath structure and a cylindrical probe near a flat surface with rectangular trench.

Interaction of the two cylindrical probe sheaths Two parallel cylindrical probes were placed at several mutual distances (2.5 mm, 5.0 mm and 10 mm) into the rectangular computational domain of $(5 \times 4) \times 10^{-2}$ m dimensions, the size of the cell of the computational grid was 1×10^{-4} m. The large probe of 1 mm radius was kept at +10 V bias with respect to the plasma potential. To obtain IV characteristic of the smaller probe (0.2 mm radius), its bias was swept between −20 V and +20 V. The 2D PIC/MCC model was used to obtain spatial distribution of the electric potential and number densities of the charged particles in the vicinity of the probes (figure 4.16) and IV characteristic of the smaller probe (figure 4.17). The electric current on the large probe for different biases of the smaller probe was also monitored (figure 4.17).

In the figure 4.16, it can be seen that the presence of the smaller probe decreases the number density of the charged particles in the vicinity of the large probe – since the modelled plasma is collisional (Debye length 0.33 mm, electron mean free path 0.74 mm), diffusion logarithmic profile of the number density is created in the vicinity of the both cylindrical probes. The figure 4.16 also shows that the potential of the negatively biased smaller probe is shielded off at longer distances and thus, the negative probe affects larger area than the positive one – the reason is large enough thermal energy of electrons which are able to overcome potential barrier created by the negatively biased probe, get into its close vicinity and weaken the shielding electric field of the positive Ar^+ ions which are cumulated at the probe.

In the table 4.9, plasma parameters obtained by the standard analysis of the IV characteristic of the smaller probe (figure 4.17) are listed for different mutual distances of the probes. It can be seen that even in the case when the large probe is not present in the computational domain, we observe a lower evaluated number density of the charged particles ($n_e = 5.90 \times 10^{14}$ m^{-3}) than what is in the particle source ($n_e = 1.0 \times 10^{15}$ m^{-3}). A similar observation was made in the previous chapters when we examined a planar probe (see e.g. the table 4.8). The reason for this difference is that we use the collisionless plasma theory to evaluate the IV characteristic, which is not suitable, because in the case studied, collisions dominate and manifest themselves by creating a logarithmic diffusion profile of the number density of the charged particles in the vicinity of the cylindrical probe. By applying the collisionless plasma theory, we evaluate rather the number density of

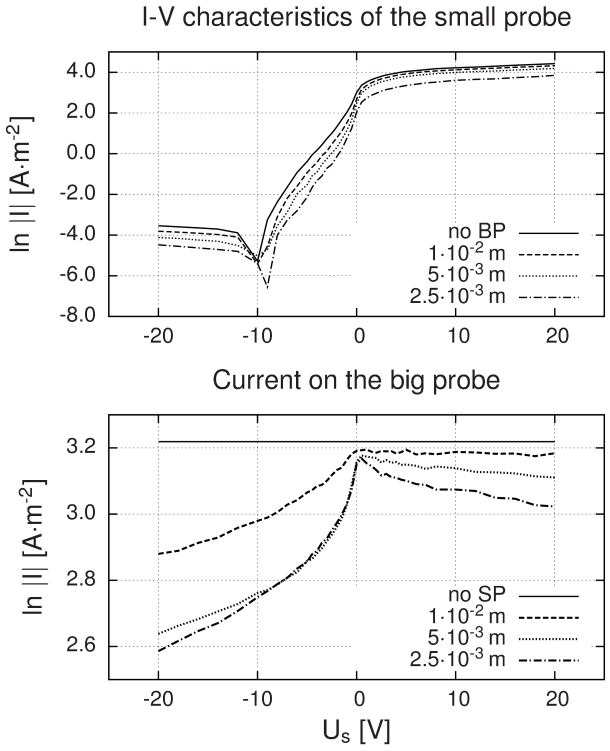

Figure 4.17: IV characteristics of the smaller cylindrical probe for different distances from the large probe and the current collected by the large probe.

Distance [mm]	T_e [K]	n_e [10^{14} m^{-3}]
No large probe	18 960	5.90
10.0	18 280	4.36
5.0	17 570	3.58
1.0	17 120	2.37

Table 4.9: Analysis of the IV characteristics of the smaller probe.

particles at the sheath edge, which, due to the presence of collisions, is lower than in the undisturbed plasma in the particle source. If the large probe is present in the computational area, then it can be seen that for a closer mutual distance between the probes, the observed current and the evaluated number density of the particles are lower. This trend is in agreement with the calculated number density distribution which is decreasing towards the large probe according to the logarithmic diffusion profile.

Even in the case when the large probe is not present in the computational domain, the evaluation of the IV characteristic yields a lower electron temperature ($T_e = 18\,960$ K) than that in the particle source ($T_e = 23\,210$ K $= 2$ eV). This is the opposite observation to the case of the planar probe studied in the previous chapters (see e.g. the table 4.8). The reason is apparently that in the currently studied case of cylindrical probes, inelastic collisions (excitation, ionization) were taken into account for the electrons which cool them when they move in the computational domain. If a large probe is present in the region, then we see that the electron temperature evaluated from the IV characteristic is lower for a closer

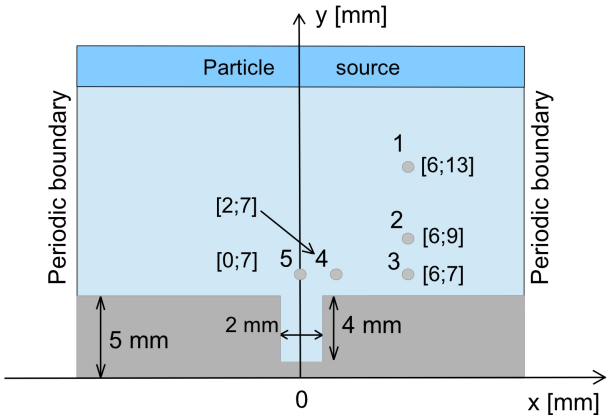

Figure 4.18: 2D model of the flat surface with a rectangular trench and positions 1 – 5 of the cylindrical probe.

mutual distance between the probes. It is the effect of the strong electric field between the probes: high energetic electrons are rather attracted by the positive large probe in the case of negative smaller probe which leads to the lower electron current on the smaller probe, greater derivative of the current and consequently to the lower evaluated electron temperature.

The figure 4.17 shows that the electric current (formed mainly by electrons) on the positive large probe decreases for both positive and negative bias of the smaller probe; this effect is more significant for closer mutual distance of the probes. Positive smaller probe apparently collects part of the electrons which would otherwise end up at the positive large probe. On the contrary, negative smaller probe repels also those electrons which are heading towards the positive large probe.

Interaction of the cylindrical probe sheath with the sheath of uneven surface A cylindrical Langmuir probe of 0.2 mm radius was placed at several positions near a flat surface with a rectangular trench (figure 4.18). The question is whether the presence of the flat surface and of the trench, in particular, affects the IV characteristic measured by the probe at these positions. Bias of the uneven surface was kept at 0 V with respect to the plasma potential, bias of the probe was swept between −20 V and +20 V.

IV characteristics in the figure 4.19 show that the electric current on the probe decreases with the decreasing distance between the probe and the flat surface. It is due to the linearly decreasing diffusion profile of the charged particles number density towards the surface. On the other hand, no significant effect is observed when the probe approaches the trench along the flat surface. Presence of the trench in the flat surface does not influence the sheath structure of the flat surface much as can be seen in the figure 4.20. In the investigated case, sheath surrounding the cylindrical probe is of comparable size with the trench. More significant effect of the trench on the calculated IV characteristics would be probably observed if the trench had larger dimensions than the sheath.

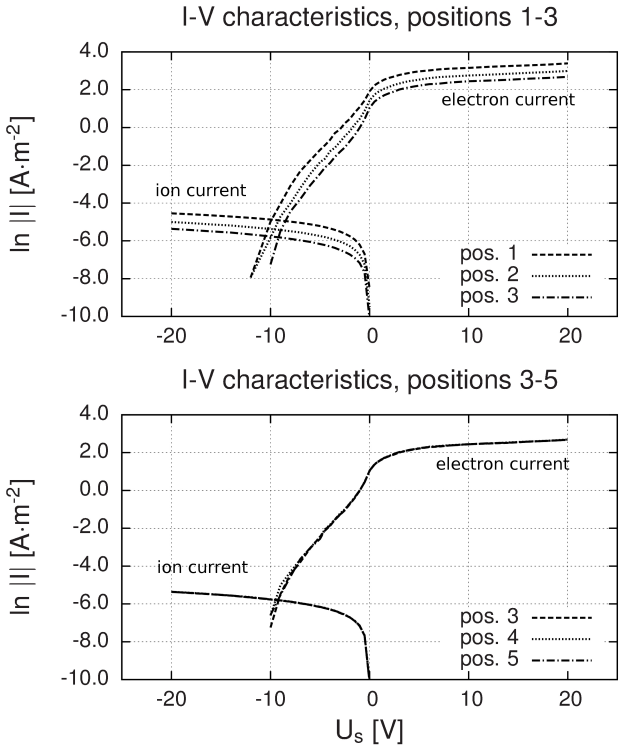

Figure 4.19: IV characteristics of the cylindrical probe near the uneven surface at different positions.

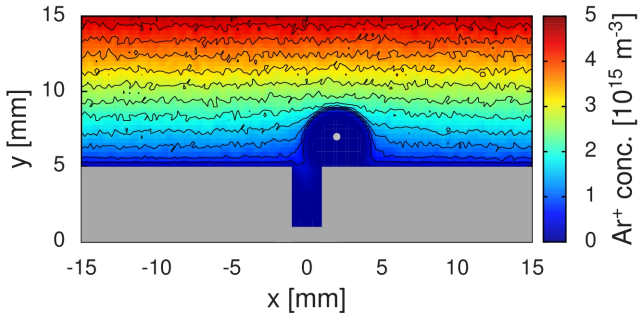

Figure 4.20: Number density of Ar^+ ions for +10 V bias of the cylindrical probe and position no. 4.

Summary Mutual interaction of the plasma sheaths has significant influence on the fluxes of the charged particles on the solids immersed in plasma. The 2D PIC/MCC model is able to provide trends of the observed phenomena; however, for quantitative comparison, 3D model is needed because interpretation of the 2D model results is problematic.

4.3.2 Electronegative plasma

Results that are presented in this section were published in the article Hromadka et al. [2015] and were obtained by means of the developed 2D PIC/MCC model

which was described in the section 3.1.

Motivation Electronegative plasma, in which part of the negative electric charge is formed by negative ions, is also widely used in different plasma-assisted techniques of material surface treatment (e.g. surface etching, ion implantation, thin film deposition). Presence of negative ions in the plasma significantly affects its response to external electromagnetic fields and also its chemical activity. This strongly depends on the ratio between number density of electrons (n_e) and number density of negative ions (n_-). For this reason, we define plasma electronegativity α as

$$\alpha = \frac{n_-}{n_- + n_e}.$$

The most common electronegative plasmas used in semiconductor manufacturing are plasmas in gases which contain e.g. H_2, F_2, O_2, Cl_2, SF_6. Electronegativity can vary in a wide range from tenths of a per cent up to almost 100%.

Theory of electronegative plasma sheath has been adressed in numerous works so far, e.g. Swift and Schwar [1969], Braithwaite and Allen [1988], Riemann [1995]. In this section, 2D PIC/MCC study of plasma sheath of a single cylindrical Langmuir probe in argon plasma with admixture of negative oxygen ions O^- is studied. Further, mutual interaction of multiple plasma sheaths in this kind of plasma is presented (similar study as in the section 4.3.1 for electropositive plasma).

Model settings The object of the presented study is an artificial mixture of positive argon ions Ar^+, electrons e^- and negative oxygen ions O^- with neutral argon gas Ar in the background. It is a very simple model of Ar/O_2 plasma which contains much more charged species in reality. In this way, the model remained as simple as possible and still able to show the effect negative O^- ions on the sheath structures. The computational study was done by means of 2D PIC/MCC model which is described in more detail in the section 3.1. In the table 4.10, there are values of the model parameters which were used in the presented study. The model resolved trajectories of 2×10^6 charged particles in total. Typically, it took 1.5×10^5 iterations of the main time cycle to reach the steady state and additional 1×10^5 iterations to get sufficiently smooth solution. The following scattering processes of the charged particles with argon neutrals were taken into account: electron collisions [Bogaerts et al., 1999] – elastic scattering, excitation (11.55 eV) and ionization (15.76 eV) ; Ar^+ collisions [Phelps, 2013] – elastic scattering and charge transfer; O^- collisions [Vahedi and Surendra, 1995] – elastic scattering.

Sheath of a single probe in the electronegative plasma Sheath structure in the vicinity of a biased cylindrical probe of 0.2 mm radius was studied for two different values of its bias U_B with respect to the plasma potential: $U_B = \{-10, +10\}$ V. The study was done for plasma of three different electronegativities: $\alpha = \{10\%, 50\%, 90\%\}$. In the figure 4.21, profile of number density of the charged particles for $\alpha = 50\%$ case is presented. (Note that only the detail of the sheath region is captured in the figure. The electronegativity of 50% applies only to the bulk plasma which is at a distance of 20 mm from the probe. At the sheath edge, i.e. 1.5 mm or 5 mm from the probe, the electronegativity is

Model parameter	Value
Computational domain	$(4 \times 4) \times 10^{-2}\,\mathrm{m}$
Computational mesh	400×400 nodes
Pressure	$133\,\mathrm{Pa}$
Plasma density	$1.59 \times 10^{15}\,\mathrm{m}^{-3}$
Plasma electronegativity	10%, 50%, 90%
Temperature (e^-, Ar^+, O^-)	$23\,600\,\mathrm{K}$, $300\,\mathrm{K}$, $300\,\mathrm{K}$
Time steps (e^-, Ar^+, O^-)	$10^{-11}\,\mathrm{s}$, $10^{-8}\,\mathrm{s}$, $10^{-8}\,\mathrm{s}$
Probe radius (smaller, large)	$0.2\,\mathrm{mm}$, $1.0\,\mathrm{mm}$

Table 4.10: 2D PIC/MCC model parameters applied in the study of electronegative plasma sheaths.

significantly lower.) Profiles of net space charge density and electric field in the case of all considered plasma electronegativities are also given in the figure 4.21.

In the case of $\alpha = 50\%$ and $U_B = +10\,\mathrm{V}$, shielding of the external probe potential is ensured rather by e^- than O^- ions. It can be seen that number density of O^- ions is lower than density of e^- also just behind the sheath edge. In the case of negative probe bias $U_B = -10\,\mathrm{V}$, positive space charge of Ar^+ ions which shields off the probe bias originates; however, this region is infiltrated by those electrons which have sufficiently high thermal energy and thus, they are able to overcome repelling force of the negatively biased probe. On the contrary, O^- ions stay further from the non-quasineutral sheath, their thermal energy is not high enough to penetrate the sheath. These observations are well in agreement with the article Franklin and Snell [1992] where it is stated that negative ions are confined to bulk of plasma by the space charge fields caused by electrons with their lighter mass and higher thermal energy. The presented observation is also in accordance with the theory presented in the chapter 1.1.2 where for $\gamma = T_e/T_- = 78.7$ and the same ratio of electrons and negative ions we observe a very low electronegativity at the sheath edge (see the figure 1.2).

The figure 4.21 shows that the distribution of the net space charge density around the probe varies with changing electronegativity. It can be seen that at low electronegativity, for both positive and negative probe biases, the charge density accumulates closer to the probe, while at higher electronegativity, the charge density profile is more flat and the region of non-zero charge density extends to a greater distance from the probe. With a negative bias, this area is generally larger than with the same amount of positive probe bias. The explanation for the different charge density profile with varying electronegativity can be as follows:

- With a positive bias and low electronegativity, the potential of the probe is mostly shielded by electrons. They have a significantly higher thermal energy compared to positive ions and it is not difficult for them to break out of the quasi-neutral plasma and create a region of negative charge with a relatively high density and low thickness in front of the probe – electrons do not need pre-sheath in which they would be accelerated. This can be seen in the left part of the figure 4.22 where for a positively charged smaller probe we observe that the region of non-zero electric field (i.e. the directed vectors of the electric field in the figure at bottom) corresponds to the region of non-zero space charge density and the electric field does not penetrate

the quasi-neutral plasma. At high electronegativity, negative ions must participate in the shielding of the positive potential of the probe. However, these have an energy comparable to the thermal energy of positive ions, and therefore in this case a pre-sheath must be formed, where the negative ions would be accelerated by the electric field so that they could leave the quasi-neutral plasma and create a region of negative charge in front of the probe (the existence of a pre-sheath at a higher electronegativity is indicated by the right part of the figure 4.22 where for the smaller probe it can be observed that the region of non-zero electric field, i.e. the directed vectors, is larger than the region of non-zero charge density). Even so, the negative ions are not able to leave the quasi-neutral plasma in large quantities – the negative charge density in the sheath is thus lower and potential shielding occurs at greater distances.

- In the case of negative bias of the probe and low electronegativity, the ions must be accelerated to a very high velocity in the pre-sheath so that they are able to overcome the thermal velocity of the electrons and create a region of positive charge in front of the probe. The potential drop in the pre-sheath is relatively high and the pre-sheath extends a large distance from the probe (see the left part of the figure 4.22 where for a smaller, negatively charged probe, the electric field extends into a much larger area than the non-zero charge density area). But the electrons have a lot of thermal energy and thanks to it they can get relatively close to the probe, into the region of the negative field of the probe. As a result, an area of positive charge density is formed only in the immediate vicinity of the probe. At a higher electronegativity, according to the theory (the chapter 1.1.2), the required directed velocity of positive ions upon entering the sheath is lower than the Bohm velocity. In this case, such a high potential drop in the pre-sheath is not necessary and it does not have to extend over a long distance (see the right part of the figure 4.22 where we observe for a smaller, negatively charged probe that the region of the non-zero electric field approximately corresponds to the region of the non-zero space charge density). The situation is thus ultimately analogous to the case of a positively charged probe at a higher electronegativity (where, of course, the positive and negative ions have reversed roles), where the non-zero charge density also has a flat profile. As a result, the region of non-zero charge density is larger than in the case of low electronegativity.

Interaction of plasma sheaths in electronegative plasma Interaction of plasma sheaths of a smaller cylindrical probe (0.2 mm radius) and a large probe (1.0 mm radius) was studied. The study was done for one particular bias of the large probe, $U_{bp} = +10$ V. Parameters that were varied: distance between the probes $d = \{2.5, 10\}$ mm, bias of the smaller probe $U_{sp} = \{+10, -10\}$ V and plasma electronegativity $\alpha = \{10\%, 90\%\}$. Interaction of the sheaths is depicted in the figures 4.22 and 4.23 in terms of net space charge density and electric field distribution around the probes for all of the studied variants. The figure 4.22 presents results for positive bias of the smaller probe $U_{sp} = +10$ V, whereas the figure 4.23 for its negative bias $U_{sp} = -10$ V.

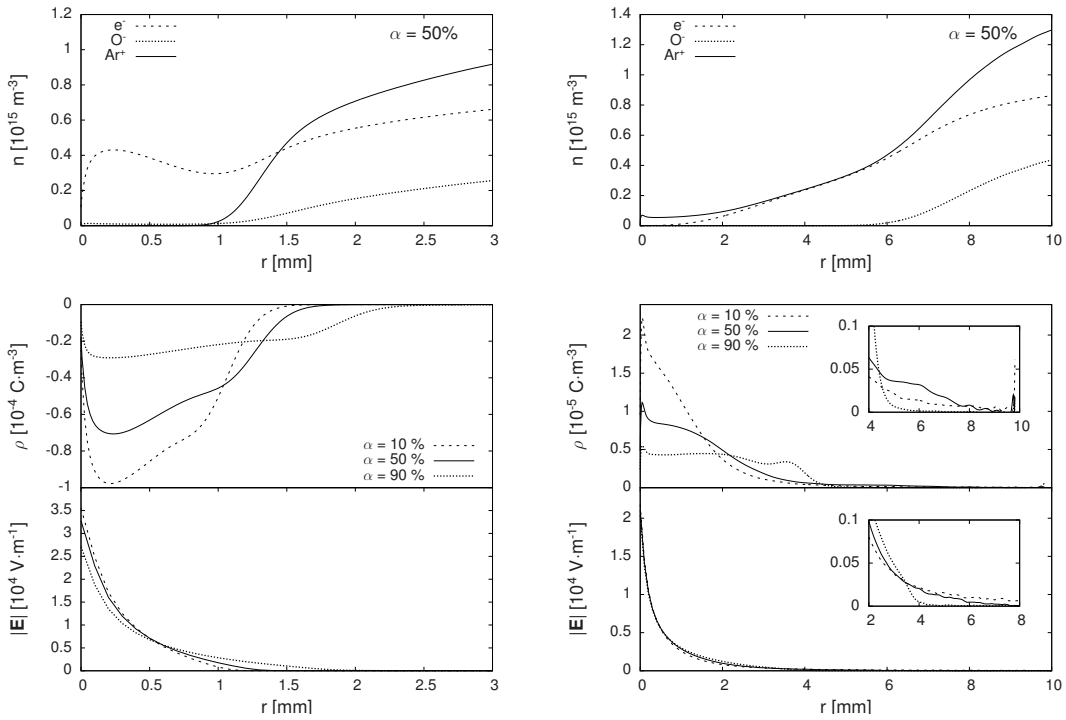

(a) $U_b = +10\,\mathrm{V}$ (b) $U_b = -10\,\mathrm{V}$

Figure 4.21: Number density of charged particles, net charge density and electric field intensity in the sheath structure around a single cylindrical probe for various voltage biases U_b and electronegativities α of the studied plasma. The probe is located on the left-hand side of the graphs, radial distance from the surface of the probe is depicted on the horizontal axis.

Positive bias of the smaller probe $U_{sp} = +10$ V: In case of large mutual distance of the probes ($d = 10$ mm), sheath structures do not significantly interact. External potentials of the probes are well shielded out by electrons and they do not penetrate far from the probes. If the distance between the probes ($d = 2.5$ mm) is lower than the characteristic size of the sheaths, one large sheath structure which is the sum of the particular sheaths is created. In general, sheaths do not interact unless they start to spatially overlap. Mutual interaction of the sheaths has quite similar character for different electronegativities; for higher electronegativity, sheaths are only spatially larger.

Negative bias of the smaller probe $U_{sp} = -10$ V: Positive Ar^+ ions shield the external potential of the small probe and area of positive space charge is created in its surroundings. In the case of low electronegativity, electric field penetrates quite far from the smaller probe; even beyond the area of non-zero space charge. Positive ions have to be accelerated first in the pre-sheath region to be able to overcome high thermal velocity of electrons in order to be able to create positive space charge area in the probe surroundings (Bohm condition). As a result, electric field of the smaller probe repels electrons which shield the positive potential of the large probe even in case of large distance ($d = 10\,\mathrm{mm}$) between the probes. This effect is stronger for closer distance between the probes. In the case of high electronegativity, electric field of the smaller probe does not

penetrate so far and areas of non-zero space charge and non-zero electric field in the probe surroundings are almost identical. As there are rather O^- ions of thermal energy which is comparable to that of Ar^+ ions than electrons, Ar^+ ions does not have to be accelerated so much before entering the sheath and presheath region does not need to extend so far from the probe. The sheath of the positive large probe is enlarged for higher α. However, the interaction of the probes can be classiffied as less intensive in the case of high electronegativy, mainly due to the lower dimension of the smaller probe pre-sheath.

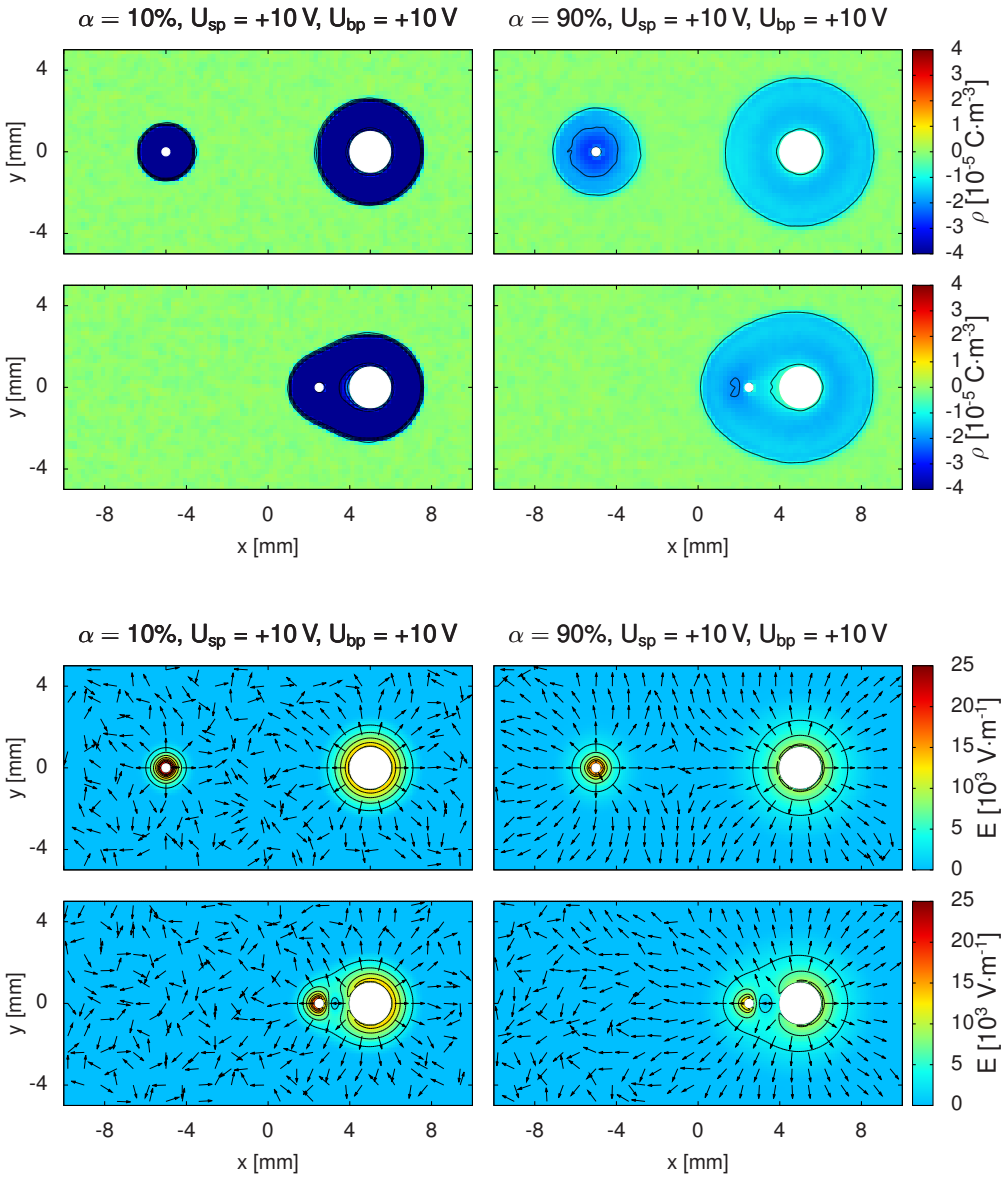

Figure 4.22: Net charge density and electric field intensity in the sheath structure around two cylindrical probes for various positions of the smaller probe with bias $U_{sp} = \mathbf{+10\ V}$ and various electronegativities of the studied plasma. Solid lines mark isolines of charge density with $1 \cdot 10^{-5}$ C $\cdot$ m^{-3} step and isolines of electric field intensity with $3 \cdot 10^3$ V $\cdot$ m^{-1} step. Big probe bias $U_{bp} = +10$ V.

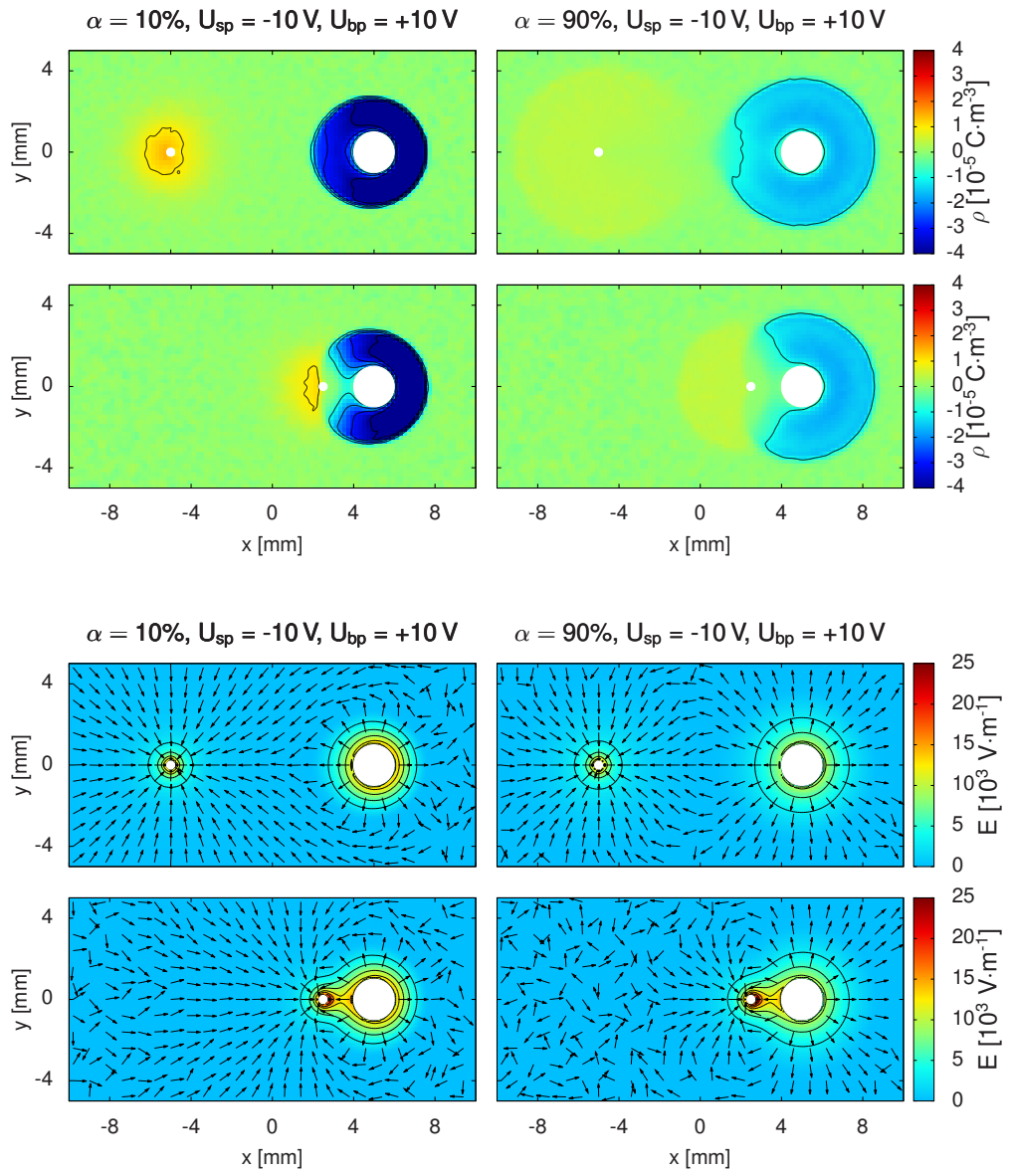

Figure 4.23: Net charge density and electric field intensity in the sheath structure around two cylindrical probes for various positions of the smaller probe with bias $U_{sp} = -10$ **V** and various electronegativities of studied plasma. Solid lines mark isolines of charge density with $1 \cdot 10^{-5}$ C $\cdot$ m^{-3} step and isolines of electric field intensity with $3 \cdot 10^{3}$ V $\cdot$ m^{-1} step. Big probe bias $U_{bp} = +10$ V.

Effect of the presence of the negatively biased smaller probe ($U_{sp} = -10$ V) on the sheath structure of the positively biased large probe ($U_{bp} = +10$ V) is documented also in the figure 4.24 where flux of negatively charged particles on the large probe is depicted for different conditions. Reduction of the flux from direction of the smaller probe position ($\psi = \pi$) can be observed for all studied variants. The reason is the electric field in the pre-sheath of the smaller probe which repels the negative particles. The decrease of flux is more significant for closer distance between the probes and it is also more significant for O^- ions than for electrons which have higher thermal energy and thus, they are able to better overcome repelling field of the smaller probe.

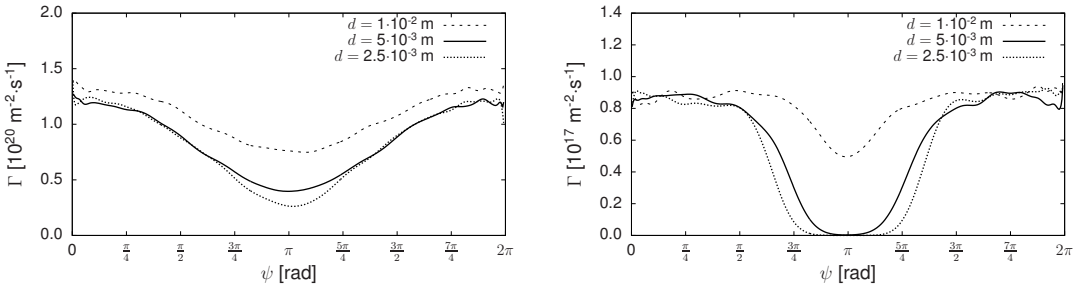

(a) Flux of electrons, $\alpha = 10\%$ (b) Flux of O^- ions, $\alpha = 90\%$

Figure 4.24: Fluxes of negatively charged particles on the large probe ($U_{bp} = +10$ V) for different values of plasma electronegativity α and positions of the smaller probe ($U_{sp} = -10$ V).

Summary The study of a single probe sheath in electronegative plasma proved that negative O^- ions stay rather in a bulk plasma while electrons with higher mobility, higher thermal energy and lower values of elastic scattering cross section ensure shielding out of the external potentials. The study of mutual interaction of multiple plasma sheaths showed that even low electric field in the pre-sheath of a smaller probe can considerably affect fluxes of the charged particles on the large probe placed in its surroundings.

4.4 Mutual interaction of plasma sheaths in 3D

The results presented in this chapter follow the 2D study of the interaction of plasma sheaths formed around two cylindrical probes, which was presented in the chapter 4.3, and extend the study of this issue to 3D space. Here, two planar probes of finite dimensions are studied – a larger probe whose dimensions are identical to the planar probe studied in the chapter 4.2 and a smaller probe whose dimensions in the x and y directions are half that. The geometry of the probes, including the used computational domain, can be seen in the figure 4.25, which also presents two relative positions of the probes for which the study was carried out – i.e. for mutual distances of $d = 5.0$ mm and $d = 2.5$ mm in the normal direction to the planes of the probes. The choice of the dimensions of the probes is a little artificial and is limited by the chosen step of the computational grid – in fact, the thickness of the probes in the z-axis should be much smaller, for which it would be necessary to choose a smaller step of the computational grid, which would lead to more time-consuming calculations. As a result, for the smaller probe, its dimensions are comparable in all directions and even at a relatively close distance it can be thought of as a spherical probe.

The study was performed by placing the smaller probe in two different positions relative to the large probe for which the IV characteristic was calculated in each of these configurations. For each bias of the large probe, the potential of the smaller probe was adjusted to equalize the flows of positively and negatively charged particles on it, i.e. the smaller probe was assigned a voltage corresponding to the floating potential under the given situation. In this way, it was possible to find out what influence the presence of a smaller conductive object in the vicin-

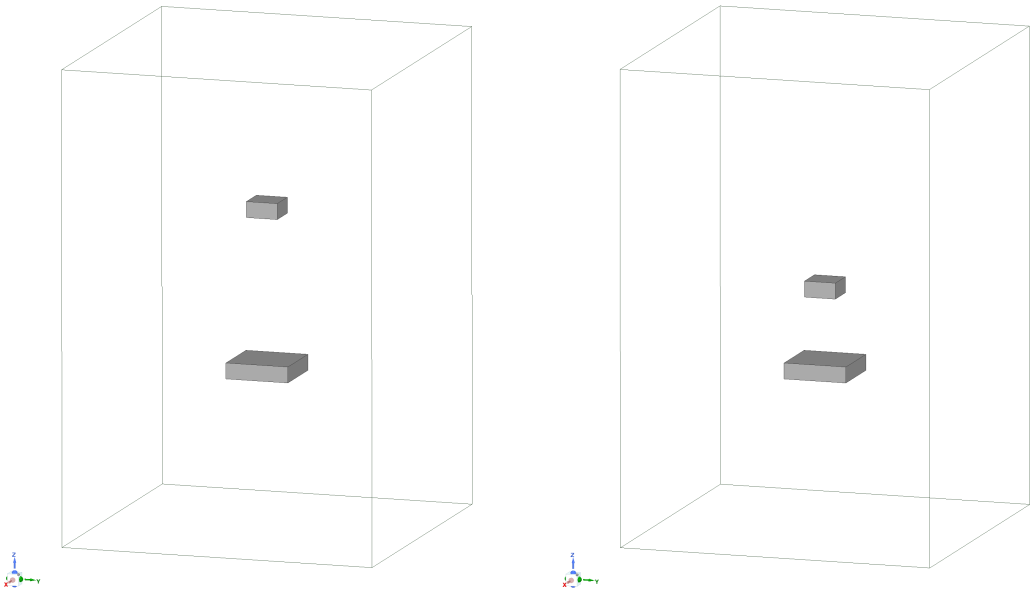

(a) Distance $d = 5.0$ mm (b) Distance $d = 2.5$ mm

Figure 4.25: Geometry of two interacting planar probes and 3D computational domain.

ity of the planar probe has on its IV characteristic and on the plasma parameters derived from it.

The calculations were performed for an electropositive argon plasma with the same properties as those considered in the chapter 4.2. The plasma parameters used and the settings of the 3D PIC/MCC model are summarized in the table 4.11. By modeling a plasma with the same parameters, the mutual relations between the Debye length ($\lambda_D = 2.35 \times 10^{-4}$ m), the mean free path of electrons ($\lambda_e = 3.91 \times 10^{-4}$ m), the mean free path of ions ($\lambda_i = 1.12 \times 10^{-5}$ m) and the equivalent radius of the large probe ($r_{LP} = 7.82 \times 10^{-4}$ m) did not change. So we can still talk about a collisional sheath, both in the case of electrons and ions, and also about a rather thin sheath around the large probe (for more detail, see the discussion of the characteristic lengths in the chapter 4.2). The discussion of the characteristic lengths now needs to be supplemented with the relationship between the equivalent radius of the smaller probe, which is $r_{SP} = 4.92 \times 10^{-4}$ m, and between the Debye length λ_D and the mean free paths of the charged particles λ_e, λ_i.

We can see that $r_{SP}/\lambda_D = 2.09$ applies to the smaller probe and according to the figure 1.3, it is necessary to consider its sheath rather as a thick sheath. In the case of the relation of the equivalent radius of the smaller probe to the mean free paths of the charged particles, the same applies as in the case of the large probe: $\lambda_i < r_{SP}$ and $\lambda_e < r_{SP}$. So even in this case, we have to consider that the smaller probe can block a significant part of the particles that would come to the sheath edge and we cannot thus talk about an undisturbed plasma here. It should be noted that the inequality $\lambda_e < r_{SP}$ is only partially satisfied compared to the similar inequality for ions and may be the reason for the different behavior of electrons and ions in the vicinity of the smaller probe.

In the 4.2 chapter, it was shown that at the negative probe bias of $U_p = -7$ V,

Temperature	$T_e = 11\,600\,\mathrm{K}$ $(= 1\,\mathrm{eV})$, $T_i = 300\,\mathrm{K}$
Number density	$n_e = n_i = 10^{15}\,\mathrm{m}^{-3}$
Plasma frequency	$\omega_p = 1.78 \times 10^9\,\mathrm{rad} \cdot \mathrm{s}^{-1}$
Debye length	$\lambda_D = 2.35 \times 10^{-4}\,\mathrm{m}$
Elastic cross section	$\sigma_e = 2.0 \times 10^{-20}\ \mathrm{m}^2$, $\sigma_i = 7.0 \times 10^{-19}\ \mathrm{m}^2$
Neutral gas	$p = 532\,\mathrm{Pa} (= 4\,\mathrm{Torr})$, $T = 300\,\mathrm{K}$
No. particles per a superparticle	$N_p = 2.0 \times 10^3$ particles
Size of a grid cell	$\Delta x = 1.25 \times 10^{-4}\,\mathrm{m}$
Time step	$\Delta t_e = 1.0 \times 10^{-11}\,\mathrm{s}$, $\Delta t_i = 1.0 \times 10^{-9}\,\mathrm{s}$
Large probe dimensions	$(2 \times 2 \times 0.5) \times 10^{-3}\,\mathrm{m}$
Smaller probe dimensions	$(1 \times 1 \times 0.5) \times 10^{-3}\,\mathrm{m}$
Computational domain	$(10 \times 10 \times 15) \times 10^{-3}\,\mathrm{m}$

Table 4.11: Plasma parameters and settings of the 3D PIC/MCC model used for the study of plasma sheath interaction of two planar probes in 3D.

which is approximately equivalent to the floating potential, the sheath size is approximately $s = 1.75$ mm (see the figure 4.11). We therefore expect that when the probes are at a mutual distance of $d = 5.0$ mm, the sheaths around the probes will not interact, while at a closer distance of $d = 2.5$ mm they will.

Let us discuss results presented in the figures 4.26, 4.27, 4.28, 4.29, 4.30 and 4.31 which show the sheath structures for different mutual positions of both probes and for different biases (positive and negative) of the large probe. The smaller probe is kept at floating potential in each situation, meaning it is negatively biased with respect to the plasma potential. As observed in the previous chapters, the electric field of the negatively charged probe is not completely attenuated in the sheath region (that is, the region where the quasi-neutrality of the plasma is disturbed) and partially penetrates into the pre-sheath where it accelerates the positive ions so that they are able to create a region with positive charge density in front of the probe. As a result, the electric field of the negatively charged smaller probe reaches a relatively large distance and can be seen to affect, albeit slightly, the sheath of the large probe (both positively and negatively charged) even at a large mutual distance of $d = 5.0$ mm. Through this electric field, the smaller probe either takes away the positive charge density from the negatively charged large probe, or begins to repel the negative charge density from the positively charged large probe.

If the (negatively charged) smaller probe approaches a negatively charged large probe, the positive charge densities attached to the surface of the individual probes begin to repel each other and the charge density in the space between the probes is neutralized. As a result, the electric potential in the region between the probes will decrease. If the smaller probe were to get even closer, the array of probes would begin to behave as a single structure manifesting outwardly as a single resulting shielding layer. If the (negatively charged) smaller probe approaches a positively charged large probe, then also in this case the charge density in the space between the probes is neutralized – the positive charge density of the smaller probe is neutralized with the negative charge density of the large probe and as a result, high intensity electric field sets up between the probes.

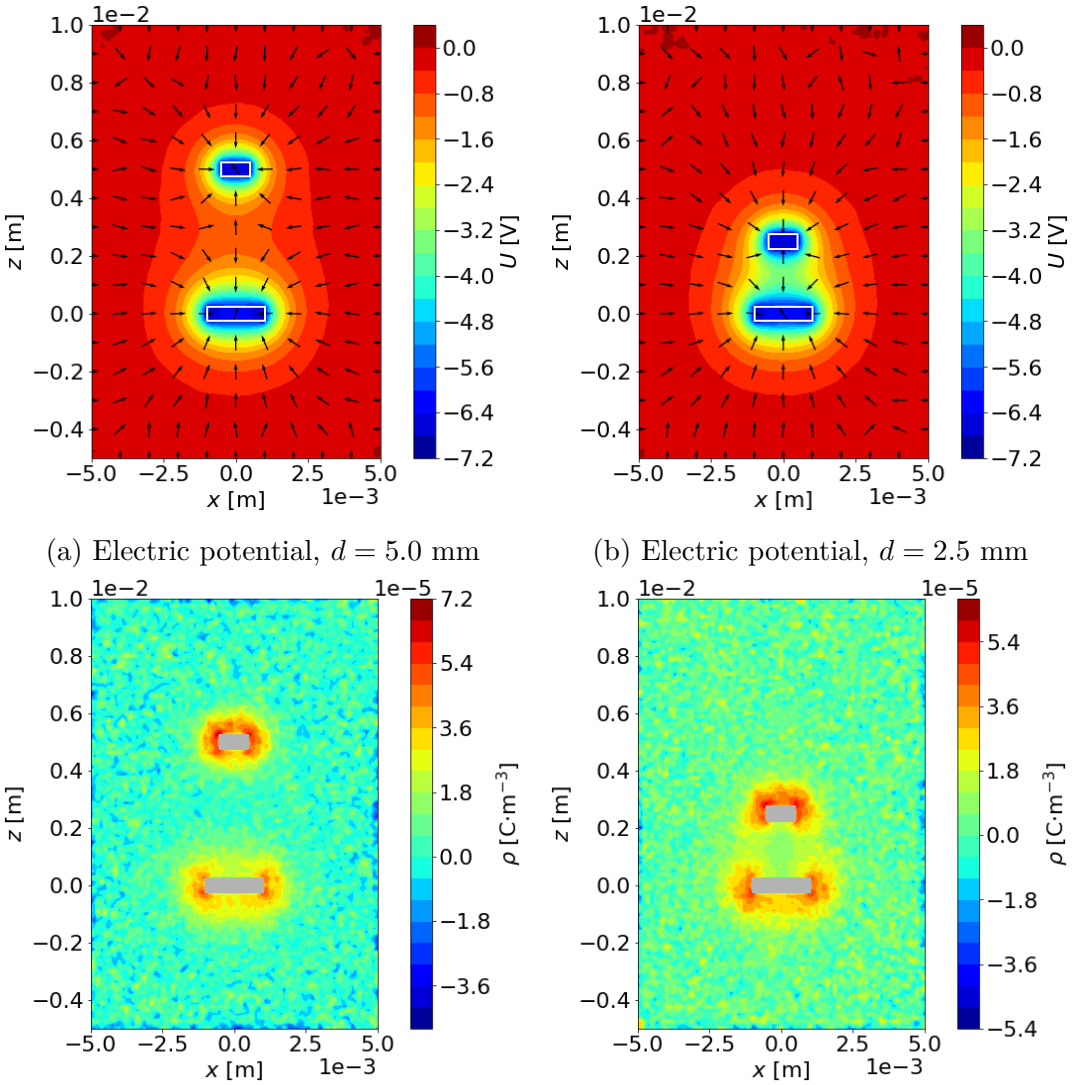

(a) Electric potential, $d = 5.0$ mm

(b) Electric potential, $d = 2.5$ mm

(c) Charge density, $d = 5.0$ mm

(d) Charge density, $d = 2.5$ mm

Figure 4.26: Electric potential and space charge density distribution in the surroundings of two interacting planar probes in 3D space, XZ plane cut at $y = 0$ m. The large probe is negatively biased ($U_{LP} = -6.65$ V), the smaller probe is at floating potential ($U_{SP} = -6.50$ V).

In both cases of positive and negative bias of the large probe, the effect of the fact that there is a $1/r$ diffusion profile of the number density of the charged particles in the vicinity of the smaller probe, which limits the number density in the area between the probes, is apparently applied. It also holds that in all cases shown, the sheath layer does not change at the surface of the probe, which is turned away from the second, interacting probe.

Now let us take a look at the figure 4.32 and the table 4.12 where IV characteristics of the large probe for different mutual positions of the interacting probes are shown and compared to the IV characteristic of the single planar probe modelled in 3D space, which was presented in the chapter 4.2. From the figure 4.32, it can be seen that the differences in the values of the electron and ion current flowing to the large probe are relatively small and become apparent only when using a logarithmic scale. A lower current flowing to the large probe is observed

for the closer distance between the probes; however, the overall shape of the IV characteristic remains the same for different distances between the probes.

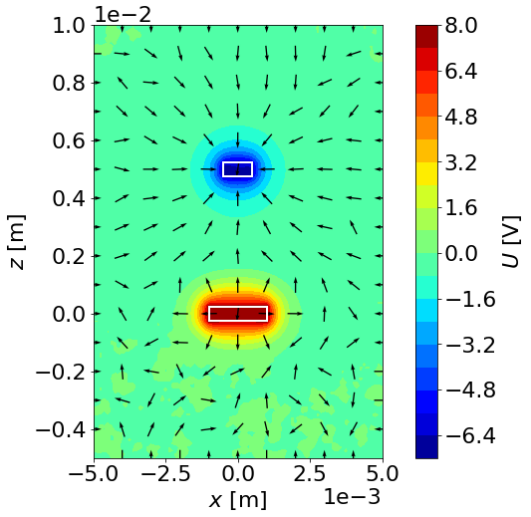

(a) Electric potential, $d = 5.0$ mm

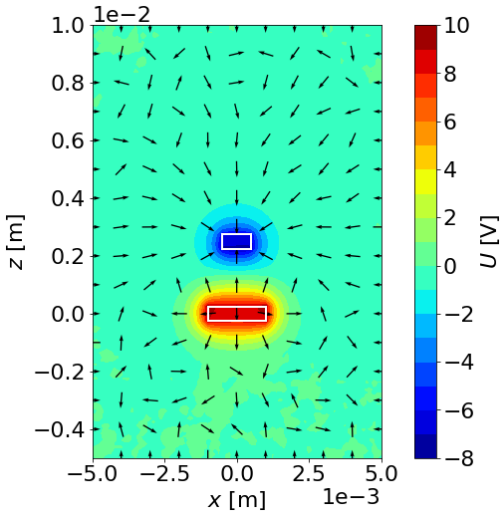

(b) Electric potential, $d = 2.5$ mm

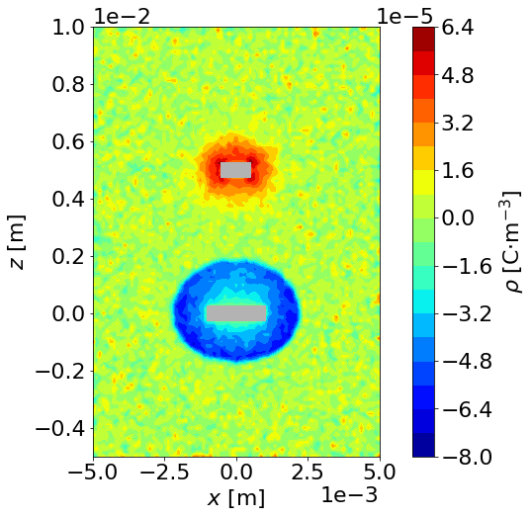

(c) Charge density, $d = 5.0$ mm

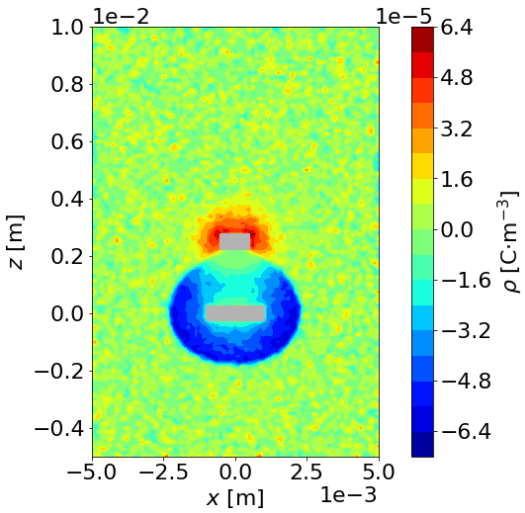

(d) Charge density, $d = 2.5$ mm

Figure 4.27: Electric potential and space charge density distribution in the surroundings of two interacting planar probes in 3D space, XZ plane cut at $y = 0$ m. The large probe is positively biased ($U_{LP} = 7.86$ V), the smaller probe is at floating potential ($U_{SP} = -6.50$ V).

From the table 4.12 it can be seen that due to the lower current on the large probe, after evaluating the IV characteristics, we get a proportionally lower number density of electrons n_e for the closer distance between the probes. In contrast, the electron temperature T_e evaluated from the IV characteristic remains approximately the same for different probe positions and the presence of the smaller probe at the floating potential therefore has no effect on it. Furthermore, we observe that as the probes are closer, the value of the floating potential U_f evaluated from the IV characteristic of the large probe decreases, and at the same time the value of the current density of the charged particles j_f also decreases at this bias. A lower value of the floating potential U_f indicates that positive ions

are more sensitive to the presence of the smaller probe, whose flow to the large probe decreases more than the flow of electrons when the probes are closer, and the floating potential thus reaches a lower value.

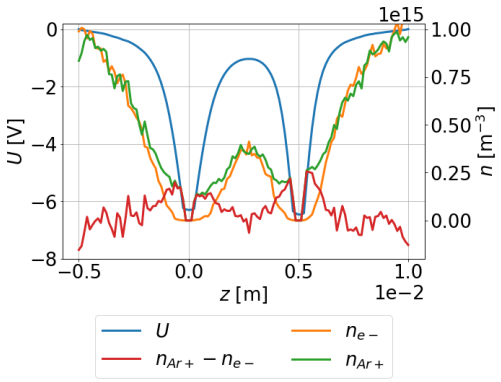

(a) Profiles of electric potential and number density of the charged particles

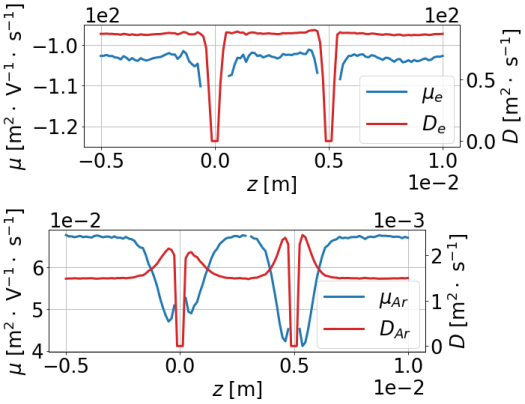

(b) Profiles of transport coefficients

Figure 4.28: Sheath structure in the surroundings of two interacting planar probes modelled in 3D space. The large probe is negatively biased ($U_{LP} = -6.65$ V), the smaller probe is at floating potential ($U_{SP} = -6.50$ V) and mutual distance between the probes is $d = 5$ mm.

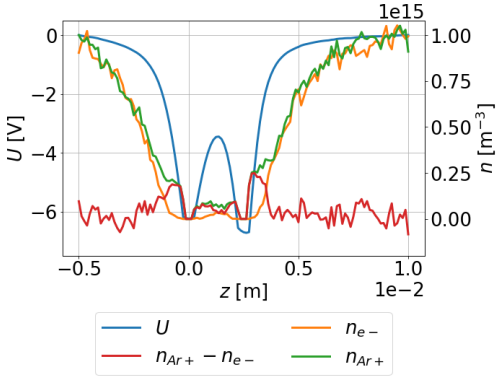

(a) Profiles of electric potential and number density of the charged particles

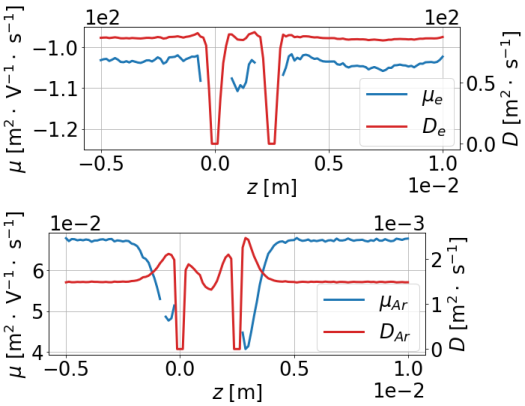

(b) Profiles of transport coefficients

Figure 4.29: Sheath structure in the surroundings of two interacting planar probes modelled in 3D space. The large probe is negatively biased ($U_{LP} = -6.56$ V), the smaller probe is at floating potential ($U_{SP} = -6.80$ V) and mutual distance between the probes is $d = 2.5$ mm.

Figure 4.33 shows the situation on the smaller probe at different biases of the large probe. It can be seen that if the large probe is at the plasma potential ($U_{LP} = 0$ V), then the potential of the smaller probe required to equalize the electron and ion current on it is slightly lower than the floating potential evaluated in the chapter 4.2 for a single planar probe, which, however, had dimensions corresponding to the large probe in the currently studied case.

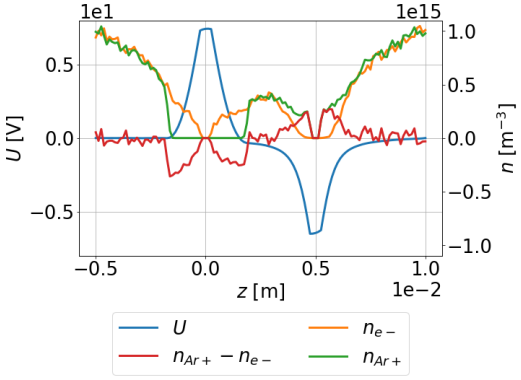

(a) Profiles of electric potential and number density of the charged particles

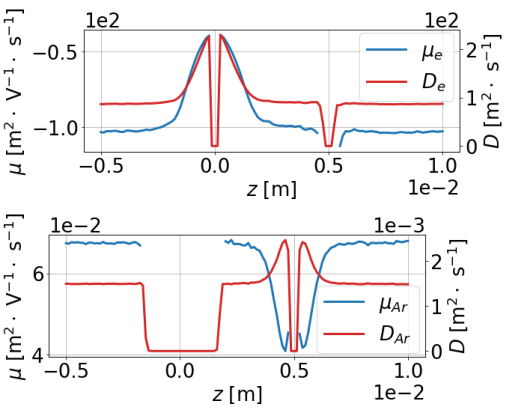

(b) Profiles of transport coefficients

Figure 4.30: Sheath structure in the surroundings of two interacting planar probes modelled in 3D space. The large probe is positively biased ($U_{LP} = 7.86$ V), the smaller probe is at floating potential ($U_{SP} = -6.50$ V) and mutual distance between the probes is $d = 5$ mm.

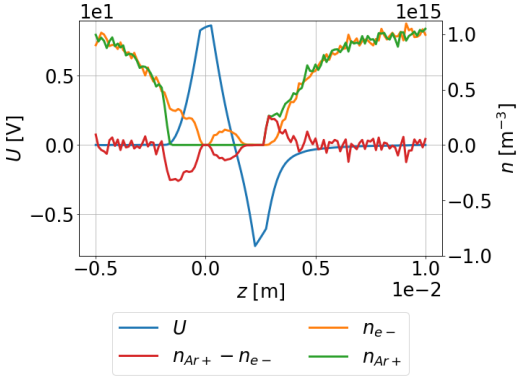

(a) Profiles of electric potential and number density of the charged particles

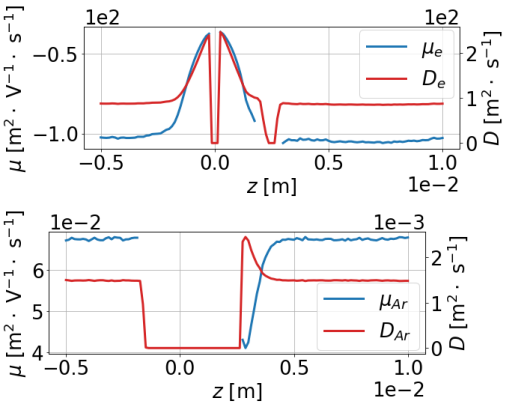

(b) Profiles of transport coefficients

Figure 4.31: Sheath structure in the surroundings of two interacting planar probes modelled in 3D space. The large probe is positively biased ($U_{LP} = 8.87$ V), the smaller probe is at floating potential ($U_{SP} = -6.72$ V) and mutual distance between the probes is $d = 2.5$ mm.

Furthermore, under these conditions, we observe that the flux of the charged particles to a smaller probe is greater than the flux of the charged particles to the single planar probe at the floating potential. The reason is probably related to the shape of the probe – the smaller probe is more similar to a spherical probe and a $1/r$ number density profile is indeed formed around it. In the case of the larger probe, the number density profile is not exactly $1/r$, but for straight parts it can locally transition to a linear profile and thus to a smaller number density of particles in the vicinity of the probe (see e.g. the figure 4.28a). As a result, we apparently observe a lower current density for the large probe than for the smaller one. Since the observed current density is greater with the smaller probe, the floating potential can apparently drop slightly as such a large value is not required to maintain a sufficiently large ion current.

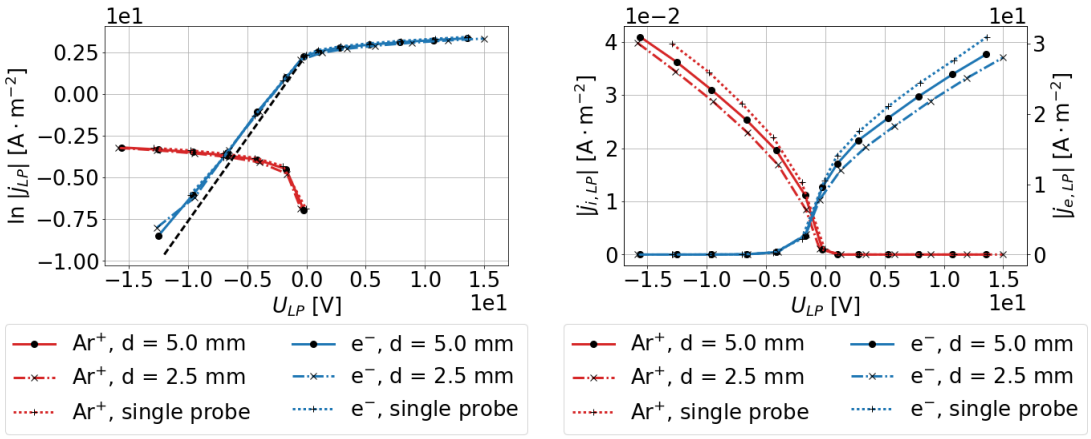

(a) Logarithmic scale

(b) Linear scale

Figure 4.32: IV characteristics of the large planar probe for two positions of the interacting smaller planar probe which is at floating potential and comparison with IV characteristics of a single planar probe modelled in 3D space. (Black dashed line marks current density which would correspond to the Maxwellian electrons of temperature $T_e = 11\,605$ K.)

Model	$j_{e,0}$ [A · m^{-2}]	T_e [K]	n_e [m^{-3}]	U_f [V]	j_f [A · m^{-2}]
2 probes, $d = 2.5$ mm	8.956	13 580	3.09×10^{14}	−7.49	2.48×10^{-2}
2 probes, $d = 5.0$ mm	10.25	13 135	3.60×10^{14}	−7.07	2.61×10^{-2}
Single probe	10.82	13 294	3.77×10^{14}	−6.79	2.93×10^{-2}

Table 4.12: Evaluation of the IV characteristics of the large planar probe modelled in 3D space which interacts with the smaller planar probe, comparison with values obtained for the single planar probe modelled in 3D space is provided.

Further, we observe that both in the case of positive and negative biasing of the large probe, the value of the bias voltage of the smaller probe, which is needed to equalize the electron and ion flux on it, decreases, and these fluxes themselves also decrease. So what seems to be crucial is what effect the large probe has on the positive ions – if the large probe is negatively biased, it will take over the positive ions of the smaller probe, as a result of which its voltage must be decreased to maintain a large enough flow of positive ions. If the large probe is positively biased, it will repel positive ions from around the smaller probe and the smaller probe must lower its voltage again to maintain a sufficiently high ion current.

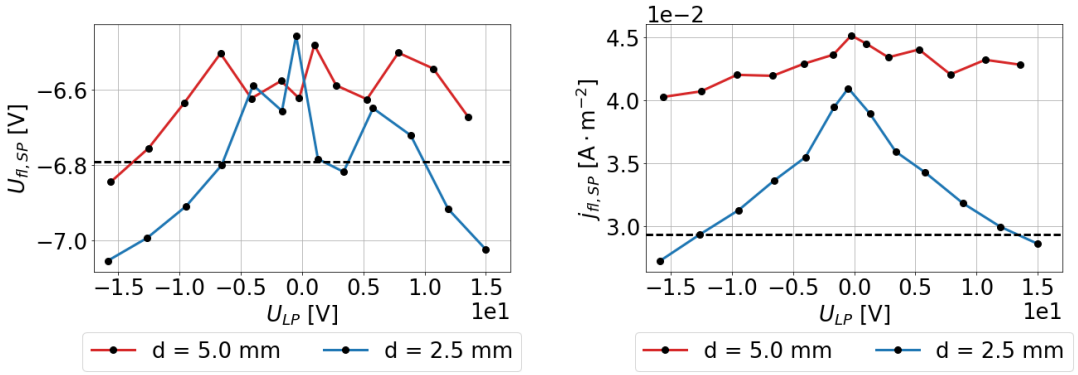

(a) Bias of the smaller planar probe at which the fluxes of electrons and Ar^+ ions are equal

(b) Current density of the charged particles on the smaller probe

Figure 4.33: Parameters of the smaller planar probe for different values of the electric bias of the large planar probe. (Black dashed line marks values obtained for the single planar probe modelled in 3D space.)

Conclusion

The thesis deals with the study of the sheath layer which is formed during the interaction of a low-temperature plasma with a solid object using computer modelling techniques.

In the theoretical part of the thesis (chapter 1), the findings available from the literature on the physics of the sheath layer of low-temperature electropositive and electronegative collisionless plasma were summarized. In a separate subchapter, it was described what effect collisions of charged particles with neutrals have on the sheath layer. A collisonless theory of measuring plasma parameters using a Langmuir probe was also presented, which was also supplemented with findings regarding the effect of collisions on the probe measurements.

The next chapter of the thesis (chapter 2) was devoted to the theoretical foundations of computer models that were developed and used within the framework of the thesis. The basic idea of the Particle-in-Cell method, which is a well-established method in plasma research, was presented. The theory needed for its practical implementation was described, including a discussion of the conditions that must be met for its stability. Furthermore, the theory of fluid low-temperature plasma modelling based on the drift-diffusion approximation was described.

The part of the thesis in which the achieved results are described is made up of two chapters. In the first chapter (chapter 3), the implementation of the developed computer models is described in detail, mainly of the 3D PIC/MCC code. In addition to the standard procedures used in the Particle-in-Cell modelling methodology, the unique elements of our implementation are described here, which are:

- Application of the Intel® Math Kernel Library (MKL) [Intel Corporation, 2017] routines to solve the Poisson's equation.

- Methodology for modelling electrically charged objects immersed in a 3D computational domain using the definition of the equivalent charge density distribution at their location. This methodology makes it possible to use the extremely fast functions of the Intel MKL library based on the fast Fourier transform for solving the Poisson's equation.

- The enhanced null collision method [Roucka and Hrach, 2011] for dealing with collisions of the charged particles with neutrals.

Stability and accuracy tests of the developed 3D PIC/MCC model were successfully performed as well as its comparison with the results of the Reid's benchmark. In the paragraph dedicated to the implementation of the fluid model based on the drift-diffusion approximation, we describe the formulation of the problem in the form that was needed to create a model using the finite element method using the FEniCS software [Alnæs et al., 2015].

The second chapter (chapter 4) dedicated to the achieved results describes a total of five physical problems that were solved with the help of the developed computer models.

The first physical problem (the chapter 4.1.2) was the study of the sheath layer and the IV characteristics of an infinitely large planar probe in the medium pressure range (4 torr = 532 Pa), where 1D symmetry could be used. Much space has been devoted here to discussing the differences between fluid models based on the drift-diffusion approximation and particle models based on the Particle-in-Cell method, which is inherently more accurate, which has also been confirmed. All the values of the physical parameters obtained from the models were explained, but in conclusion it can be stated that 1D symmetric models of the sheath layer are more suitable for qualitative analysis than for quantitative, since in a given pressure regime the results of the models directly depend on the selected size of the computational domain. The 1D planar probe model is also highly idealized in that it does not include boundary effects and effects of the finite dimensions of the probe, e.g. orbital motions of charged particles in its surroundings.

The second investigated case (the chapter 4.2) was the modelling of the sheath layer and IV characteristics of a planar probe of finite dimensions in 3D space. The study was again performed for electropositive argon medium pressure plasma. The real geometry of the probe made it possible to include edge effects in the calculations as well as possible orbital motions of the charged particles in its vicinity. At a sufficiently large distance, it is possible to consider a planar probe of finite dimensions as a spherical probe. This was manifested, for example, by the observation of the $1/r$ diffusion profile of the number density of charged particles in the vicinity of the probe compared to the linear profile observed in the 1D case or by the increasing electron current observed on the IV characteristic at a positive bias of the probe compared to the constant current in the 1D case. As in the 1D case, it was observed that a positive probe bias is well shielded by electrons, while at a negative probe bias, the electric field reaches a relatively large distance from the probe due to the existence of the pre-sheath. Compared to the 1D model, in the 3D model, potential shielding generally occurs at shorter distances, which is due to the higher number density of particles at the sheath edge due to the $1/r$ diffusion profile of the number density of charged particles in the vicinity of the probe. The 3D model of the probe pointed to the accumulation of (mainly positive) space charge density in the places of a strong electric field at the edges of the probe, which led us to hypothesize that this could be the reason for the higher detected floating potential compared to the 1D model – a strong electric field at the edges of the probe could increase the ion current relative to the electron one and thus increase the floating potential. Further, in accordance with the theory, it was observed that the directed velocity of the positive ions upon entering the sheath is lower than the value of the Bohm velocity due to the collisions with neutrals. An excellent agreement with the theory was achieved in the case of the electron current on the probe maintained at the plasma potential – the calculated value was in excellent agreement with the value given by the relation that took into account the collision effects. This led us to the conclusion that, under the given conditions, for the correct determination of the number density of the particles from the IV characteristic, it is not possible to use the relation for a collisionless plasma, and the effect of collisions must be definitely taken into account. The electron temperature evaluated from the calculated IV characteristic was 14.5% higher than the value in the source of the particles. The reason for such a difference could be the presence of a positive space charge

in front of the negatively charged probe sensing the electron current, which is apparently not included in the classical expression for collisionless plasma which is used to evaluate the electron temperature from the IV characteristic.

The third case studied (the chapter 4.3.1) was the interaction of the sheaths of two cylindrical probes in an electropositive argon plasma. A 2D PIC/MCC model was used to calculate the IV characteristics of a smaller cylindrical probe that was placed at different positions relative to a large cylindrical probe with a positive electrical bias. By evaluating the calculated IV characteristics, it was found that the smaller cylindrical probe is able to capture the decrease in the number density of charged particles in the vicinity of the large cylindrical probe. It turns out that the presence of the positively charged large probe significantly distorts the temperature of the electrons measured with the smaller probe – for the closer distance between the probes we get a lower temperature which is probably due to the fact that the positively charged large probe attracts electrons that would otherwise end up on the negatively charged smaller probe measuring electron current. It is consequently smaller which leads to a lower measured temperature. The observed effect is stronger for closer probe spacing. An interesting finding was that the (electron) current on the positively charged large probe decreases for both positive and negative biasing of the smaller probe. The smaller probe therefore either repels electrons from the surroundings of the large probe with its negative potential, or, on the contrary, accepts them in the case of a positive bias. The current drop on the large probe is more significant when the smaller probe is negatively biased, since due to the need for a pre-sheath, a relatively high electric field reaches a relatively large distance from the smaller probe. The observed current drop per large probe is higher at closer probe spacing.

The subject of the fourth studied physical problem were the sheath structures created around cylindrical probes in an electronegative plasma containing electrons, negative O^- ions and positive Ar^+ ions (i.e. a very simplified model of Ar/O_2 plasma). The study was carried out using a 2D PIC/MCC model; at first, the sheath of a single cylindrical probe was examined for its positive and negative bias and for different values of plasma electronegativity. In accordance with the theory, it was found that even with the same ratio of electrons and negative ions, these are rather electrons which contribute to the shielding of external potentials and negative ions tend to remain in the plasma bulk. Further, the interaction of the sheath of the positively biased larger cylindrical probe with the sheath of the smaller probe (positively and negatively biased) was studied for various mutual positions and different values of plasma electronegativity. It was found that with greater electronegativity, the sheaths have a larger size and can thus begin to overlap already at a greater distance between the probes. On the other hand, with a higher electronegativity, the required directed velocity of positive ions upon entering the sheath of negatively biased probe is lower than Bohm velocity since positive and negative ions have comparable thermal energy. As a result, lower potential drop is needed in the pre-sheath and electric field does not reach such large distances as in the case of low electronegativity. The interaction of the probes, whose sheaths do not spatially overlap, is thus less intense.

The last investigated physical problem was the interaction of the sheaths of two planar probes of finite dimensions in 3D space (the chapter 4.4). Using the developed 3D PIC/MCC model, the IV characteristic of a larger probe was

calculated near which a smaller half-sized probe was placed. The potential of this smaller probe was maintained at such a value as to equalize the flow of electrons and positive ions to it in each situation. The study was performed for an electropositive argon plasma and two relative positions of the probes. It was observed that the number density of the charged particles in the vicinity of the large probe was reduced due to the presence of the smaller probe simply by creating a diffuse $1/r$ profile of the number density in its vicinity. Since the smaller probe was maintained at a floating potential all the time, it had a negative bias with respect to the plasma potential and its electric field thus penetrated to a relatively large distance thanks to the existence of the pre-sheath. As a result, the smaller probe influenced, albeit slightly, the sheath structure of the large probe even at a greater distance between the probes. It was observed that the smaller probe with its electric field either removed the positive charge density from the negatively biased large probe or repelled the negative charge density from it during its positive bias. As expected, the sheath structure of the large probe did not change much on the side away from the smaller probe. From the calculated IV characteristics, it was seen that when the probes were closer, both the electron and ion current to the large probe was lower. This resulted in a lower number density of the charged particles evaluated in the standard way from the IV characteristic. The presence of the smaller probe, on the other hand, had no effect on the electron temperature value evaluated from the IV characteristic. This is a somewhat different observation compared to the chapter 4.3.1 where a lower temperature was observed for closer probe spacing – however, in that study the calculation setup was different (the IV characteristic was measured with a smaller probe and the large probe was held at a constant positive bias, not at a floating potential). At a closer distance, the calculated IV characteristic resulted in a lower floating potential – positive ions were apparently more sensitive to the presence of a smaller probe, the flow of which to the probe decreased more than the flow of electrons, and the floating potential thus reached a lower value. It was interesting to observe that the voltage of the smaller probe required to maintain a balanced flow of electrons and ions on it dropped for both the positive and negative bias of the large probe. So the effect of the large probe on the positive ions prevailed – if the large probe had a negative bias, it began to take over the positive ions of the smaller probe, as a result of which its voltage had to be reduced in order to maintain a sufficiently large flow of the positive ions. If the large probe had a positive bias, it began to repel positive ions from the surroundings of the smaller probe, and the smaller probe had to lower its voltage again to maintain a sufficiently high ion current.

As a great contribution of the work, we see the successful implementation of a 3D PIC/MCC plasma-solid interaction model that can be used to solve problems of up to macroscopic dimensions on an average workstation with 32 computational cores and 64 GB of RAM memory.

In conclusion, it can be stated that within the framework of the presented work, 2D and 3D computer models of the interaction of low-temperature plasma with a solid object were successfully developed, the results of which were verified by comparison with theory and with the help of which it was possible to describe in detail the unique issue of the interaction of several sheath layers.

Bibliography

J. E. Allen, R. L. F. Boyd, and P. Reynolds. The collection of positive ions by a probe immersed in a plasma. *Proceedings of the Physical Society. Section B*, 70(3):297, 1957. doi: 10.1088/0370-1301/70/3/303.

M. S. Alnæs, J. Blechta, J. Hake, A. Johansson, B. Kehlet, A. Logg, C. Richardson, J. Ring, M. E. Rognes, and G. N. Wells. The FEniCS project version 1.5. *Archive of Numerical Software*, 3(100):9–23, 2015. doi: 10.11588/ans.2015.100.20553.

L. L. Alves. Fluid modelling of the positive column of direct-current glow discharges. *Plasma Sources Science and Technology*, 16(3):557–569, 2007. doi: 10.1088/0963-0252/16/3/015.

ANSYS, Inc. ANSYS Electronics Desktop Student, 2021. URL `https://www.ansys.com/academic/students/ansys-electronics-desktop-student`.

E. V. Barnat and G. A. Hebner. Electric field profiles around an electrical probe immersed in a plasma. *Journal of Applied Physics*, 101(1):013306, 2007. doi: 10.1063/1.2404471.

I. B. Bernstein and I. N. Rabinowitz. Theory of electrostatic probes in a low-density plasma. *The Physics of Fluids*, 2(2):112–121, 1959. doi: 10.1063/1.1705900.

C. K. Birdsall and A. B. Langdon. *Plasma Physics via Computer Simulation*. Adam Hilger, Bristol, 1991. ISBN 0070053715. doi: 10.1201/9781315275048.

A. Bogaerts, R. Gijbels, and W. Goedheer. Hybrid modeling of a capacitively coupled radio frequency glow discharge in argon: combined Monte Carlo and fluid model. *Japanese Journal of Applied Physics*, 38(Part 1, No. 7B):4404–4415, 1999. doi: 10.1143/jjap.38.4404.

S. Bose, M. Kaur, P. K. Chattopadhyay, J. Ghosh, Y. C. Saxena, and R. Pal. Langmuir probe in collisionless and collisional plasma including dusty plasma. *Journal of Plasma Physics*, 83(2):615830201, 2017. doi: 10.1017/S0022377817000289.

R. L. F. Boyd and J. B. Thompson. The operation of Langmuir probes in electro-negative plasmas. *Proceedings of the Royal Society of London. Series A. Mathematical and Physical Sciences*, 252(1268):102–119, 1959. doi: 10.1098/rspa.1959.0140.

N. St. J. Braithwaite and J. E. Allen. Boundaries and probes in electronegative plasmas. *Journal of Physics D: Applied Physics*, 21(12):1733–1737, 1988. doi: 10.1088/0022-3727/21/12/011.

F. F. Chen. Electric probes. In R. H. Huddlestone and S. L. Leonard, editors, *Plasma Diagnostic Techniques*, pages 113–200. Academic Press, New York, 1965a.

F. F. Chen. Numerical computations for ion probe characteristics in a collisionless plasma. *Journal of Nuclear Energy. Part C, Plasma Physics, Accelerators, Thermonuclear Research*, 7(1):47, 1965b. doi: 10.1088/0368-3281/7/1/306.

Y. S. Chou, L. Talbot, and D. R. Willis. Kinetic theory of a spherical electrostatic probe in a stationary plasma. *The Physics of Fluids*, 9(11):2150–2167, 1966. doi: 10.1063/1.1761585.

G. Colonna and A. D'Angola, editors. *Plasma Modeling*. 2053–2563. IOP Publishing, Bristol, 2016. ISBN 978-0-7503-1200-4. doi: 10.1088/978-0-7503-1200-4.

E. Cormier-Michel, B. A. Shadwick, C. G. R. Geddes, E. Esarey, C. B. Schroeder, and W. P. Leemans. Unphysical kinetic effects in particle-in-cell modeling of laser wakefield accelerators. *Physical Review E*, 78(1):016404, 2008. doi: 10.1103/PhysRevE.78.016404.

T. A. Davis. Algorithm 832: UMFPACK V4.3 – an unsymmetric-pattern multifrontal method. *ACM Transactions on Mathematical Software*, 30(2):196–199, 2004. doi: 10.1145/992200.992206.

J. M. Dawson. Particle simulation of plasmas. *Reviews of Modern Physics*, 55 (2):403–447, 1983. doi: 10.1103/RevModPhys.55.403.

R. N. Franklin. What significance does the Bohm criterion have in an active collisional plasma–sheath? *Journal of Physics D: Applied Physics*, 35(18): 2270, 2002. doi: 10.1088/0022-3727/35/18/307.

R. N. Franklin and J. Snell. The free fall column with negative ions. *Journal of Physics D: Applied Physics*, 25(3):453–457, 1992. doi: 10.1088/0022-3727/25/3/017.

R. N. Franklin and J. Snell. The transition from collisionless to collisional active plasma in the fluid model and the relevance of the Bohm criterion to sheath formation. *Physics of Plasmas*, 7(7):3077–3083, 2000. doi: 10.1063/1.874161.

G. Fubiani and J. P. Boeuf. Role of positive ions on the surface production of negative ions in a fusion plasma reactor type negative ion source – insights from a three dimensional particle-in-cell Monte Carlo collisions model. *Physics of Plasmas*, 20(11):113511, 2013. doi: 10.1063/1.4834475.

P. Gambron and S. Thorne. Comparison of several FFT libraries in C/C++. Technical report RAL-TR-2020-003, Rutherford Appleton Laboratory, Harwell Oxford, 2020. URL `https://epubs.stfc.ac.uk/manifestation/45434584/RAL-TR-2020-003.pdf`.

P. Garcia-Risueno, J. Alberdi-Rodriguez, M. J. T. Oliveira, X. Andrade, M. Pippig, J. Muguerza, A. Arruabarrena, and A. Rubio. A survey of the parallel performance and accuracy of Poisson solvers for electronic structure calculations. *Journal of Computational Chemistry*, 35(6):427–444, 2014. doi: 10.1002/jcc.23487.

A. Gholami, D. Malhotra, H. Sundar, and G. Biros. FFT, FMM, or multigrid? A comparative study of state-of-the-art Poisson solvers for uniform and non-uniform grids in the unit cube. *SIAM Journal on Scientific Computing*, 38(3): C280–C306, 2016. doi: 10.1137/15M1010798.

V. A. Godyak and N. Sternberg. Smooth plasma-sheath transition in a hydrodynamic model. *IEEE Transactions on Plasma Science*, 18(1):159–168, 1990. doi: 10.1109/27.45519.

E. Havlickova, P. Bartos, and R. Hrach. Computational study of plasma-solid interaction in DC glow discharge in argon plasma at medium pressures. *Journal of Physics: Conference Series*, 63:012019, 2007. doi: 10.1088/1742-6596/63/1/012019.

R. W. Hockney and J. W. Eastwood. *Computer simulation using particles*. First Edition. Taylor & Francis, Inc., Bristol, PA, USA, 1988. ISBN 0-85274-392-0. doi: 10.1201/9780367806934.

J. Hromadka, T. Ibehej, and R. Hrach. Computational study of plasma sheath interaction. *Physica Scripta*, 2014(T161):014068, 2014. doi: 10.1088/0031-8949/2014/t161/014068.

J. Hromadka, T. Ibehej, and R. Hrach. Computer modelling of electronegative plasma sheaths and their mutual interaction. *Physica Scripta*, 90(10):105603, 2015. doi: 10.1088/0031-8949/90/10/105603.

J. Hromádka. Aplikace metod počítačové fyziky při studiu interakce plazmatu s pevnými látkami. Master's thesis, Charles University, Prague, Czech Republic, 2013.

V. Hruby and R. Hrach. Three-dimensional hybrid computer modeling of Langmuir probes of finite dimensions in medium pressure plasmas. *IEEE Transactions on Plasma Science*, 38(9):2328–2331, 2010. doi: 10.1109/TPS.2010.2056702.

J. D. Hunter. Matplotlib: A 2D graphics environment. *Computing in Science and Engineering*, 9(3):90–95, 2007. doi: 10.1109/MCSE.2007.55.

T. Ibehej, J. Hromádka, and R. Hrach. Computer simulation of metal ions transport to uneven substrates during ionized plasma vapour deposition. *Advances in Materials Science and Engineering*, 2017:4283547, 2017. doi: 10.1155/2017/4283547.

H. Ibeid, L. Olson, and W. Gropp. FFT, FMM, and multigrid on the road to exascale: Performance challenges and opportunities. *Journal of Parallel and Distributed Computing*, 136:63–74, 2020. doi: 10.1016/j.jpdc.2019.09.014.

Intel Corporation. Intel® oneAPI Math Kernel Library, 2017. URL `https://www.intel.com/content/www/us/en/developer/tools/oneapi/onemkl.html`.

A. Kalinkin, Y. M. Laevsky, and S. Gololobov. 2D fast Poisson solver for high-performance computing. In V. Malyshkin, editor, *Parallel Computing Technologies*, pages 112–120, Berlin Heidelberg, 2009. Springer. ISBN 978-3-642-03275-2. doi: 10.1007/978-3-642-03275-2_11.

G. Keller, U. Rüde, L. Stals, S. Mändl, and B. Rauschenbach. Simulation of trench homogeneity in plasma immersion ion implantation. *Journal of Applied Physics*, 88(2):1111–1117, 2000. doi: 10.1063/1.373784.

S. Khokhriakov, R. R. Manumachu, and A. Lastovetsky. Performance optimization of multithreaded 2D fast Fourier transform on multicore processors using load imbalancing parallel computing method. *IEEE Access*, 6:64202–64224, 2018. doi: 10.1109/ACCESS.2018.2878271.

M. J. Kushner. Hybrid modelling of low temperature plasmas for fundamental investigations and equipment design. *Journal of Physics D: Applied Physics*, 42(19):194013, 2009. doi: 10.1088/0022-3727/42/19/194013.

J. G. Laframboise. Theory of spherical and cylindrical Langmuir probes in a collisionless, Maxwellian plasma at rest. Technical report UTIAS Report, No. 100, University of Toronto, Institute for Aerospace Studies, Toronto, 1966. URL `https://apps.dtic.mil/sti/pdfs/AD0634596.pdf`.

I. Langmuir and K. B. Blodgett. Currents limited by space charge between coaxial cylinders. *Physical Review*, 22:347–356, 1923. doi: 10.1103/PhysRev.22.347.

I. Langmuir and K. B. Blodgett. Currents limited by space charge between concentric spheres. *Physical Review*, 24:49–59, 1924. doi: 10.1103/PhysRev.24.49.

G. Lapenta. Particle simulations of space weather. *Journal of Computational Physics*, 231(3):795–821, 2012. doi: 10.1016/j.jcp.2011.03.035.

A. J. Lichtenberg, V. Vahedi, M. A. Lieberman, and T. Rognlien. Modeling electronegative plasma discharges. *Journal of Applied Physics*, 75(5):2339–2347, 1994. doi: 10.1063/1.356252.

M. A. Lieberman and A. J. Lichtenberg. *Principles of plasma discharges and materials processing*. John Wiley & Sons, Hoboken, 2005. ISBN 0-471-72001-1. doi: 10.1002/0471724254.

J. Lu and M. J. Kushner. Trench filling by ionized metal physical vapor deposition. *Journal of Vacuum Science & Technology A*, 19(5):2652–2663, 2001. doi: 10.1116/1.1399318.

S. Markidis and G. Lapenta. The energy conserving particle-in-cell method. *Journal of Computational Physics*, 230(18):7037–7052, 2011. doi: 10.1016/j.jcp.2011.05.033.

K. Matyash, R. Schneider, F. Taccogna, A. Hatayama, S. Longo, M. Capitelli, D. Tskhakaya, and F. X. Bronold. Particle in cell simulation of low temperature laboratory plasmas. *Contributions to Plasma Physics*, 47(8–9):595–634, 2007. doi: 10.1002/ctpp.200710073.

Y. Miyagawa, M. Ikeyama, S. Miyagawa, M. Tanaka, and H. Nakadate. Plasma analysis for the plasma immersion ion implantation processing by a PIC-MCC simulation. *Computer Physics Communications*, 177(1):84–87, 2007. doi: 10.1016/j.cpc.2007.02.034.

H. M. Mott-Smith and I. Langmuir. The theory of collectors in gaseous discharges. *Physical Review*, 28(4):727–763, 1926. doi: 10.1103/PhysRev.28.727.

N. Oudini, J.-L. Raimbault, P. Chabert, A. Meige, and A. Aanesland. Particle-in-cell simulation of an electronegative plasma under direct current bias studied in a large range of electronegativity. *Physics of Plasmas*, 20(4):043501, 2013. doi: 10.1063/1.4798501.

A. Phelps. Compilation of electron cross sections, 2013. URL `http://jila.colorado.edu/avp/collision_data/`.

A. Pukhov. Particle-in-cell codes for plasma-based particle acceleration. *Proceedings of the 2014 CAS-CERN Accelerator School: Plasma Wake Acceleration*, 1: 181–206, 2016. doi: 10.5170/CERN-2016-001.181.

I. D. Reid. An investigation of the accuracy of numerical solutions of boltzmann's equation for electron swarms in gases with large inelastic cross sections. *Australian Journal of Physics*, 32:231–254, 1979. doi: 10.1071/PH790231.

K. U. Riemann. The Bohm criterion and sheath formation. *Journal of Physics D: Applied Physics*, 24(4):493–518, 1991. doi: 10.1088/0022-3727/24/4/001.

K. U. Riemann. The Bohm criterion and boundary conditions for a multicomponent system. *IEEE Transactions on Plasma Science*, 23(3):709–716, 1995. doi: 10.1109/27.467993.

K. U. Riemann. The influence of collisions on the plasma sheath transition. *Physics of Plasmas*, 4(11):4158–4166, 1997. doi: 10.1063/1.872536.

S. Roucka and R. Hrach. Extending PIC models to higher pressures – enhanced model of collisions. *IEEE Transactions on Plasma Science*, 39(11):3244–3250, 2011. doi: 10.1109/TPS.2011.2164789.

Š. Roučka. Studium interakce plazma-pevná látka při středních tlacích. Master's thesis, Charles University, Prague, Czech Republic, 2008.

H. R. Skullerud. The stochastic computer simulation of ion motion in a gas subjected to a constant electric field. *Journal of Physics D: Applied Physics*, 1 (11):1567–1568, 1968. doi: 10.1088/0022-3727/1/11/423.

J. D. Swift and M. J. R. Schwar. *Electrical probes for plasma diagnostics*. Iliffe Books, London, 1969. ISBN 9780444196941.

L. Talbot and Y. Chou. Langmuir probe response in the transition regime. In C. L. Brundin, editor, *6th Rarefied Gas Dynamics Conference, Volume II*, pages 1723–1737, New York, 1969. Academic Press.

J. Teunissen and U. Ebert. 3D PIC-MCC simulations of discharge inception around a sharp anode in nitrogen/oxygen mixtures. *Plasma Sources Science and Technology*, 25(4):044005, 2016. doi: 10.1088/0963-0252/25/4/044005.

M. Tichy, M. Sicha, P. David, and T. David. A collisional model of the positive ion collection by a cylindrical Langmuir probe. *Contributions to Plasma Physics*, 34(1):59–68, 1994. doi: 10.1002/ctpp.2150340108.

H. Ueda, Y. Omura, H. Matsumoto, and T. Okuzawa. A study of the numerical heating in electrostatic particle simulations. *Computer Physics Communications*, 79(2):249–259, 1994. doi: 10.1016/0010-4655(94)90071-X.

V. Vahedi and M. Surendra. A Monte Carlo collision model for the particle-in-cell method: applications to argon and oxygen discharges. *Computer Physics Communications*, 87(1):179–198, 1995. doi: 10.1016/0010-4655(94)00171-W.

J. P. Verboncoeur, A. B. Langdon, and N. T. Gladd. An object-oriented electromagnetic PIC code. *Computer Physics Communications*, 87(1):199–211, 1995. doi: 10.1016/0010-4655(94)00173-Y.

Z. Zakrzewski and T. Kopiczynski. Effect of collisions on positive ion collection by a cylindrical Langmuir probe. *Plasma Physics*, 16(12):1195, 1974. doi: 10.1088/0032-1028/16/12/011.

X. C. Zeng, T. K. Kwok, A. G. Liu, P. K. Chu, and B. Y. Tang. Plasma immersion ion implantation of the interior surface of a large cylindrical bore using an auxiliary electrode. *Journal of Applied Physics*, 83(1):44–49, 1998. doi: 10.1063/1.366699.

List of Figures

List of Tables

List of Abbreviations

ABR	Allen-Boyd-Reynolds theory
BC	Boundary condition
BRL	Bernstein-Rabinowitz-Laframboise theory
CIC	Cloud-in-Cell algorithm
CFL	Courant-Friedrichs-Lewy condition
IV	Current-voltage characteristic of a Langmuir probe
MCC	Monte Carlo collision module
MKL	Intel® Math Kernel Library
OML	Orbital-motion-limited theory
PIC	Particle-in-Cell method

List of Publications

Impacted publications

J. Hromadka, T. Ibehej and R. Hrach. Computational study of plasma sheath interaction. *Physica Scripta*, 2014(T161):014068, 2014.

J. Hromadka, T. Ibehej and R. Hrach. Computer modelling of electronegative plasma sheaths and their mutual interaction. *Physica Scripta*, 90(10):105603, 2015.

T. Ibehej, J. Hromadka and R. Hrach. Computer simulation of metal ions transport to uneven substrates during ionized plasma vapour deposition. *Advances in Materials Science and Engineering*, 2017:4283547, 2017.

Conference proceedings (peer-reviewed)

J. Hromadka, T. Ibehej and R. Hrach. Computer modelling of sheaths in multicomponent plasma. In: *WDS'14 Proceedings of Contributed Papers — Physics*. Prague: Matfyzpress, 2014, pp. 255 – 260. ISBN 978-80-7378-276-4.

J. Hromadka, T. Ibehej and R. Hrach. Hybrid computer modelling in plasma physics. *Journal of Physics: Conference Series*, 759(1):012066, 2016.

J. Hromadka, T. Ibehej and R. Hrach. Parametric computational study of sheaths in multicomponent Ar/O_2 plasma. *Journal of Physics: Conference Series*, 982:012008, 2018.

Conference proceedings (not peer-reviewed)

J. Hromadka, T. Ibehej and R. Hrach. Interaction of sheaths in multicomponent plasma via computer modelling. In: *41st EPS Conference on Plasma Physics*, Berlin, Germany. European Physical Society, 2014. ISBN 2-914771-90-8.

J. Hromadka, T. Ibehej and R. Hrach. Fluid modelling of plasma at low pressures. In: *42nd EPS Conference on Plasma Physics*, Lisbon, Portugal. European Physical Society, 2015. ISBN 2-914771-98-3.

J. Hromadka, T. Ibehej and R. Hrach. Applications of hybrid computer models in plasma sheath physics. In: *44th EPS Conference on Plasma Physics*, Belfast, UK. European Physical Society, 2017. ISBN 979-10-96389-07-0.

A. Attachments

A.1 Collision cross section – definition and interpretation

General definition Let there be a beam of incident particles with density n and velocity $\boldsymbol{v}$ which enters a thin layer of material of thickness $\mathrm{d}x$. The flux of the beam $\boldsymbol{\Gamma} = n\boldsymbol{v}$ decreases by $\mathrm{d}\boldsymbol{\Gamma}$

$$\frac{\mathrm{d}\boldsymbol{\Gamma}}{\mathrm{d}x} = -n_g \sigma(\boldsymbol{v})\boldsymbol{\Gamma}, \tag{A.1.1}$$

where $\sigma(\boldsymbol{v})$ is the collision cross section, which generally depends on the velocity $\boldsymbol{v}$ of the incident particles, and n_g is number density of the scattering centers (targets). Solving the equation above, we can write that the flux of incident particles that did not undergo collision (= uncollided flux) is at the distance x given by

$$\boldsymbol{\Gamma_1} = \boldsymbol{\Gamma_0} \exp\left(-n_g \sigma x\right),$$

where $\boldsymbol{\Gamma_0}$ is flux of the beam at $x = 0$ (figure A.1). Similarly, we can write the flux of incident particles that already collided (= collided flux) at the distance x

$$\boldsymbol{\Gamma_2} = \boldsymbol{\Gamma_0} - \boldsymbol{\Gamma_1} = \boldsymbol{\Gamma_0}\left[1 - \exp\left(-n_g \sigma x\right)\right].$$

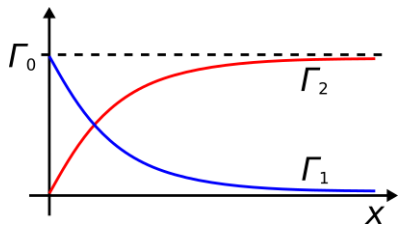

Figure A.1: Uncollided $\boldsymbol{\Gamma_1}$ and collided $\boldsymbol{\Gamma_2}$ flux of incident particles.

Similar expressions are valid for number density n. If the velocity $\boldsymbol{v}$ of the incident particles is constant along x axis, equation A.1.1 can be written as

$$\boldsymbol{v}\frac{\mathrm{d}n}{\mathrm{d}x} = -n_g \sigma(\boldsymbol{v}) n\boldsymbol{v}. \tag{A.1.2}$$

Then, we can write number density n_1 of incident particles at x that did not undergo collision yet and number density n_2 of those that already underwent collision

$$\begin{aligned} n_1 &= n_0 \exp\left(-n_g \sigma x\right), \\ n_2 &= n_0 - n_1 = n_0\left[1 - \exp\left(-n_g \sigma x\right)\right]. \end{aligned}$$

Further, we can write expression

$$p(x) = \frac{n_2(x)}{n_0} = 1 - \exp\left(-n_g \sigma x\right) \in (0, 1],$$

which is obviously the ratio of the particles that already underwent collision at x to the initial number density. This expression can be also interpreted as a probability that a concrete particle of interest from the beam already underwent collision at x (= cumulative distribution function), figure A.2. Expression for the probability density function in this case can be written as

$$f(x) = \frac{\mathrm{d}p}{\mathrm{d}x} = n_g \sigma \exp\left(-n_g \sigma x\right) = \frac{1}{\lambda} \exp\left(-\frac{x}{\lambda}\right),$$

where parameter $\lambda = \frac{1}{n_g \sigma}$ is called mean free path and it is the mean value of this probability distribution. Probability density function $f(x)$ above is normalized. Further, we define mean time between collisions τ

$$\tau = \frac{\lambda}{v} = \frac{1}{n_g \sigma v},$$

and collision frequency ν

$$\nu = \frac{1}{\tau} = n_g \sigma v.$$

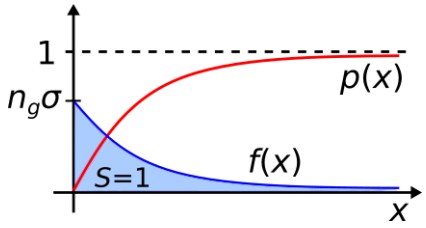

Figure A.2: Cumulative distribution function $p(x)$ for a probability that a concrete particle from the incident beam already underwent collision at x and probability density function $f(x)$.

Alternative interpretation 1 Let there be a target slab of thickness $\mathrm{d}x$ and of a very large area. Density of the scattering centers in the slab is n_g, each scattering center has a tiny projected area, cross section, σ. Let there be a beam of incoming particles (considered as point-like) of flux J [m^{-1}] and cross section A [m^2] which is smaller than the target area. If N is the number of particles fallen on the target, then number of particles coming through $\mathrm{d}x$ thickness without scattering event is $N + \mathrm{d}N$ where

$$\mathrm{d}N = -\frac{n_g A \mathrm{d}x \sigma}{A} N = -n_g \sigma N \mathrm{d}x.$$

Meaning of the expression above: number of particles that undergo scattering event is "some" ratio of the incoming N particles. This ratio corresponds to the ratio of all scattering center areas that are present in the beam area to the overall area available for the beam ($n_g A \mathrm{d}x$ = number of scattering centers, σ = cross section of a single scattering center). In terms of number densities, we can write

$$\mathrm{d}n = \frac{\mathrm{d}N}{V} = -n_g \sigma n \mathrm{d}x,$$

which is equivalent to the equation A.1.2.

Alternative interpretation 2 Let there be a beam of incident particles of density n and velocity v. We denote

$$\sigma = \pi \left(a_1 + a_2\right)^2,$$

where a_1 is radius of the incident projectiles and a_2 is radius of the targets. According to the figure A.3 we can write expression for the number of projectiles which hit a single particular target in time interval $\mathrm{d}t$

$$N_{\mathrm{d}t} = n\sigma v \mathrm{d}t.$$

If there is N_g targets, they are hit by

$$N_g N_{\mathrm{d}t} = N_g n\sigma v \mathrm{d}t$$

projectiles during time interval $\mathrm{d}t$. There are N_g targets in the volume V_g, $n_g = \frac{N_g}{V_g}$. Per unit volume, there is

$$\frac{N_g N_{\mathrm{d}t}}{V_g} = n_g n\sigma v \mathrm{d}t = \mathrm{d}n$$

interactions between projectiles and targets, this means number of projectiles per unit volume which hit some target in time $\mathrm{d}t$. As a result, we have

$$\mathrm{d}n = n_g \sigma n \mathrm{d}x,$$

which is equivalent to the equation A.1.2.

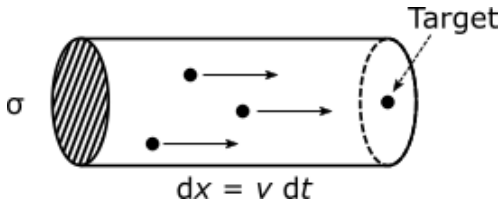

Figure A.3: Incident particles impinging on a single target.

Alternative interpretation 3 Let there be situation similar to that one presented in alternative definition 2 except: the concrete ion is at rest in the origin of the coordinate system, target particles of number density n_g and velocity v are moving towards the ion. In time interval $\mathrm{d}t$, there will be

$$N_{\mathrm{d}t} = n_g \sigma v \mathrm{d}t$$

hits of the ion by the targets.

Total and differential cross section Generally, collision cross section is dependent on the relative kinetic energy ϵ_r of the incident and target particles. For more precise way of description of the scattering processes we can introduce differential cross section σ_d which takes into account dependance of the cross section on the scattering (polar) angle χ. Total scattering cross section σ_t is related to the differential cross section σ_d by

$$\sigma_t\left(\epsilon_r\right) = 2\pi \int_0^{\pi} \sigma_d\left(\epsilon_r, \chi\right) \sin\chi \mathrm{d}\chi.$$

A.2 Null collision method

Implementation of the null collision method [Skullerud, 1968] in the developed plasma models is based on the approach which is described in the diploma thesis Roučka [2008] and in the article Roucka and Hrach [2011].

To model collisions of charged particles with neutral gas in background by Monte Carlo method, we need to know the following:

1. How often does the concrete charged particle collide with neutral ones?
2. What is the velocity distribution of the neutrals with which the charged particle interacts?

Let the concrete charged particle be e. g. ion moving in the neutral gas. According to the alternative interpretation of cross section no. 3 in section A.1 (the ion does not move, all neutral particles of n_g density move with velocity $\boldsymbol{v}$), there will be $N_{\mathrm{d}t}$ neutrals that hit the ion in time interval $(t, t + \mathrm{d}t)$

$$N_{\mathrm{d}t} = \nu_t \mathrm{d}t = n_g \sigma(\boldsymbol{v}) \left|\boldsymbol{v}\right| \mathrm{d}t,$$

where $\nu_t \, [\mathrm{s}^{-1}]$ is current collision frequency at time t. If the ion moves with velocity $\boldsymbol{v_0}$, we can write

$$N_{\mathrm{d}t} = \nu_t \mathrm{d}t = n_g \sigma(\boldsymbol{v} - \boldsymbol{v_0}) \left|\boldsymbol{v} - \boldsymbol{v_0}\right| \mathrm{d}t. \tag{A.2.1}$$

If the neutrals have velocity distribution $f(\boldsymbol{v})$, which is normalized $\int f(\boldsymbol{v})\mathrm{d}\boldsymbol{v} = 1$, we can write

$$N_{\mathrm{d}t} = \nu_t \mathrm{d}t = n_g \int f(\boldsymbol{v}) \sigma(\boldsymbol{v} - \boldsymbol{v_0}) \left|\boldsymbol{v} - \boldsymbol{v_0}\right| \mathrm{d}\boldsymbol{v}\mathrm{d}t.$$

We can denote

$$N_{\mathrm{d}\boldsymbol{v}\mathrm{d}t} = \nu_{\boldsymbol{v}t} \mathrm{d}\boldsymbol{v}\mathrm{d}t = n_g f(\boldsymbol{v}) \sigma(\boldsymbol{v} - \boldsymbol{v_0}) \left|\boldsymbol{v} - \boldsymbol{v_0}\right| \mathrm{d}\boldsymbol{v}\mathrm{d}t, \tag{A.2.2}$$

which is the number of neutrals with velocity $(\boldsymbol{v}, \boldsymbol{v} + \mathrm{d}\boldsymbol{v})$ that hit the ion in time interval $(t, t + \mathrm{d}t)$. Further, we can introduce normalized velocity distribution $g(\boldsymbol{v})$ of neutrals that hit the ion in time interval $(t, t + \mathrm{d}t)$

$$\begin{aligned} g(\boldsymbol{v})\mathrm{d}\boldsymbol{v} = \frac{N_{\mathrm{d}\boldsymbol{v}\mathrm{d}t}}{N_{\mathrm{d}t}} = \frac{\nu_{\boldsymbol{v}t}\mathrm{d}\boldsymbol{v}\mathrm{d}t}{\nu_t \mathrm{d}t} = \frac{n_g f(\boldsymbol{v}) \sigma(\boldsymbol{v} - \boldsymbol{v_0}) \left|\boldsymbol{v} - \boldsymbol{v_0}\right| \mathrm{d}\boldsymbol{v}}{n_g \int f(\boldsymbol{v}) \sigma(\boldsymbol{v} - \boldsymbol{v_0}) \left|\boldsymbol{v} - \boldsymbol{v_0}\right| \mathrm{d}\boldsymbol{v}} = \\ = \frac{n_g}{\nu_t} f(\boldsymbol{v}) \sigma(\boldsymbol{v} - \boldsymbol{v_0}) \left|\boldsymbol{v} - \boldsymbol{v_0}\right| \mathrm{d}\boldsymbol{v}. \end{aligned}$$

Let us suppose that the velocity distribution of neutrals is Maxwellian

$$\begin{aligned} f(\boldsymbol{v})\mathrm{d}\boldsymbol{v} &= \frac{1}{v_m^3 \pi^{\frac{3}{2}}} \exp\left(-\frac{v^2}{v_m^2}\right) \mathrm{d}\boldsymbol{v}, \\ v_m &= \left(\frac{2k_B T}{m}\right)^{\frac{1}{2}}. \end{aligned}$$

Further, let us suppose that the collision cross section is independent of the relative velocity $\sigma(\boldsymbol{v} - \boldsymbol{v_0}) = \sigma = \text{const.}$ and velocity of the ion is $\boldsymbol{v_0} = (0, 0, v_0)$.

Roučka [2008] shows that if the isotropic Maxwellian velocity distribution of neutrals is inserted into the equation A.2.2 and integration over solid angle is performed, we get

$$\begin{aligned} N_{\mathrm{d}v\mathrm{d}t} = \nu_{vt}\mathrm{d}v\mathrm{d}t &= \frac{4\pi}{3} n_g f(v) \sigma v^3 \left(3\frac{v_0}{v} + \frac{v}{v_0}\right) \mathrm{d}v\mathrm{d}t \ldots \text{for } v < v_0, \\ &= \frac{4\pi}{3} n_g f(v) \sigma v^3 \left(3 + \frac{v_0^2}{v}\right) \mathrm{d}v\mathrm{d}t \ldots \text{for } v > v_0. \end{aligned} \tag{A.2.3}$$

If the integration over velocitities is also performed, we get

$$\begin{aligned} \nu_t(v_0) &= n_g \sigma v_0 \left[\frac{1}{\pi^{\frac{1}{2}}} \frac{v_m}{v_0} \exp -\frac{v_0^2}{v_m^2} + \operatorname{erf}\left(\frac{v_0}{v_m}\right)\left(1 + \frac{1}{2}\frac{v_m^2}{v_0^2}\right)\right], \\ \lambda_t(v_0) &= \frac{v_0}{\nu_t(v_0)}. \end{aligned} \tag{A.2.4}$$

Velocity dependance of the collision frequency ν_t A.2.4 and mean free path λ_t of an Ar^+ ion which is moving in neutral argon gas with Maxwellian velocity distribution $f(v)$ is shown in the figure A.4. It can be seen that for small v_0 collision frequency (and thus time to the next collision) is constant. It can be also seen that for large v_0, mean free path λ is constant and collisions can be resolved by null collision method based on generation of random free path between collisions with a mean value $\lambda = \frac{1}{\sigma n}$. This corresponds to the situation when targets can be considered as stationary, e. g. in case of an electron moving in argon gas. In this approximation we can consider that velocity $\boldsymbol{v}$ of all the neutrals is $\boldsymbol{v} = 0$ and thus equation A.2.1 is simplified to

$$\begin{aligned} N_{\mathrm{d}t} = \nu_t \mathrm{d}t &= n_g \sigma(\boldsymbol{v_0}) \left|\boldsymbol{v_0}\right| \mathrm{d}t, \\ \Rightarrow \nu_t &= n_g \sigma(\boldsymbol{v_0}) v_0, \\ \Rightarrow \lambda &= \frac{v_0}{\nu_t} = \frac{1}{n_g \sigma(\boldsymbol{v_0})}. \end{aligned}$$

If we further assume that $\sigma(\boldsymbol{v_0}) = \sigma = \text{const.}$, we get

$$\begin{aligned} \nu_t &= n_g \sigma v_0, \\ \lambda &= \frac{v_0}{\nu_t} = \frac{1}{n_g \sigma}. \end{aligned}$$

These dependencies can be seen in the figure A.4 as dashed asymptotes for $v_0 \to \infty$.

Finally, we can outline how to proceed with collision treatment in a general case:

1. Every time step, probability that the concrete charged particle collides in time interval Δt is calculated according to (see also general definition of collision cross section in section A.1)

$$\begin{aligned} p = 1 - \exp\left(-n_g \sigma \Delta x\right) = 1 - \exp\left[-\frac{\Delta x}{\lambda(v)}\right] = 1 - \exp\left[-\frac{v\Delta t}{\lambda(v)}\right] = \\ = 1 - \exp\left[-\frac{\Delta t}{\tau(v)}\right] = 1 - \exp\left[-\nu_t(v)\Delta t\right], \end{aligned}$$

   where ν_t is in case of Maxwellian neutrals given by equation A.2.4.

2. In case of a collision, neutral particle with which the charged particle collides is generated from the normalized velocity distribution

$$g(\boldsymbol{v}) = \frac{\nu_{vt}}{\nu_t},$$

where ν_{vt} and ν_t are in case of Maxwellian neutrals given by equations A.2.3 and A.2.4.

The outlined general procedure has two disadvantages that significantly affect calculation time: First, probability of a collision has to be calculated every time step for every charged particle in the simulation. Second, interacting neutral particle is generated from quite complicated velocity distribution which is even more complicated in the case of anisotropic scattering.

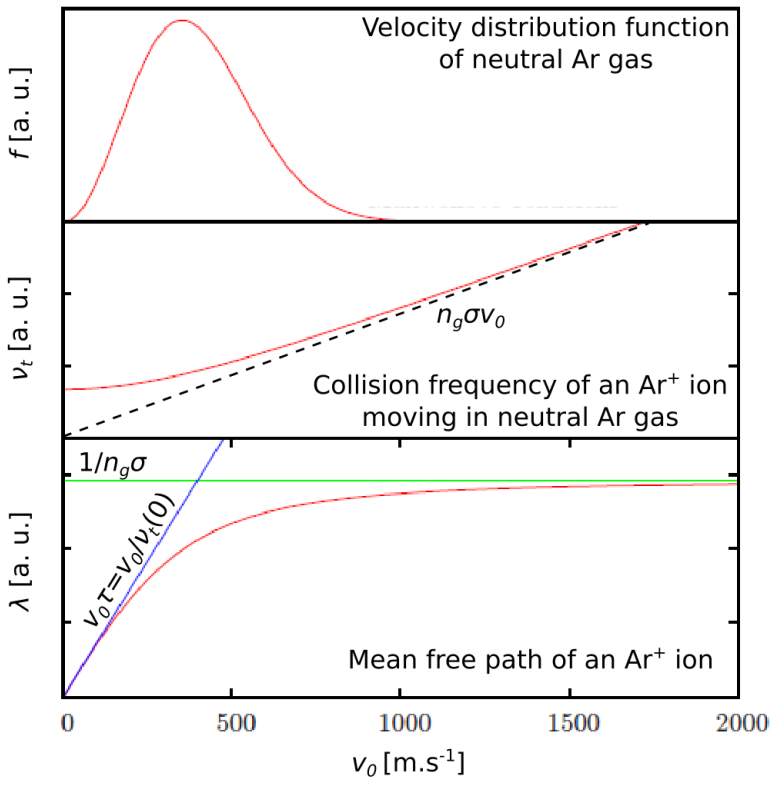

Figure A.4: Velocity dependance of the collision frequency ν and mean free path λ of an Ar^+ ion which is moving in neutral argon gas with Maxwellian velocity distribution $f(v)$. Taken from the diploma thesis Roučka [2008].

Null collision method To overcome the above mentioned disadvantages of the general procedure, we can take advantage of the null collision method. Let us consider the general expression A.2.2

$$N_{\mathrm{d}\boldsymbol{v}\mathrm{d}t} = \nu_{vt}\mathrm{d}\boldsymbol{v}\mathrm{d}t = n_g f(\boldsymbol{v})\sigma(\boldsymbol{v}-\boldsymbol{v_0})\,|\boldsymbol{v}-\boldsymbol{v_0}|\,\mathrm{d}\boldsymbol{v}\mathrm{d}t.$$

Let us introduce a constant ν_{max}

$$\nu_{max} = n_g \max_{\boldsymbol{v_r}}\{|\boldsymbol{v_r}|\,\sigma(\boldsymbol{v_r})\},$$

where maximum is considered over all possible relative velocities $\boldsymbol{v_r} = \boldsymbol{v} - \boldsymbol{v_0}$ that can occur in the simulation. It corresponds to introduction of a new collision process called null collision (see also figure A.5) which does not have any effect and which cross section is

$$\sigma_0(\boldsymbol{v}) = \frac{\nu_{max}}{n_g|\boldsymbol{v}|} - \sum_i \sigma_i(\boldsymbol{v}),$$

where the sum is performed over all real collision processes that the charged particle can undergo with the given neutral species. Thus, we can write

$$\nu_{max} = n_g|\boldsymbol{v}| \left[\sigma_0(\boldsymbol{v}) + \sum_i \sigma_i(\boldsymbol{v})\right] = \text{const.}.$$

As a result, we get

$$N_{\mathrm{d}\boldsymbol{v}\mathrm{d}t} = \nu_{\boldsymbol{v}t}\mathrm{d}\boldsymbol{v}\mathrm{d}t = \nu_{max} f(\boldsymbol{v})\mathrm{d}\boldsymbol{v},$$

$$N_{\mathrm{d}t} = \nu_t \mathrm{d}t = \int_{\boldsymbol{v}} \nu_{\boldsymbol{v}t}\mathrm{d}\boldsymbol{v}\mathrm{d}t = \int_{\boldsymbol{v}} \nu_{max} f(\boldsymbol{v})\mathrm{d}\boldsymbol{v}\mathrm{d}t = \nu_{max}\mathrm{d}t,$$

since velocity distribution $f(\boldsymbol{v})$ is normalized, $\int f(\boldsymbol{v})\mathrm{d}\boldsymbol{v} = 1$. For the velocity distribution $g(\boldsymbol{v})$ of neutrals which hit the charged particle in the time interval $(t, t + \mathrm{d}t)$ we can write

$$g(\boldsymbol{v})\mathrm{d}\boldsymbol{v} = \frac{N_{\mathrm{d}\boldsymbol{v}\mathrm{d}t}}{N_{\mathrm{d}t}} = \frac{\nu_{max} f(\boldsymbol{v})\mathrm{d}\boldsymbol{v}\mathrm{d}t}{\nu_{max}\mathrm{d}t} = f(\boldsymbol{v})\mathrm{d}\boldsymbol{v}.$$

It means that the distribution $g(\boldsymbol{v})$ is exactly the same as the distribution of all neutrals in the background.

Finally, the probability p that the charged particle collides in the time interval Δt is:

$$p = 1 - \exp\left(-\nu_{max}\Delta t\right),$$

and velocity distribution of the interacting neutrals is

$$g(\boldsymbol{v}) = f(\boldsymbol{v}).$$

It can be stated that there are two significant advantages of the proposed null collision method:

- Probability p is independent of velocity of the particle and it is the same for all particles in the simulated ensemble. Thus, it is not necessary to evaluate p for every particle in every time step; instead, we can perform collisions for randomly chosen

  $$N_C = pN_T = \left[1 - \exp\left(-\nu_{max}\Delta t\right)\right] N_T,$$

  particles in every time step (N_T is the total number of the charged particles in the simulation).

- The ineracting neutral can be generated from the same velocity distribution as the neutrals in the background have. Often, it is Maxwellian distribution.

If the collision occurs, cross section σ_i and collision frequency

$$\nu_i = n_g \left| \boldsymbol{v} - \boldsymbol{v_0} \right| \sigma_i(\boldsymbol{v} - \boldsymbol{v_0})$$

are determined for all possible collision types that the charged particle can undergo. Then, one collision type is selected with probability proportional to the particular collision frequencies.

Time step of the simulation Δt has to be set up with respect to $\tau_{min} = \frac{1}{\nu_{max}}$. The implementation of the null collision method described above allows us to treat only one collision event for a given particle per single Δt; as a consequence, Δt must be less than τ_{min}. Roucka and Hrach [2011] show that in a special case (charged particles in homogeneous electric field that collide with particles of neutral background gas with cross section independent of the particle velocity, collision is simulated by stopping the charged particle ⇒ simple model of resonant charge transfer interaction of ions with cold neutrals), the mean error in energy determination can still be around 10% for time steps $\Delta t = \frac{\tau_{min}}{10}$.

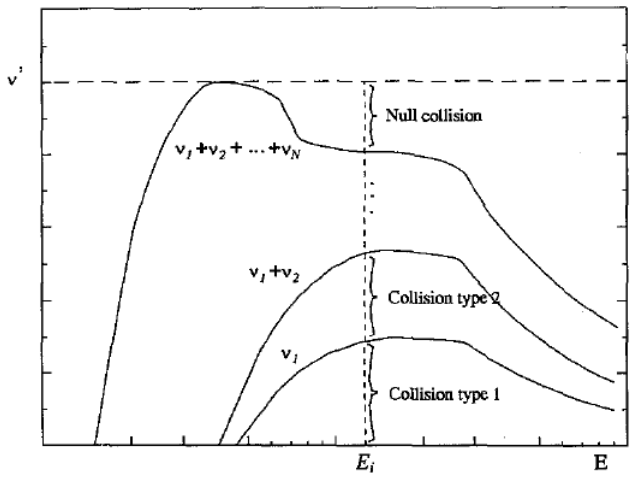

Figure A.5: The addition of the null collision process results in a constant collision frequency over all energies. Taken from the article Vahedi and Surendra [1995].

Null collision method based on time-to-scatter evaluation Condition $\Delta t < \tau_{min}$ can lead to computationally expensive simulations, especially in the cases when ν_{max} is high (e. g. medium and high pressure plasmas). For that reason, we can introduce an alternative implementation of the null collision method which is based on the continuous time axis for collision treatment during the simulation.

In view of the null collision method, the probability that the charged particle undergoes a collision in time t is

$$p(t) = 1 - \exp\left(-\nu_{max} t\right) = 1 - \exp\left(-\frac{t}{\tau_{min}}\right).$$

This expression can be regarded as a cumulative distribution function for the probability that the charged particle undergoes a collision. Probability density

function $f(t)$ for time to the collision can be written as

$$f(t) = \frac{\mathrm{d}p(t)}{\mathrm{d}t} = \frac{1}{\tau_{min}} \exp\left(-\frac{t}{\tau_{min}}\right),$$

where τ_{min} is the mean value of this probability distribution.

Instead of performing colision for $N_C = pN_T$ particles every time step Δt, we can generate time-to-scatter τ_i for each particle from distribution

$$f(t) = \frac{1}{\tau_{min}} \exp\left(-\frac{t}{\tau_{min}}\right),$$

and check each particle in every time step of the simulation whether this time was already reached. This method seems to be less efficient than the previous approach but it allows us to introduce continuous time axis for collision treatment during the simulation: if time-to-scatter is larger than Δt, we can calculate clasically trajectory of the particle over Δt and subtract Δt from time-to-scatter. If time-to-scatter is smaller than Δt, we integrate equation of motion for the particle till time-to-scatter, collision and its effects is performed and new time-to-scatter is generated. We repeat this process until Δt is reached.

A.3 Mechanics of particle collisions

Let us have 2 particles that collide: particle 1 (= incident particle) with mass m_1 and velocity $\boldsymbol{v_1}$ and particle 2 (= target particle) with mass m_2 and velocity $\boldsymbol{v_2}$. It is assumed that the collision is in general inelastic, no external forces act on the particles and there is also zero mutual force between the particles. The particles are treated as mass points. Particle velocities $\boldsymbol{v_1'}$, $\boldsymbol{v_2'}$ after the collision are to be determined ($\Rightarrow$ it means 6 unknowns).

To determine unknown velocities $\boldsymbol{v_1'}$ and $\boldsymbol{v_2'}$, 3 equations of momentum conservation and 1 equation of energy conservation can be used. Additionally, 2 independent parameters representing scattering angles have to be set down.

Momentum conservation equation

$$m_1\boldsymbol{v_1} + m_2\boldsymbol{v_2} = m_1\boldsymbol{v_1'} + m_2\boldsymbol{v_2'}. \tag{A.3.1}$$

Energy conservation equation

$$K = \frac{1}{2}m_1v_1^2 + \frac{1}{2}m_2v_2^2 = \frac{1}{2}m_1v_1'^2 + \frac{1}{2}m_2v_2'^2 + \Delta E = K' + \Delta E,$$

where ΔE is the energy loss (in case of e. g. excitation process, $\Delta E = \epsilon_{exc} =$ excitation energy) or energy gain (in case of superelastic collisions) in the inelastic collision.

Let us define velocity of centre-of-mass of the 2 particles ($M := m_1 + m_2$)

$$\boldsymbol{v_{CM}} := \frac{1}{M}\left(m_1\boldsymbol{v_1} + m_2\boldsymbol{v_2}\right).$$

Further, we introduce

$$\begin{aligned}\boldsymbol{v_r'} &= \boldsymbol{v_1'} - \boldsymbol{v_2'}\\ \Rightarrow \boldsymbol{v_1'} &= \boldsymbol{v_2'} + \boldsymbol{v_r'}\\ \Rightarrow \boldsymbol{v_2'} &= \boldsymbol{v_1'} - \boldsymbol{v_r'}.\end{aligned}$$

Equation A.3.1 then becomes

$$\boldsymbol{P} = M\boldsymbol{v_{CM}} = m_1\boldsymbol{v_1} + m_2\boldsymbol{v_2} = m_1\boldsymbol{v_1'} + m_2\boldsymbol{v_2'}.$$

This equation can be reformulated using velocity $\boldsymbol{v_r'}$

$$\begin{aligned} M\boldsymbol{v_{CM}} &= m_1\boldsymbol{v_1'} + m_2\boldsymbol{v_2'} = m_1\boldsymbol{v_1'} + m_2\boldsymbol{v_1'} - m_2\boldsymbol{v_r'} = M\boldsymbol{v_1'} - m_2\boldsymbol{v_r'} \\ &\Rightarrow \boldsymbol{v_1'} = \boldsymbol{v_{CM}} + \frac{m_2}{M}\boldsymbol{v_r'}, \end{aligned}$$

$$\begin{aligned} M\boldsymbol{v_{CM}} &= m_1\boldsymbol{v_1'} + m_2\boldsymbol{v_2'} = m_1\boldsymbol{v_2'} + m_1\boldsymbol{v_r'} + m_2\boldsymbol{v_2'} = M\boldsymbol{v_2'} + m_1\boldsymbol{v_r'} \\ &\Rightarrow \boldsymbol{v_2'} = \boldsymbol{v_{CM}} - \frac{m_1}{M}\boldsymbol{v_r'}. \end{aligned}$$

Usage of momentum conservation equation and reformulation of the problem allowed us to reduce the problem of finding 6 components of vectors $\boldsymbol{v_1'}$, $\boldsymbol{v_2'}$ to the problem of finding 3 components of vector $\boldsymbol{v_r'}$: magnitude v_r will be determined from energy conservation equation, direction of $\boldsymbol{v_r'}$ will be given by 2 independent variables χ, η representing scattering angles.

Usage of energy conservation equation to determine v_r

$$K = \frac{1}{2}m_1v_1^2 + \frac{1}{2}m_2v_2^2 = \frac{1}{2}m_1v'^2_1 + \frac{1}{2}m_2v'^2_2 + \Delta E = K' + \Delta E.$$

LHS can be reformulated

$$K = \frac{P^2}{2(m_1+m_2)} + \frac{m_1m_2}{2(m_1+m_2)}v_r^2 = \frac{P^2}{2M} + \frac{1}{2}\mu_r v_r^2,$$

where $P = |\boldsymbol{P}| = |m_1\boldsymbol{v_1} + m_2\boldsymbol{v_2}|$, $v_r = |\boldsymbol{v_r}| = |\boldsymbol{v_1} - \boldsymbol{v_2}|$, $M = m_1 + m_2$, $\mu_r = \frac{m_1m_2}{m_1+m_2}$.

Proof:

$$\begin{aligned} P^2 &= (m_1\boldsymbol{v_1} + m_2\boldsymbol{v_2})^2 = m_1^2v_1^2 + m_2^2v_2^2 + 2m_1m_2\boldsymbol{v_1}\cdot\boldsymbol{v_2}, \\ v_r^2 &= (\boldsymbol{v_1} - \boldsymbol{v_2})^2 = v_1^2 + v_2^2 - 2\boldsymbol{v_1}\cdot\boldsymbol{v_2}, \end{aligned}$$

$$\begin{aligned} P^2 + m_1m_2v_r^2 &= m_1^2v_1^2 + m_2^2v_2^2 + 2m_1m_2\boldsymbol{v_1}\cdot\boldsymbol{v_2} + \\ &\quad + m_1m_2v_1^2 + m_1m_2v_2^2 - 2m_1m_2\boldsymbol{v_1}\cdot\boldsymbol{v_2} = \\ &= m_1^2v_1^2 + m_1m_2v_1^2 + m_2^2v_2^2 + m_1m_2v_2^2 = \\ &= m_1v_1^2(m_1+m_2) + m_2v_2^2(m_1+m_2) = \\ &= (m_1+m_2)(m_1v_1^2 + m_2v_2^2), \end{aligned}$$

$$\frac{P^2 + m_1m_2v_r^2}{2(m_1+m_2)} = \frac{(m_1+m_2)(m_1v_1^2+m_2v_2^2)}{2(m_1+m_2)} = \frac{1}{2}m_1v_1^2 + \frac{1}{2}m_2v_2^2 = K.$$

Similarly

$$K' = \frac{P'^2}{2(m_1+m_2)} + \frac{m_1m_2}{2(m_1+m_2)}v'^2_r = \frac{P'^2}{2M} + \frac{1}{2}\mu_r v'^2_r,$$

where $P' = |\boldsymbol{P'}| = |m_1\boldsymbol{v'_1} + m_2\boldsymbol{v'_2}| = |\boldsymbol{P}| = P$ (momentum conservation), $v'_r = |\boldsymbol{v'_r}| = |\boldsymbol{v'_1} - \boldsymbol{v'_2}|$. Finally, we can write:

$$\begin{aligned} K &= K' + \Delta E, \\ \frac{P^2}{2M} + \frac{1}{2}\mu_r v_r^2 &= \frac{P'^2}{2M} + \frac{1}{2}\mu_r v'^2_r + \Delta E, \\ \frac{1}{2}\mu_r v'^2_r &= \frac{1}{2}\mu_r v_r^2 - \Delta E, \\ v'_r &= \left(v_r^2 - \frac{2\Delta E}{\mu_r}\right)^{\frac{1}{2}}. \end{aligned} \tag{A.3.2}$$

What is ΔE?

- Elastic collision: $\Delta E = 0$,
- Inelastic collision: $\Delta E \neq 0$,
  - excitation: $\Delta E = \epsilon_{exc} > 0$ ... excitation energy,
  - superelastic collision: $\Delta E = \epsilon_{de-exc} < 0$ ... de-excitation energy from upper level to lower level,
  - ionization: $\Delta E = \epsilon_{ion} + \epsilon_{ej} > 0$ ... ϵ_{ion} = ionization energy, ϵ_{ej} = energy of ejected electron which might have distribution $\sigma_{ion}(\epsilon_1, \epsilon_{ej})$, where ϵ_1 is energy of the incident electron.

How to determine ΔE in case of ionization? Let us consider several auxiliary approximations that lead us to the expressions for general case.

Auxiliary approximation 1: Target neutral particle can be considered at rest ($v_2 \sim v'_2 \sim 0$) since ionization processes generally involve energy much higher than the energy of the neutral gas in the background. Moreover, it can be assumed that $m_2 >> m_1$. Energy conservation equation then becomes (particle 1 is the incident electron)

$$\epsilon_1 = \frac{1}{2}m_1 v_1^2 = \frac{1}{2}m_1 v'^2_1 + \epsilon_{ej} + \epsilon_{ion}.$$

Generally, ϵ_{ej} depends on differential ionization cross section $\frac{\mathrm{d}\sigma_{ion}}{\mathrm{d}\epsilon}(\epsilon_1, \epsilon)$. Energy ϵ_{ej} can then be determined

$$r_{ion} = \frac{\int_0^{\epsilon_{ej}} \frac{\mathrm{d}\sigma_{ion}}{\mathrm{d}\epsilon}(\epsilon_1, \epsilon)\mathrm{d}\epsilon}{\sigma_{ion}(\epsilon_1)},$$

where $r_{ion} \in [0, 1]$ is random number generated from uniform distribution and $\sigma_{ion}(\epsilon_1)$ is integral ionization cross section; $\sigma_{ion}(\epsilon_1) = \int_0^{\epsilon_{ej,max}} \frac{\mathrm{d}\sigma_{ion}}{\mathrm{d}\epsilon}(\epsilon_1, \epsilon)\mathrm{d}\epsilon$, where $\epsilon_{ej,max} = \epsilon_1 - \epsilon_{ion}$.

Auxiliary approximation 2: Let us assume that the differential ionization cross section is independent of the energy ϵ of the ejected electron, $\frac{\mathrm{d}\sigma_{ion}}{\mathrm{d}\epsilon}(\epsilon_1, \epsilon) = \frac{\mathrm{d}\sigma_{ion}}{\mathrm{d}\epsilon}(\epsilon_1)$. It is equivalent to the situation when energy is divided among scattered and ejected electron according to random uniform distribution

$$\begin{aligned} \frac{1}{2}m_1 v'^2_1 + \epsilon_{ej} &= \frac{1}{2}m_1 v_1^2 - \epsilon_{ion}, \\ \epsilon_{ej} &= r_{ion}\left(\frac{1}{2}m_1 v_1^2 - \epsilon_{ion}\right), \end{aligned}$$

where $r_{ion} \in [0,1]$ is random number generated from uniform distribution.

$$\frac{1}{2}m_1 v_1'^2 = (1 - r_{ion})\left(\frac{1}{2}m_1 v_1^2 - \epsilon_{ion}\right),$$
$$v_1'^2 = (1 - r_{ion})\left(v_1^2 - \frac{2\epsilon_{ion}}{m_1}\right). \tag{A.3.3}$$

Auxiliary approximation 3: half energy is taken by scattered electron, the other half is taken by ejected electron ($r_{ion} = 0.5$ in equation A.3.3)

$$v_1' = \frac{1}{\sqrt{2}}\left(v_1^2 - \frac{2\epsilon_{ion}}{m_1}\right)^{\frac{1}{2}}.$$

Let us consider general case without any approximation. According to the equation A.3.2 relative velocity v_r' is given by

$$v_r'^2 = v_r^2 - \frac{2\Delta E}{\mu_r}, \tag{A.3.4}$$
$$\Delta E = \epsilon_{ion} + \epsilon_{ej}. \tag{A.3.5}$$

In the most general case, energy of the ejected electron ϵ_{ej} has distribution described by differential ionization cross section $\frac{\mathrm{d}\sigma_{ion}}{\mathrm{d}\epsilon}(\epsilon_r, \epsilon)$, where $\epsilon_r = \frac{1}{2}\mu_r v_r^2$. Energy ϵ_{ej} can then be determined

$$r_{ion} = \frac{\int_0^{\epsilon_{ej}} \frac{\mathrm{d}\sigma_{ion}}{\mathrm{d}\epsilon}(\epsilon_r, \epsilon)\mathrm{d}\epsilon}{\sigma_{ion}(\epsilon_r)},$$

where $r_{ion} \in [0,1]$ is random number generated from uniform distribution and $\sigma_{ion}(\epsilon_r)$ is integral ionization cross section; $\sigma_{ion}(\epsilon_r) = \int_0^{\epsilon_{ej,max}} \frac{\mathrm{d}\sigma_{ion}}{\mathrm{d}\epsilon}(\epsilon_r, \epsilon)\mathrm{d}\epsilon$, where $\epsilon_{ej,max} = \epsilon_r - \epsilon_{ion}$.

If we want to introduce an approximation at this point that energy is divided among scattered and ejected electron according to random uniform distribution, we can first find the maximal possible energy of the ejected electron $\epsilon_{ej,max}$ from equations A.3.4 and A.3.5. This corresponds to the situation when all resultant kinetic energy in the centre-of-mass frame is taken by the ejected electron:

$$\epsilon_{ej,max} \Leftrightarrow v_r' = 0 \Leftrightarrow v_r^2 - \frac{2\Delta E}{\mu_r} = 0,$$
$$\Delta E = \frac{1}{2}\mu_r v_r^2,$$
$$\epsilon_{ion} + \epsilon_{ej,max} = \frac{1}{2}\mu_r v_r^2,$$
$$\epsilon_{ej,max} = \frac{1}{2}\mu_r v_r^2 - \epsilon_{ion}.$$

Energy of the ejected electron ϵ_{ej} can then be determined

$$\epsilon_{ej} = r_{ion}\left(\frac{1}{2}\mu_r v_r^2 - \epsilon_{ion}\right),$$

where $r_{ion} \in [0,1]$ is random number generated from uniform distribution. Finally, we get expression for magnitude of relative velocity v_r'

$$\frac{\mu_r}{2}v_r'^2 = \frac{\mu_r}{2}v_r^2 - \epsilon_{ion} - \epsilon_{ej} = (1 - r_{ion})\left(\frac{\mu_r}{2}v_r^2 - \epsilon_{ion}\right),$$
$$v_r' = (1 - r_{ion})^{\frac{1}{2}}\left(v_r^2 - \frac{2\epsilon_{ion}}{\mu_r}\right)^{\frac{1}{2}}. \tag{A.3.6}$$

In special case ($r_{ion} = 0.5$) when energy is distributed equally between scattered and ejected electron, we get

$$v_r' = \frac{1}{\sqrt{2}} \left(v_r^2 - \frac{2\epsilon_{ion}}{\mu_r} \right)^{\frac{1}{2}}.$$

If we take into account approximation $m_2 >> m_1$ and $v_2 \sim v_2' \sim 0$, equation A.3.6 passes to the equation A.3.3 since $\mu_r = \frac{m_1 m_2}{m_1+m_2} = \frac{m_1}{m_1/m_2+1} \sim m_1$, $v_r = |\boldsymbol{v_1} - \boldsymbol{v_2}| \sim v_1$ and $v_r' = |\boldsymbol{v_1'} - \boldsymbol{v_2'}| \sim v_1'$ in this approximation.

As a last step, direction of vector $\boldsymbol{v_r'}$ has to be determined. For that purpose, polar angle $\chi \in [0, \pi]$ and azimuthal angle $\eta \in [0, 2\pi]$ has to be determined. Generally, in the approximation that we use (particles treated as mass points with zero mutual force) these are 2 independent parameters.

- Polar angle χ
  - Anisotropic scattering: distribution of deflection polar angle χ is given by differential cross section $\sigma_d(\epsilon_r, \chi)$ and angle χ can be determined according to
    $$r_\chi = \frac{\int_0^\chi \sigma_d(\epsilon_r, \chi') \sin\chi' \mathrm{d}\chi'}{\int_0^\pi \sigma_d(\epsilon_r, \chi') \sin\chi' \mathrm{d}\chi'}, \tag{A.3.7}$$
    where $r_\chi \in [0, 1]$ is random variable generated from the uniform distribution.
    [Total cross section σ_t is given by $\sigma_t(v_r) = 2\pi \int_0^\pi \sigma_d(v_r, \chi) \sin\chi \mathrm{d}\chi$.]
  - Isotropic scattering: we can consider $\sigma_d(\epsilon_r, \chi) = \sigma_d(\epsilon_r)$ and expression A.3.7 is simplified to
    $$\cos\chi = 1 - 2r_\chi.$$
- Azimuthal angle η
  $$\eta = 2\pi r_\eta, \tag{A.3.8}$$
  where $r_\eta \in [0, 1]$ is random variable generated from the uniform distribution.

If there is non-zero mutual force between the interacting particles (e. g. Coulomb collisions), there is additional condition based on which scattering angles can be determined.

A.4 Transformations of vectors and coordinate systems

Notes to the transformations between local and laboratory coordinate systems when treating collision processes.

- Let us have velocity $\boldsymbol{v_1}$ of the incident particle, velocity $\boldsymbol{v_2}$ of the target particle, relative velocity $\boldsymbol{v_r} = \boldsymbol{v_1} - \boldsymbol{v_2}$ before the collision and relative velocity $\boldsymbol{v_r'}$ after the collision.

- Let us have some laboratory system (x, y, z), figure A.6. Local system $(\widehat{x}, \widehat{y}, \widehat{z})$ is created in a way that $\widehat{z}$ axis is aligned with the direction of the relative velocity $\boldsymbol{v_r}$. Angles θ and ϕ are given by the components of the vector $\boldsymbol{v_r}$ in the system (x, y, z):

$$\sin\theta = \frac{\sqrt{v_{r,x}^2 + v_{r,y}^2}}{v_r}, \qquad \cos\theta = \frac{v_{r,z}}{v_r},$$

$$\sin\phi = \frac{v_{r,x}}{\sqrt{v_{r,x}^2 + v_{r,y}^2}}, \qquad \cos\phi = -\frac{v_{r,y}}{\sqrt{v_{r,x}^2 + v_{r,y}^2}}.$$

- How is the laboratory system (x, y, z) turned to the local system $(\widehat{x}, \widehat{y}, \widehat{z})$: 1. Rotation about z axis by an angle ϕ. This gives system (x^*, y^*, z^*). 2. Rotation about x^* axis by an angle θ. This gives system $(\widehat{x}, \widehat{y}, \widehat{z})$.

- Vector $\boldsymbol{v_r'}$ is generated in the local system $(\widehat{x}, \widehat{y}, \widehat{z})$, angles η and χ are random variables generated from appropriate distribution:

$$\begin{aligned} v'_{r,\widehat{x}} &= v'_r \cos\eta \sin\chi, \\ v'_{r,\widehat{y}} &= v'_r \sin\eta \sin\chi, \\ v'_{r,\widehat{z}} &= v'_r \cos\chi. \end{aligned}$$

  For further calculations, coordinates of updated relative velocity in the laboratory system are needed: $v'_{r,x}, v'_{r,y}, v'_{r,z}$.

- Example: $A' = [T]\, A$
  - A' ... coordinates of vector A in the system (x', y', z')
  - A ... coordinates of vector A in the system (x, y, z)
  - $[T]$ ... transformation matrix for transition from system (x, y, z) to the system (x', y', z'). E. g. for system (x', y', z') which originated from system (x, y, z) by rotation around z axis by angle γ, it means:

$$[T] = \begin{pmatrix} \cos\gamma & \sin\gamma & 0 \\ -\sin\gamma & \cos\gamma & 0 \\ 0 & 0 & 1 \end{pmatrix}.$$

- The vector $\boldsymbol{v_r'}$ is needed to be transformed 2 times:
  1. Transformation from system $(\widehat{x}, \widehat{y}, \widehat{z})$ to the system (x^*, y^*, z^*) which originated by rotation around $\widehat{x}$ axis by angle $(-\theta)$:

$$\begin{pmatrix} v'_{r,x^*} \\ v'_{r,y^*} \\ v'_{r,z^*} \end{pmatrix} = \begin{pmatrix} 1 & 0 & 0 \\ 0 & \cos(-\theta) & \sin(-\theta) \\ 0 & -\sin(-\theta) & \cos(-\theta) \end{pmatrix} \begin{pmatrix} v'_{r,\widehat{x}} \\ v'_{r,\widehat{y}} \\ v'_{r,\widehat{z}} \end{pmatrix} =$$

$$= \begin{pmatrix} 1 & 0 & 0 \\ 0 & \cos\theta & -\sin\theta \\ 0 & \sin\theta & \cos\theta \end{pmatrix} \begin{pmatrix} v'_{r,\widehat{x}} \\ v'_{r,\widehat{y}} \\ v'_{r,\widehat{z}} \end{pmatrix}.$$

2. Transformation from system (x^*, y^*, z^*) to the system (x, y, z) which originated by rotation around z^* axis by angle $(-\phi)$:

$$\begin{pmatrix} v'_{r,x} \\ v'_{r,y} \\ v'_{r,z} \end{pmatrix} = \begin{pmatrix} \cos(-\phi) & \sin(-\phi) & 0 \\ -\sin(-\phi) & \cos(-\phi) & 0 \\ 0 & 0 & 1 \end{pmatrix} \begin{pmatrix} v'_{r,x^*} \\ v'_{r,y^*} \\ v'_{r,z^*} \end{pmatrix} = \\ = \begin{pmatrix} \cos\phi & -\sin\phi & 0 \\ \sin\phi & \cos\phi & 0 \\ 0 & 0 & 1 \end{pmatrix} \begin{pmatrix} v'_{r,x^*} \\ v'_{r,y^*} \\ v'_{r,z^*} \end{pmatrix}.$$

- Finally:

$$\begin{pmatrix} v'_{r,x} \\ v'_{r,y} \\ v'_{r,z} \end{pmatrix} = \begin{pmatrix} \cos\phi & -\sin\phi & 0 \\ \sin\phi & \cos\phi & 0 \\ 0 & 0 & 1 \end{pmatrix} \begin{pmatrix} 1 & 0 & 0 \\ 0 & \cos\theta & -\sin\theta \\ 0 & \sin\theta & \cos\theta \end{pmatrix} \begin{pmatrix} v'_{r,\widehat{x}} \\ v'_{r,\widehat{y}} \\ v'_{r,\widehat{z}} \end{pmatrix} = \\ = \begin{pmatrix} \cos\phi & -\sin\phi & 0 \\ \sin\phi & \cos\phi & 0 \\ 0 & 0 & 1 \end{pmatrix} \begin{pmatrix} 1 & 0 & 0 \\ 0 & \cos\theta & -\sin\theta \\ 0 & \sin\theta & \cos\theta \end{pmatrix} \begin{pmatrix} \cos\eta\sin\chi \\ \sin\eta\sin\chi \\ \cos\chi \end{pmatrix} v'_r = \\ = \begin{pmatrix} \cos\phi & -\sin\phi\cos\theta & \sin\phi\sin\theta \\ \sin\phi & \cos\phi\cos\theta & -\cos\phi\sin\theta \\ 0 & \sin\theta & \cos\theta \end{pmatrix} \begin{pmatrix} \cos\eta\sin\chi \\ \sin\eta\sin\chi \\ \cos\chi \end{pmatrix} v'_r.$$

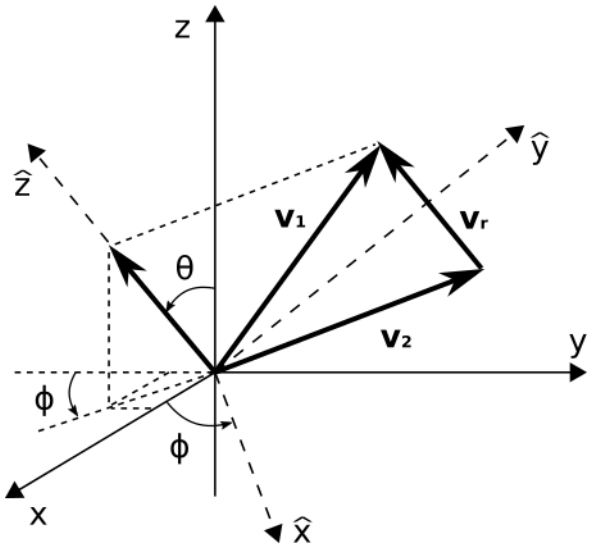

Figure A.6: Transformation from the local coordinate system $(\widehat{x}, \widehat{y}, \widehat{z})$ to the laboratory one (x, y, z).

A.5 Source codes

As an appendix to the thesis, the source codes of the developed computer models are provided. We attach them to the printed version of the thesis on a CD and to the electronic version of the work as an electronic attachment.

The following source codes are provided:

- **2D-PIC-MCC**: the source code of the 2D PIC/MCC plasma model developed in C programming language.
- **3D-PIC-MCC**: the source code of the 3D PIC/MCC plasma model developed in C++ programming language.
- **3D-FLUID**: drift-diffusion fluid model of plasma based on the FEniCS software.
- **POSTPROCESSING**: Python package of scripts for post-processing of the developed model results.